nature medicine

Article

https://doi.org/10.1038/s41591-025-03884-4

Perioperative IDH inhibition in treatment-naive IDH-mutant glioma: a pilot trial

Received: 24 September 2024

Accepted: 3 July 2025

A list of authors and their affiliations appears at the end of the paper

Mutant isocitrate dehydrogenase (mIDH) inhibition significantly improves progression-free survival in patients with mIDH WHO grade 2 glioma; however, a large proportion of patients will progress, and mechanisms of adaptation to mIDH inhibition remain poorly understood. Perioperative studies with evaluation of paired pre- and post-treatment samples enable detailed understanding of drug response, facilitating biomarker development, but are rare in glioma owing to safety and cost concerns. Here we conducted a single-arm, open-label feasibility perioperative trial in patients with mIDH1 low-grade glioma, treatment naive to radiation and chemotherapy, with safusidenib (AB-218/DS-1001b), an orally available small-molecule inhibitor of mIDH1. As of 8 November 2024, 10 patients were enrolled and have completed the perioperative component, with a median follow-up of 14 months. Patients continue postoperative safusidenib with ongoing follow-up for safety and efficacy. The primary endpoint showed the feasibility and acceptability of conducting a two-stage perioperative trial. One patient experienced a serious surgery-related adverse event, and ten reported safusidenib-related adverse events; most were grade 1, and one experienced grade 3 elevation of transaminases. Tumor 2-hydroxyglutarate quantification revealed on-target activity, associated with alterations in differentiation programs and neural excitability, functionally validated in post hoc analysis by patch-clamp electrophysiology. Taken together, these results provide a detailed investigation of observations associated with mIDH inhibition in glioma. The study shows the safety and feasibility of this perioperative approach, which can be applied broadly in clinical trial design, serving as proof of concept for advancing drug development in glioma. ClinicalTrials.gov registration: NCT05577416.

The introduction of mutant isocitrate dehydrogenase (mIDH) inhibitors into clinical practice for patients with mIDH lower-grade gliomas (LGGs) marks a key advance in precision medicine. Several clinical trials have shown that these therapies are well tolerated, yield radiological responses and extend progression-free survival[1–4]. Neomorphic mutation of mIDH1/2 drives tumorigenesis by converting α-ketoglutarate (α-KG) to the oncogenic metabolite (R)-2-hydroxyglutarate (2-HG)[5], disrupting epigenetic landscapes[6] including histone hypermethylation[7], redox homeostasis[8] and T cell function[9–11]. Although *IDH* mutations occur early and persist through glioma evolution[12], most studies showed benefit predominantly in non-enhancing, lower-grade tumors, collectively suggesting that mIDH therapeutic targeting early and before standard-of-care radiation and chemotherapy may be most beneficial[13].

Perioperative studies, wherein patients undergo a biopsy followed by biomarker-informed neoadjuvant treatment before resection, provide a unique opportunity to study drug response[14–16]. Paired

✉e-mail: kate.drummond@mh.org.au; whittle.j@wehi.edu.au

treatment-naive and treated tissue samples allow assessment of pharmacokinetics (PK) and pharmacodynamics (PD), confirmation of target engagement and delineation of predictive biomarkers with internal controls strengthening statistical power. In glioma, this requires consideration of safety and financial implications. Thus, few perioperative trials have been undertaken in brain cancer.

Safusidenib is an oral, brain-penetrant selective inhibitor of the IDH1-R132X enzyme[17], with promising activity in recurrent mIDH1 gliomas both in enhancing and non-enhancing disease[4]. We report a single-arm perioperative trial (NCT05577416) in patients with *IDH1*-mutant LGG who underwent open biopsy, before neoadjuvant treatment with safusidenib and subsequent resection. We report endpoints from the perioperative component of the study, to assess biological effects of mIDH1 inhibition in tumor and peri-tumoral brain. This proof of principle study confirms the safety, feasibility and patient acceptability of perioperative trials with matched samples and highlights their potential to uncover drug mechanisms and inform future combination strategies.

Results

Clinical trial overview

Participants with a radiological or pathological diagnosis of World Health Organization (WHO) grade 2 (G2) LGG were recruited to a single center from 22 December 2022. Eligible participants were ≥18 years and not requiring urgent resection. Participants with previous radiation therapy or chemotherapy and cerebellar or brainstem lesions were excluded. In part A, participants underwent craniotomy, biopsy and lumbar puncture for cerebrospinal fluid (CSF), and received safusidenib (250 mg twice daily (b.i.d.) for 22–36 days) before craniotomy and maximal safe resection with repeat lumbar puncture, within 5 h of final dose (Fig. 1a). Participants continue on safusidenib in the ongoing adjuvant phase (part B)[18]. Primary objectives from part A were to assess the feasibility and acceptability of undertaking a two-stage surgical study. Secondary objectives include determining toxicity and safety of the planned biopsy followed by surgery, establishing biological activity and assessing the PK and antitumor activity of safusidenib. Exploratory objectives include assessing mechanisms of resistance and tumor volumetric monitoring[18].

At time of reporting, 12 participants were screened and 10 completed part A[18] (Fig. 1a, Table 1 and Supplementary Table 1). The study was ongoing at data cutoff on 8 November 2024, with a median follow-up of 14 months in part B. One participant withdrew consent pre-biopsy, and one participant had gliosis at biopsy and was withdrawn (Fig. 1a). All participants had non-contrast-enhancing WHO grade 2/3 glioma, according to WHO Central Nervous System 5 (CNS5) classification[19], with *IDH1* activating mutations. Six (60%) participants were enrolled at first presentation without previous surgery (Table 1). Seven participants had a diagnosis of astrocytoma (A-01 to A-07) and three, oligodendroglioma (O-01 to O-03) (Fig. 1b and Extended Data Fig. 1a). Response assessment using Low-Grade Glioma Response Assessment in Neuro-Oncology[20] and volumetric analysis showed stable disease for all patients following one cycle of safusidenib (Fig. 1c and Extended Data Fig. 1b–f). Most patients had gross or near-total resection, limiting response assessment in part B; two patients had stable disease, and one progressed and came off study after 13.4 months. These findings support the feasibility of the two-stage design and suggest early disease control, with ongoing follow-up required for efficacy and mechanisms of resistance.

Safety and feasibility of clinical trial

To address concerns of invasive perioperative trials in brain cancer[14], we included a validated research participant perception survey[21,22]. Eight of ten participants responded positively to recommend the study to family and friends, regardless of the demanding nature (Fig. 1d and Extended Data Fig. 1g). Safusidenib was well tolerated during part A. Seven participants (70%) reported safusidenib-related adverse events, all Common Terminology Criteria for Adverse Events V5 Grade 1. All adverse events occurring in the study (part A and B) until data cutoff on 8 November 2024, median 14 months, are reported with no new safety signals (Table 2 and Supplementary Table 2). One case of grade 3 alanine aminotransferase (ALT) rise occurred in conjunction with grade 2 aspartate aminotransferase (AST) rise, which was precipitated by drug interaction with a concomitant medication. The ALT and AST resolved to grade 1 after drug interruption (36 days), and safusidenib was recommenced at 125 mg b.i.d. Subsequently, ALT and AST rose to grade 2 after 35 days, which required drug cessation, and corticosteroids were initiated until the transaminases returned to normal levels. No other patient required dose reduction. Grade 1–2 arthralgia was reported and responsive to simple analgesia. Grade 1 dermatological toxicities were common and responded to topical interventions or oral antihistamines.

Neurosurgery-related adverse events included one serious case of postoperative hemiparesis from surgical injury unrelated to treatment, with moderate upper limb weakness and normal lower limb power at 15 months. Other events included a low-pressure headache post-lumbar puncture and a seizure admission before safusidenib commencement for a patient with known tumor-associated epilepsy. Overall, the study met its primary endpoint; the perioperative design was safe, feasible and acceptable to participants.

Pharmacokinetics and biomarker response post-safusidenib

Safusidenib was detected in therapeutic concentrations in plasma and tumor (Fig. 1e). The mean tumor concentration of safusidenib was 2,654 ng g^{-1} (3.3 µM), above the half maximal inhibitor concentration

Fig. 1 | Perioperative study safely delivers safusidenib to inhibit mIDH1. **a**, Clinical trial schema. WGTS, Whole Genome Transcription Sequencing. In part A, previously untreated participants with WHO grade 2 or 3 (G2/3) mIDH1 glioma ($n = 10$) underwent biopsy then 28 days of safusidenib treatment followed by resection surgery (within 5 h pre-resection safusidenib dose). Materials taken for translational research are depicted below. **b**, Oncoprint detailing the histopathology, whole-genome sequencing and methylation ($n = 7$ astrocytoma, A-01 to A-07; $n = 3$ oligodendroglioma, O-01 to O-03). A-04 translational tissue samples had low tumor purity (0%) and were excluded from downstream translational exploratory endpoints. NS, not significant. **c**, Volumetric analysis of tumor volume (cm^3) for T2/FLAIR sequences in each participant over time. **d**, Research Participant Perception Survey (RPPS) results from $n = 8$ participants who completed the survey. Response keys are depicted for each question. **e**, Safusidenib concentration in plasma (ng ml^{-1}), CSF (ng ml^{-1}) and tumor tissue (ng g^{-1}) at the post-safusidenib resection timepoint ($n = 10$). **f**, Comparison of safusidenib in tumor tissue (ng g^{-1}) and in plasma (ng ml^{-1}) within each participant at the post-safusidenib resection timepoint ($n = 10$, *t*-test). **g**, Quantification of tissue 2-HG in pre- and post-safusidenib tumor, paired per participant ($n = 10$). Change in 2-HG concentration depicted post-safusidenib. The asterisk indicates that A-04 (low tumor purity) was sampled from non-tumor tissue (paired *t*-test). **h**, Spatial metabolomics detecting endogenous 2-HG (m/z: 209.10; adducts: M + IsoProp + H) intensity (top) at 10 µm pixel resolution in pre- and post-safusidenib samples of participant O-01. Below is a kernel density plot visualizing the intensity. **i**, LC–MS untargeted analysis of itaconic acid ($n = 9$ participants, paired *t*-test) and citric acid ($n = 9$ participants, paired *t*-test). Each box indicates the interquartile range (IQR), the center line is the median and the whiskers extend to the furthest points within 1.5 × IQR. Participant legend as in **c**. **j**, LC–MS/MS analysis of H3 canonical histone methylation and acetylation pre- versus post-safusidenib treatment ($n = 7$ G2 participants). **k**, Quantification of H3K9 and H3K27 monomethylation marks in pre- and post-safusidenib tumor, paired per participant ($n = 8$). Each box indicates the IQR, the center line is the median and whiskers extend to the furthest points within 1.5 × IQR. Panel **a** created with BioRender.com.


a
IDH1R132X G2/3 glioma, no previous radiation or chemo n = 12
Withdrew consent n = 1
External controls: surgery only n = 7 mIDH1 LGG n = 11
Part A
Part B
28-day cycle
n = X cycles
Biopsy
Safusidenib 250 mg b.i.d. n = 10
Resection
Pre-resection dose <5 h to surgery
Safusidenib 250 mg b.i.d.
Progression
Off study
Non-cancer diagnosis n = 1
PK
[2-HG]
WGTS
Methylation DNA Histone
Metabolomics
snRNA-seq
Spatial-omics Transcriptomics Metabolomics
Patch clamp
n = 10
n = 10
n = 10
n = 10
n = 8
n = 9
n = 9
n = 3
n = 3
n = 1 (+6)
b
6 4 2 0
Diagnosis
Grade
Sex
Extent
Methylation
Me- change
Ki67
IDH1
Purity
TP53 65%
ATRX 60%
TERT 30%
X1p.19q 30%
FUBP1 20%
MUTYH 10%
X4q12 15%
X8q24 10%
EGFR 5%
ATM 5%
CIC 5%
PIK3CA 5%
Participant
Sample
A-01 A-02 A-03 A-04 A-05 A-06 A-07 O-01 O-02 O-03
Diagnosis
Astrocytoma
Oligodendroglioma
Grade
2
3
Sex
Female
Male
Count
0 5 10 15
Extent of resection (%)
100 50 0
Tumor purity (%)
100 50 0
IDH mutation
R132C
R132H
R132S
Ki67 %
10 5 0
DNA methylation
NS
P < 0.001
P < 0.01
P < 0.05
Me- change
1.0 0.5 0 −0.5 −1.0
Methylated:demethylated alterations
Deep deletion
Single copy loss
Focal amplification
Gain
Frameshift mutation
Missense mutation
Splice site variant
Promoter mutation
Nonsense mutation
Structural variant
Participant sample
Pre-safusidenib
Post-safusidenib
c
Tumor volume (cm3)
70 60 50 40 30 20 10 0
Safusidenib
Pre-biopsy
Post-biopsy
Pre-resection
Post-resection
Participants
A-01
A-02
A-03
A-04
A-05
A-06
A-07
O-01
O-02
O-03
d
Would you recommend joining a research study to your family and friends?
0 2 4 6 8
Response key
Definitely no
Probably no
Probably yes
Definitely yes
How much did the study demand of you?
0 2 4 6 8
Response key
Intense
Moderate
Simple
Did the informed consent form prepare you for what to expect during the study?
0 2 4 6 8
Participants
Response key
No
Yes, somewhat
Yes, mostly
Yes, completely
e
Safusidenib concentration (ng g−1 or ng ml−1) × 103
20 15 10 5 0
Plasma
CSF
Tumor
Participants
f
Tumor concentration of safusidenib (ng g−1) × 103
6 4 2 0
r = 0.843
P = 0.002
0 5,000 10,000 15,000 20,000
Plasma concentration of safusidenib (ng ml−1)
A-01 A-02 A-03 A-04 A-05 A-06 A-07 O-01 O-02 O-03
g
2-HG concentration (μM)
250 200 150 100 50 0
P = 0.007
Pre
Post
Safusidenib
Δ 2-HG concentration
Participant
−92.15% A-01
−92.67% A-02
−84.82% A-03
39.61%* A-04
−89.16% A-05
−91.91% A-06
−93.00% A-07
−82.41% O-01
−72.64% O-02
−97.35% O-03
h
2-HG
Pre-safusidenib
Post-safusidenib
Intensity
2.0 1.5 1.0 0.5 0.0
1 mm
1 mm
Density
1.5 1.0 0.5 0.0
i
Itaconic acid
P = 0.030
Intensity
0.20 0.15 0.10 0.05 0
Pre
Post
Safusidenib
Citric acid
P = 0.060
Intensity
0.10 0.08 0.06 0.04 0.02
Pre
Post
Safusidenib
j
me1
me2
me3
ac
H3.1 K27 K36
H3.1 K27
H3.1 K36
H3.3 K27 K36
H3.3 K27
H3.3 K36
H3 K14
H3 K18 K23
H3 K18
H3 K23
H3 K4
H3 K56
H3 K79
H3 K9 K14
H3 K9
H4 4..17
H4 4..17 1
H4 4..17 2
H4 4..17 3
H4 4..17 4
H4 K20
log(FC)
pre- versus post-safusidenib
−2 −1 0 1 2
k
H3 K9me1
Relative abundance
18 15 12 9
Pre
Post
Safusidenib
H3.1 K27me1
Relative abundance
10.0 7.5 5.0
Pre
Post
Safusidenib
Participant
A-01
A-03
A-05
A-06
A-07
O-01
O-02
O-03

Table 1 | Patient demographics and baseline characteristics

	Number	Percent
Age (years)		
Median (range)	33 (29–46)	
Sex		
Female	4	40
Male	6	60
ECOG performance status		
0	10	100
Histological classification		
Oligodendroglioma (1p19q co-deleted)	3	30
Astrocytoma	7	70
CDKN2A homozygous deletion	0	0
WHO tumor grade at biopsy		
Grade 2	10	100
IDH1 variant		
R132H	8	80
R132C	1	10
R132S	1	10
Previous resection		
0	6	60
1	3	30
2	1	10
Months from previous surgery to registration (median (range))	48 (6–118)	
Tumor location		
Frontal	7	70
Temporal	3	30

for R132H and R132C (ref. 17), with temporally consistent plasma concentrations and a mean tumor-to-plasma ratio of 0.33 (Extended Data Fig. 2a). A direct correlation was observed between plasma and tumor concentration (Fig. 1f).

On-target activity of safusidenib was assessed using 2-HG quantified with liquid and gas chromatography–mass spectrometry (LC–MS and GC–MS, respectively), revealing an 88% reduction in 2-HG from pre-safusidenib (mean 80.9 µM; range 15.47–223.99 µM) to post-safusidenib (7.85 µM, range 2.5–21.6 µM) (Fig. 1g). Safusidenib concentration trended with change in 2-HG (Extended Data Fig. 2b). A lack of 2-HG reduction in sample A-04 was consistent genomically with low tumor purity (Fig. 1b), suggesting that peri-tumoral tissue was collected for translational endpoints. Thus, A-04 was excluded from translational endpoint analyses. Consistent with previous studies[23], 2-HG was not detected at appreciable concentrations in the CSF (0.037 ± 0.009 µM) and plasma (0.071 ± 0.018 µM) (Extended Data Fig. 2c,d). We next used matrix-assisted laser desorption and ionization imaging mass spectrometry (MALDI-IMS)[24] to identify penetration throughout the resected tumor. Using a smaller cohort ($n = 3$ paired samples), we show that the dynamic abundance of 2-HG (m/z = 209.10) was reduced post-safusidenib (Fig. 1h and Extended Data Fig. 2e). Global metabolite evaluations in mIDH patient samples have previously identified only few altered metabolites[5,25,26]; however, matched patient samples have never been evaluated. We identify a subset of metabolites with altered abundance following safusidenib (Fig. 1i, Extended Data Fig. 2f and Supplementary Table 3).

Despite overall reduction of 2-HG across participants, only minor changes in global methylation levels, previously shown to correlate with mIDH (ref. 27), were detected in six participants with no significant local methylation changes (Fig. 1b). Similarly, modest changes in global methylation levels have been observed after mIDH inhibition in xenografts[6] and patient samples[2]. As 2-HG inhibits suppression of the Jumonji-C domain histone demethylase family[7,28], we investigated altered histone marks by LC–MS. We found that lysine methylation is reduced post-safusidenib, especially H3K9 and H3K27 monomethylation marks (Fig. 1j,k) with concomitant increases in histone acetylation (Extended Data Fig. 2g), suggesting that globally, transcription is enhanced post-safusidenib.

Safusidenib treatment induces differentiation in tumor cells

In exploratory analyses, to examine mechanistic changes induced by safusidenib, we performed single-nuclei RNA sequencing (snRNA-seq) on matched tumor samples (Fig. 2a, Extended Data Fig. 3a–c and Supplementary Table 4). Malignant cells were distinguished from

Table 2 | Summary of common and treatment-related adverse events (TRAE) with respect to neurosurgical intervention and safusidenib

Event	Any grade, *n* (%)	Grade≥3, *n* (%)
Participants with ≥1 TRAE	10 (100%)	4 (40%)
Participants with ≥1 serious safusidenib-related AE		0 (0%)
Participants with ≥1 serious neurosurgery-related AE		1 (10%)
Neurosurgery-related AEs		
Unexpected return to theater	0 (0%)	0 (0%)
Postoperative hematoma	0 (0%)	0 (0%)
Wound infection	0 (0%)	0 (0%)
Unexpected neurological deficit	1 (10%)	1 (10%)
Postoperative infarct	0 (0%)	0 (0%)
Study related, but not safusidenib related		
Post-lumbar-puncture headache	1 (10%)	1 (10%)
Safusidenib-related AEs		
Blurred vision	1 (10%)	0 (0%)
Headache	1 (10%)	0 (0%)
Constipation	1 (10%)	0 (0%)
Gastro-esophageal reflux disease	1 (10%)	0 (0%)
Nausea	1 (10%)	0 (0%)
Anorexia	1 (10%)	0 (0%)
Fatigue	3 (30%)	0 (0%)
ALT increased	3 (30%)	1 (10%)
AST increased	2 (20%)	0 (0%)
Neutrophil count decreased	5 (50%)	0 (0%)
WBC count decreased	1 (10%)	0 (0%)
Arthralgia	3 (30%)	0 (0%)
Alopecia	3 (30%)	0 (0%)
Dry skin	4 (40%)	0 (0%)
Photosensitivity	1 (10%)	0 (0%)
Pruritus	5 (50%)	0 (0%)
Rash	2 (20%)	0 (0%)
Skin hyperpigmentation	0 (0%)	0 (0%)
Generalized muscle weakness	1 (10%)	0 (0%)
Chest wall pain	1 (10%)	0 (0%)

nonmalignant cells by marker expression, comparison with single-cell RNA sequencing[29] and inferred copy number alterations (Fig. 2a and Extended Data Fig. 3d,e). Cluster annotation defined malignant cell states[30] as astrocyte-like (AC-like), oligodendrocyte precursor-like (OPC-like) and progenitor, and nonmalignant cells as astrocytes, oligodendrocytes, OPC, vasculature, neurons and immune cells (Fig. 2a and Extended Data Fig. 3f). Safusidenib altered the proportions of cell types and states (Fig. 2b and Extended Data Fig. 3g–j). Matched pre- and post-safusidenib tumor cells were compared using gene set enrichment analysis (GSEA) including gene sets defining the states of tumor cells, differentiated astrocytes, oligodendrocytes and OPCs (Fig. 2c and Supplementary Table 5). Recapitulating recent analysis[29], we identified 112 significantly enriched gene sets (86 pre-safusidenib, 26 post-safusidenib) (Extended Data Fig. 4a). The AC-like gene set was significantly enriched post-safusidenib and largely showed great concordance (Extended Data Fig. 4b). However, at an individual level, this translated to an AC-like population increase across all tumor cells in five out of nine participants (Extended Data Fig. 3h). Altering the analysis to explicitly consider the matched sampling, we observed upregulation of OPC-like, oligodendrocyte and OPC gene sets post-safusidenib, but crucially no longer the AC-like gene set (34 enriched pre-safusidenib, 209 enriched post-safusidenib; Fig. 2c and Supplementary Table 5).

Analysis of AC-like and OPC-like tumor cells pre- and post-safusidenib supported an induction of differentiation, evidenced by upregulation of oligodendrocyte and OPC gene sets (Extended Data Fig. 4c–f). Post-safusidenib, tumor cells upregulated pathways related to pyrimidine synthesis, and gene sets related to inflammation, while downregulating gene sets associated with ribosomal activity (Fig. 2c,d). Ribosome biogenesis is upregulated in mIDH gliomas, compared with normal tissue and the more proliferative glioblastomas, suggesting that mIDH inhibition normalized baseline ribosomal activity[31].

Inflammatory response associated with safusidenib

Malignant cells after mIDH inhibition transcriptionally upregulate inflammation response genes[2,32], suggested to promote a shift toward the AC-like program. Here, the AC-like population, which had the strongest upregulation of gene sets related to inflammation (Fig. 2d), showed a strong positive correlation between changed interferon (IFN) signaling and AC-like gene set activity after safusidenib (Fig. 2e). Increased IFN signaling in the AC-like population appeared to be activated by the cyclic guanosine monophosphate–adenosine monophosphate (GMP–AMP) synthase (cGAS)–stimulator of interferon genes (STING) pathway[33] and correlated with transcription factor HIF-1α expression, suggesting that the identified inflammatory program is an adaptation to cellular stress (Extended Data Fig. 4g). While the relationship with mIDH and HIF-1α expression has been contentious[34,35], IFN has been shown to promote HIF-1α expression independent of mIDH (ref. 33); thus, the direct mechanism is unclear. Although changes in IFN signaling after safusidenib treatment did not correlate with increased immune cells or their activation globally, we observed local changes (Extended Data Fig. 4h). Spatial transcriptomics with snRNA-seq via CytoSpace[36] identified tumor cells co-localized with immune cells with higher inflammatory response after treatment in one patient ($P < 0.001$, Welch t-test; Extended Data Figs. 4i and 5a and Supplementary Table 6), providing further support that mIDH inhibitors cause cellular stress responses in AC-like tumor cells, resulting in inflammation and possible localized immune cell activation.

Altered immune infiltration post-safusidenib was observed in seven of nine participants, with an increase in macrophages and T cells (Extended Data Fig. 3j), validated by CD68 immunostaining (Fig. 2f). These cell types are probably infiltrative given their perivascular location in two of three post-safusidenib matched spatial transcriptomics samples, validated by immunofluorescence staining (Fig. 2g and Extended Data Figs. 5b,c and 6). These findings support a previous neoadjuvant study of mIDH inhibition, which found higher $CD8^+$ T cell infiltration and gene upregulation of immune cell activation[2]. To address whether immune infiltration was induced by the biopsy, we curated an independent cohort of patients with LGG (Supplementary Table 7), who underwent two surgeries with no intervening treatment (mean = 44 days, range = 14–77 days). Notably, $CD68^+$ cells were increased post-safusidenib and in the surgery-only cohort (Fig. 2f,g and Extended Data Fig. 6), suggesting that surgery alone results in immune infiltration, possibly through a wound healing response[37,38].

Progenitors show cellular adaptability post-safusidenib

We explored whether gene sets related to tumor cell states were consistently regulated by safusidenib. This revealed the unique behavior of the progenitor population, marked by absence of the G1 phase and high expression of *TOP2A*, which upregulated OPC and OPC-like gene sets after treatment and downregulated the differentiated astrocyte gene set (Fig. 2d and Extended Data Figs. 4e,f and 7a,b). This shift was supported by significant upregulation of *BMPER* ($P = 0.002$) and *MYRF* ($P = 0.002$) in the progenitor population post-safusidenib (Extended Data Fig. 7c). *BMPER* expression has a pivotal role in angiogenesis, promotes oligodendroglia differentiation and increases the rate of remyelination via modulation of BMP4 signaling[39]. *MYRF* encodes a transcription factor required for myelination during oligodendrocyte maturation[40].

The strong upregulation of the OPC-like program post-safusidenib led us to investigate the differentiation potential of progenitor cells before ($n = 772$) and after safusidenib ($n = 1{,}130$) using CytoTRACE2 (ref. 41; Fig. 3a). We found that progenitor cells at biopsy had greater differentiation potential than AC-like tumor cells ($P < 0.001$) and behaved more similarly to OPC-like tumor cells ($P = 1$; Extended Data Fig. 7d). Post-safusidenib, progenitor cells increased in differentiation potential ($P < 0.001$; Fig. 3a). We also projected progenitor cells

Fig. 2 | Altered gene programs following safusidenib treatment. a, UMAP plot depicting 158,487 nuclei identified in $n = 9$ matched samples using snRNA-seq from participants pre- and post-safusidenib. Top left: pre- and post-safusidenib conditions; top right: nonmalignant and malignant cells determined by Numbat; bottom: annotated UMAP clusters of glial tumor and normal cell states. **b**, Fraction of each cell state in pre- and post-safusidenib samples ($n = 9$ participants). Cell type legend as in **a**. **c**, Comparison of all tumor cells in matched pre- and post-safusidenib samples using GSEA. Each dot represents a gene set and the color indicates whether the gene set belongs to a glioma program; top enriched pathways are annotated. The x-axis shows the GSEA normalized enrichment score, and the y-axis shows the adjusted P value. The line depicts the significance threshold (adjusted $P = 0.05$). **d**, Dot plot depicting key semantic terms summarizing significant gene sets for each cell type population from GSEA. Each dot represents the proportion of significant pathways related to that term and is color coded to indicate the direction of enrichment—pre- or post-safusidenib. The accompanying bar plot illustrates the counts and enrichment direction of significant gene sets per semantic term for the tumor compartment. **e**, log(FC) in the AC-like program compared with log(FC) in the IFN program in AC-like tumor cells pre-safusidenib relative to post-safusidenib treatment ($n = 9$ participants, t-test). **f**, Representative immunohistochemistry staining of CD68 in the first surgery and biopsy, and the second surgery, from untreated patients (no treatment, surgery only) compared with participant O-01 pre- and post-safusidenib tissue. Quantification percentage $CD68^+$ cells (no treatment, $n = 6$ matched samples; safusidenib, $n = 10$ matched samples). Mean ± s.e.m. (no treatment: 14.6 ± 3.1% at first surgery and biopsy, 30.3 ± 2.6% at surgery; safusidenib: 12.3 ± 3.5% at first surgery and biopsy, 21.6 ± 5.5% at surgery). Individual dots represent matched patient samples. Participant legend as in **e**. **g**, Example of vasculature in participant A-05 pre-safusidenib and post-safusidenib ($n = 3$ per condition). Single-cell spatial maps (Voronoi) of the expression of the CD69 transcript, cell state annotation and protein expression by immunofluorescence (CD31, CD68, mIDH and GFAP), with location in tissue (scale bars, 1 mm; annotation legend in **a**). Inset scale bars, 100 µm.

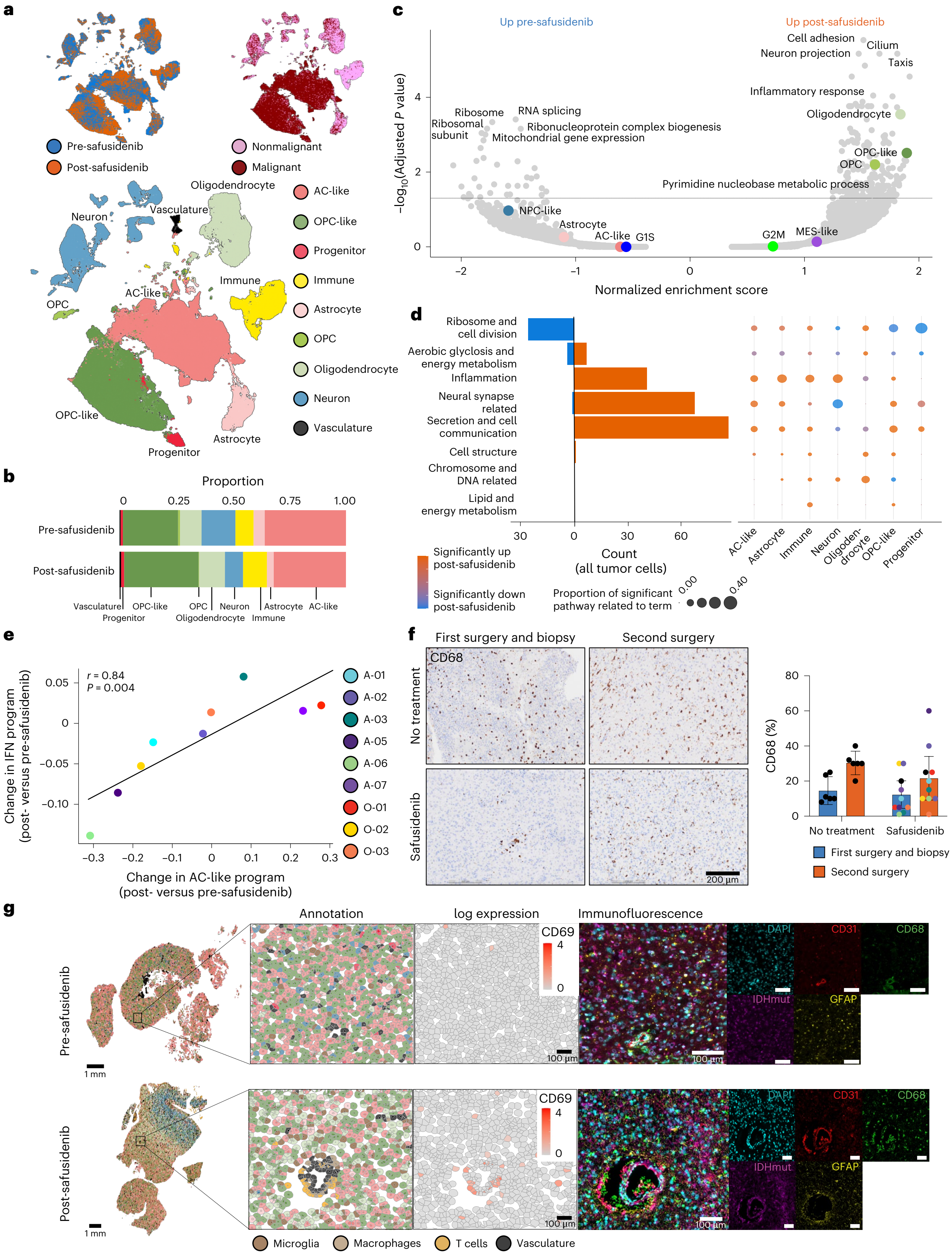
a
Pre-safusidenib
Post-safusidenib
Nonmalignant
Malignant
Oligodendrocyte
Vasculature
Neuron
AC-like
Immune
OPC
OPC-like
Astrocyte
Progenitor
AC-like
OPC-like
Progenitor
Immune
Astrocyte
OPC
Oligodendrocyte
Neuron
Vasculature
b
Proportion
0
0.25
0.50
0.75
1.00
Pre-safusidenib
Post-safusidenib
Vasculature
Progenitor
OPC-like
OPC
Oligodendrocyte
Neuron
Immune
Astrocyte
AC-like
c
Up pre-safusidenib
Up post-safusidenib
Cell adhesion
Cilium
Neuron projection
Taxis
Inflammatory response
Oligodendrocyte
Ribosome
RNA splicing
Ribosomal subunit
Ribonucleoprotein complex biogenesis
Mitochondrial gene expression
OPC-like
OPC
Pyrimidine nucleobase metabolic process
NPC-like
Astrocyte
AC-like
G1S
G2M
MES-like
$-\log_{10}$(Adjusted P value)
4
2
0
−2
−1
0
1
2
Normalized enrichment score
d
Ribosome and cell division
Aerobic glyclosis and energy metabolism
Inflammation
Neural synapse related
Secretion and cell communication
Cell structure
Chromosome and DNA related
Lipid and energy metabolism
30
0
30
60
Count (all tumor cells)
AC-like
Astrocyte
Immune
Neuron
Oligodendrocyte
OPC-like
Progenitor
Significantly up post-safusidenib
Significantly down post-safusidenib
Proportion of significant pathway related to term
0.00
0.40
e
r = 0.84
P = 0.004
Change in IFN program (post- versus pre-safusidenib)
0.05
0
−0.05
−0.10
−0.3
−0.2
−0.1
0
0.1
0.2
0.3
Change in AC-like program (post- versus pre-safusidenib)
A-01
A-02
A-03
A-05
A-06
A-07
O-01
O-02
O-03
f
First surgery and biopsy
Second surgery
CD68
No treatment
Safusidenib
200 µm
CD68 (%)
80
60
40
20
0
No treatment
Safusidenib
First surgery and biopsy
Second surgery
g
Annotation
log expression
Immunofluorescence
Pre-safusidenib
Post-safusidenib
1 mm
CD69
4
0
100 µm
DAPI
CD31
CD68
IDHmut
GFAP
Microglia
Macrophages
T cells
Vasculature

onto a two-dimensional butterfly plot[42], with each quadrant corresponding to a tumor cell state[43] (Fig. 3b), revealing that progenitor cells post-safusidenib showed greater heterogeneity in their tumor cell state (pre-safusidenib $\log_2$(entropy) = 1.83, post-safusidenib $\log_2$(entropy) = 1.96, $P < 0.001$). Together, this points toward increased cellular adaptability in progenitors, probably reflecting a direct response to mIDH inhibition.

Progenitor state shift associated with metabolic environment

To determine whether a shift toward the OPC-like gene set is indicative of treatment response, we examined a published cohort[29] detailing a single responder oligodendroglioma and nonresponder astrocytoma with available single-cell transcriptomics pre- and post-ivosidenib (Extended Data Fig. 7e). In the progenitor population, *MYRF* was increased in the nonresponder patient and largely unchanged in the responder patient (Extended Data Fig. 7f). Furthermore, a shift toward the OPC-like gene program was associated with the nonresponder signature in progenitors, compared with an upregulation of the AC-like program in the responder (Fig. 3c). This suggests that cell state may be associated with response to mIDH inhibition. Given that IDH facilitates metabolite activity through the Krebs cycle, we hypothesized that differential energy consumption may contribute to mIDH inhibition response in certain tumor cell states. To investigate, we generated an independent cohort of LGG ($n = 3$ oligodendroglioma, $n = 8$ astrocytoma) with snRNA-seq (Supplementary Table 8 and Extended Data Fig. 7g), identifying enrichment of glycolysis signatures in normal astrocytes and AC-like cells ($P < 0.001$, Welch t-test) distinct from OPC-like cells, enriched in Krebs ($P < 0.001$) and lactate ($P < 0.001$) gene programs (Fig. 3d and Extended Data Fig. 7h). To validate transcriptional inference of metabolism, we interrogated spatial transcriptomics and metabolomics, performed on serial sections. Binning a continuum of AC-like enriched and OPC-like enriched pixels using transcriptomics, and examining the metabolite abundance across each region, we validated the increased abundance of glucose in AC-like-rich regions, compared with α-KG in OPC-like-rich regions (Fig. 3e,f and Extended Data Fig. 8a). Therefore, metabolic rewiring may be involved in the efficacy of mIDH inhibition.

To further investigate the impact of mIDH inhibition, we compared pre- and post-safusidenib central carbon metabolism. Metabolites associated with aerobic metabolism altered abundance following treatment (Krebs cycle disorders $P = 0.002$; glutaminolysis and cancer $P = 0.005$; Fig. 3g, Extended Data Fig. 8b and Supplementary Table 3), consistent with inhibition of mIDH activity[44,45]. Increased metabolites associated with the reductive Krebs cycle before treatment were reduced post-safusidenib, with concomitant increases in downstream metabolites in the oxidative cycle (Fig. 3h). These data suggest that mechanistically, safusidenib inhibited enzymatic features of tumor mIDH1. To transcriptionally examine pathway changes in the responder and nonresponder samples[29], we compared gene expression associated with the Krebs cycle, glycolysis and lactate production in the progenitor cells (Fig. 3i). The nonresponder sample showed a shift toward Krebs and lactate gene signatures post-mIDH inhibition, while the responder sample remained largely unchanged. Consistent with OPC-like enrichment, safusidenib-treated samples aligned with the ivosidenib nonresponder sample, suggesting on average limited likelihood of durable response in this cohort (Extended Data Fig. 8c,d). Given that these findings are from part A of the clinical trial, future analysis will consider these results in the context of survival outcomes.

Safusidenib treatment decreases synaptic signaling

In neurons, gene sets associated with synaptic signaling were downregulated, coinciding with the upregulation of gene sets associated with neural activity and development in all tumor cells following safusidenib (Fig. 2d). Glioma cells exploit synaptic electrochemical signaling to drive cancer growth and invasion[46–48]. Downregulation of synaptic signaling following safusidenib may indicate a previously unrecognized direct or indirect drug mechanism. Previous studies have shown that 2-HG enhances neuronal excitability in *IDH*-mutated glioma models, with excitability reduced upon mIDH inhibition and associated 2-HG depletion[49]. We identified a reduction in synaptic signaling, supported by reduced levels of the neuromodulator adenosine[50] (Fig. 4a and Extended Data Fig. 9a). Similar global metabolite alterations were observed, including reduced cAMP signaling (Fig. 4b), signifying possible reduced synaptic signaling following safusidenib. Indeed, pathway analysis of metabolites altered by safusidenib revealed synaptic pathways such as neuroinflammation and glutamatergic signaling (Fig. 4c), suggesting that neural activity is altered at a metabolic level post-safusidenib.

To overcome differences in the composition of the microenvironment, we investigated gene expression changes related to synaptic signaling spatially. We identified niches with similar transcriptional dynamics across three patients with spatial transcriptomics on tumor tissue pre- and post-safusidenib (Fig. 4d and Extended Data Fig. 9b). This facilitated the identification of T7 in which neurons constituted >25% of all cell types but tumor cells were still pervasive (Fig. 4e and Extended Data Fig. 9c). Investigating the expression of neuronal layer markers revealed a cortical layer formation, indicating that this niche defines the leading edge of the tumor (Fig. 4f and Extended Data Fig. 9d). Locating neurons in the T7 niche allowed the investigation of changes pre- and post-safusidenib in similar microenvironments. Consistent with our snRNA-seq data for different neuron populations (Extended Data Fig. 9e), the average expression of synaptic signaling

Fig. 3 | Safusidenib alters transcriptional patterns in progenitor cells. **a**, UMAP plot of snRNA-seq tumor populations only, colored by differentiation potential potency scores calculated using CytoTRACE2 (left). The accompanying density plots illustrate the distribution of potency scores within the progenitor population under pre-safusidenib and post-safusidenib conditions. **b**, Two-dimensional butterfly plot visualization, with each quadrant corresponding to a tumor cell state: mesenchymal-like (MES-like), neural-progenitor-like (NPC-like), astrocyte-like (AC-like) and oligodendrocyte-progenitor-like (OPC-like) as defined by Neftel et al.[43]. SC1 and SC2 represent single-cell gene signature scores 1 and 2 also defined by Neftel et al.[43]. The position of each progenitor nucleus reflects its relative signature scores in the pre-safusidenib and post-safusidenib samples. Cell density is indicated by contour lines. **c**, Progenitor cell transcriptional program alignment with tumor cell states in responder (positive values) compared with nonresponder (negative values) Spitzer et al.[29] samples. **d**, Ternary plots comparing transcriptional metabolic programs; Krebs (K), lactate (L) and glycolysis (G), in AC-like and OPC-like tumor cells from 11 untreated LGG tumors. **e**, Quantification of metabolite (α-KG (m/z: 254.08; adducts: M + ACN + Na) and glucose (m/z: 203.05; adducts: M + Na)) intensity score in 100 × 100 µm regions of spatial metabolomics, assigned to AC-like/OPC-like tumor cell ratios calculated by serial spatial transcriptomics sections on samples A–E (example ratio regions annotated, below). Scale bars, 10 µm. Example tumor region with annotated cell type (right, above) and glucose spatial intensity (right, below). Scale bar, 100 µm. **f**, Quantification of α-KG and glucose in AC-like compared with OPC-like tumor cell states calculated based on spatial transcriptomics annotation relative to spatial metabolomics (Welch t-test). Mean ± s.e.m. Cell type legend as in **e**. **g**, Barcode plot of pathways 'Krebs cycle disorders' and 'glutaminolysis and cancer'. Significance calculated via GSEA ($n = 9$ participants, permutation-based testing). **h**, Simplified schema of the citric acid cycle and nucleotide synthesis. Blue, increased abundance pre-safusidenib; orange, increased abundance post-safusidenib. UMP, uridine monophosphate; CIT, citrate; OAA, oxaloacetate; MAL, malate; FUM, fumarate; SUC, succinate; ICIT, isocitrate; *cis*-ACO, *cis*-aconitate; ND, not detected. Data from LC–MS untargeted analysis ($n = 9$ participants). **i**, Ternary plot comparing transcriptional metabolic programs in progenitor cells of K, L and G in responder and nonresponder Spitzer et al.[29] samples pre-mIDH inhibitor compared with post-mIDH inhibitor. Inh, inhibitor.

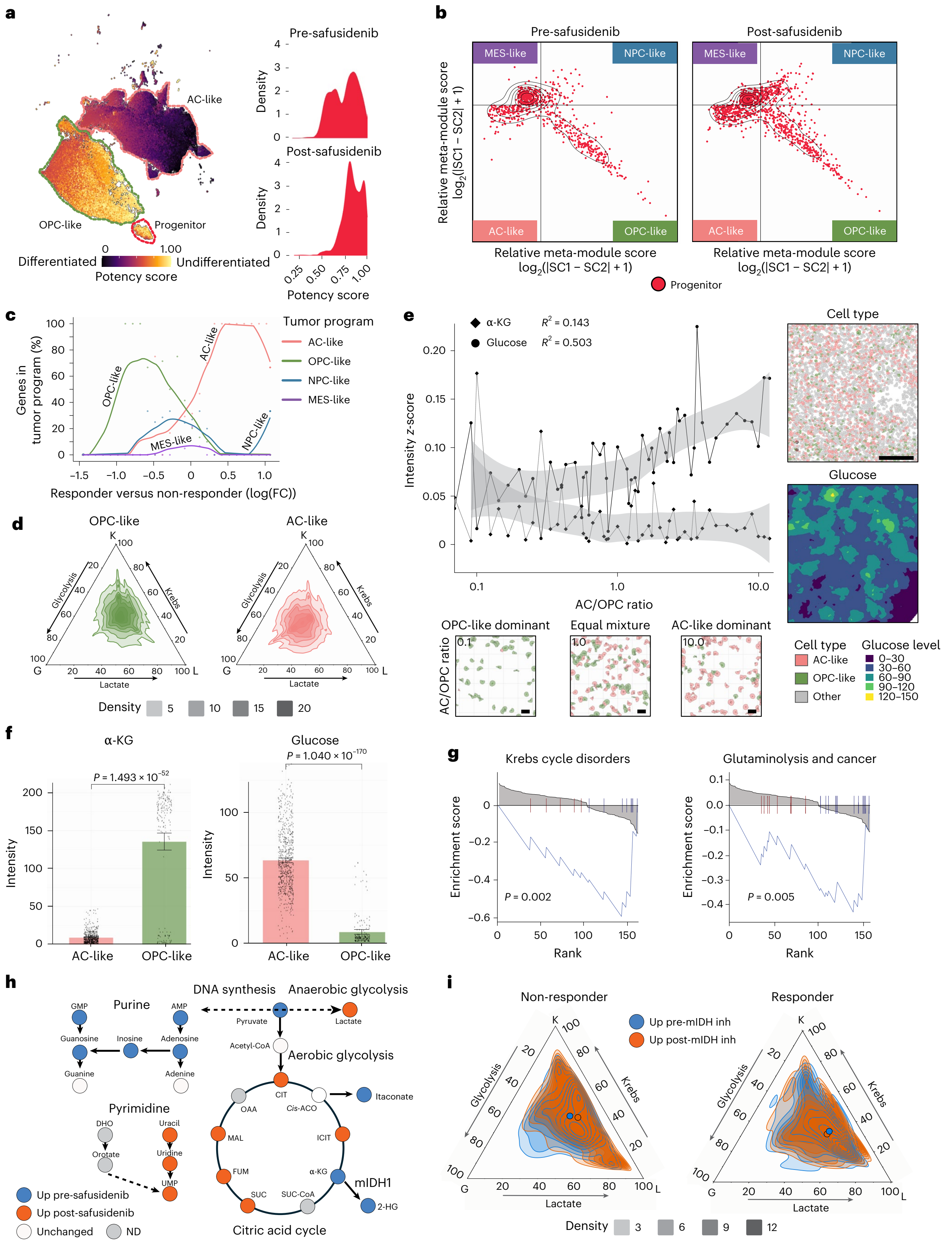
a
AC-like
OPC-like
Progenitor
0
1.00
Differentiated
Undifferentiated
Potency score
Pre-safusidenib
Post-safusidenib
Density
4
3
2
1
0
0.25
0.50
0.75
1.00
Potency score
b
Pre-safusidenib
Post-safusidenib
MES-like
NPC-like
AC-like
OPC-like
Relative meta-module score
$\log_2(|SC1 - SC2| + 1)$
Progenitor
c
Genes in tumor program (%)
100
80
60
40
20
0
OPC-like
AC-like
MES-like
NPC-like
Tumor program
AC-like
OPC-like
NPC-like
MES-like
−1.5
−1.0
−0.5
0
0.5
1.0
Responder versus non-responder (log(FC))
d
OPC-like
AC-like
K
100
80
60
40
20
Glycolysis
Krebs
G
L
Lactate
Density
5
10
15
20
e
α-KG $R^2 = 0.143$
Glucose $R^2 = 0.503$
Intensity z-score
0.20
0.15
0.10
0.05
0
0.1
1.0
10.0
AC/OPC ratio
Cell type
Glucose
OPC-like dominant
Equal mixture
AC-like dominant
AC/OPC ratio
0.1
1.0
10.0
Cell type
AC-like
OPC-like
Other
Glucose level
0–30
30–60
60–90
90–120
120–150
f
α-KG
$P = 1.493 \times 10^{-52}$
Intensity
200
150
100
50
0
AC-like
OPC-like
Glucose
$P = 1.040 \times 10^{-170}$
100
50
0
AC-like
OPC-like
g
Krebs cycle disorders
Glutaminolysis and cancer
Enrichment score
0
−0.2
−0.4
−0.6
P = 0.002
0.1
0.0
−0.1
−0.2
−0.3
−0.4
P = 0.005
0
50
100
150
Rank
h
Purine
GMP
AMP
Guanosine
Inosine
Adenosine
Guanine
Adenine
DNA synthesis
Anaerobic glycolysis
Pyruvate
Lactate
Acetyl-CoA
Aerobic glycolysis
CIT
Cis-ACO
Itaconate
OAA
ICIT
MAL
FUM
α-KG
mIDH1
SUC
SUC-CoA
2-HG
Citric acid cycle
Pyrimidine
DHO
Uracil
Orotate
Uridine
UMP
Up pre-safusidenib
Up post-safusidenib
Unchanged
ND
i
Non-responder
Responder
Up pre-mIDH inh
Up post-mIDH inh
K
100
80
60
40
20
Glycolysis
Krebs
G
L
Lactate
Density
3
6
9
12

inferred by CytoSPACE was downregulated in the T7 niche in neurons before and after safusidenib in one participant, for which samples at both timepoints contained sufficient leading-edge tissue (log(fold change (FC)) = −0.360; Fig. 4g). In addition, we investigated synaptic signaling genes included in our spatial transcriptomics gene panel, which showed decreases in their average expression in neurons in the T7 niche post-safusidenib (Fig. 4h).

As our findings suggest a decrease in synaptic signaling, we performed post hoc analysis to assess the influence of safusidenib on the excitability of cortical neurons. Whole-cell patch-clamp recordings were performed from pyramidal neurons within ex vivo tissue slices from pre-safusidenib samples ($n = 11$ neurons; 4 participants) and post-safusidenib samples ($n = 14$ neurons; 3 participants; Fig. 4i and Extended Data Fig. 10). Following safusidenib, there was a dampening in the overall excitability of neurons with a significant decrease in the evoked firing rate ($P = 0.018$; Fig. 4j,k). Congruently, there was a significant increase in the rheobase (100 ± 21 versus 163 ± 20 pA; $P = 0.043$; Fig. 4l) and a decrease in membrane resistance (107 ± 14 versus 65 ± 7 MΩ; $P = 0.009$; Fig. 4m) following treatment. Safusidenib did not influence the resting membrane potential (−66.6 ± 1.2 versus −67.5 ± 1.0 mV; $P = 0.551$; Fig. 4n), action potential width (1.4 ± 0.04 versus 1.6 ± 0.05; $P = 0.124$) or threshold (−42.4 ± 0.9 versus −43.5 ± 0.5 mV; $P = 0.199$). Combined with the downregulation of synaptic signaling genes and metabolites, the decrease in neuronal excitability following treatment illustrates that the tumor electrical environment is altered by safusidenib.

Discussion

By combining multi-omic techniques on paired samples from a perioperative clinical trial, we examined direct drug mechanisms of mIDH inhibitor treatment in mIDH1 gliomas. Confirming earlier results[4], we show that safusidenib is safe and well tolerated and that the perioperative design is feasible and safe, meeting the primary study endpoint. While funding, logistical considerations and ethical justification for the above standard-of-care surgical procedures remain debated[14–16], this study supports a paradigm shift[14,15] in clinical trial design for gliomas, offering a robust framework for evaluating drug efficacy in the brain. Importantly, it underscores how repetitive tissue sampling, although traditionally limited in neuro-oncology, can inform therapeutic development, provided safety, participant engagement and experience are prioritized. This concept will be further evaluated in the GIANT trial (NCT06816927), assessing feasibility in newly diagnosed glioblastoma.

We confirm that mIDH inhibition results in 2-HG reduction, altered metabolism, decreased histone monomethylation and induction of differentiation in most tumor cell states, establishing biological adaptations in both astrocytomas and oligodendrogliomas. The investigation of matched participant samples enabled us to resolve the effect of mIDH inhibition on histone modifications, which probably led to transcriptional impacts driving differences in individual tumor populations[51]. We revealed that progenitors show distinct behavior, including dedifferentiation and increased heterogeneity, pointing to increased cellular adaptability after mIDH inhibition.

Predictive biomarkers are required to identify likely responders to mIDH inhibition and reveal resistance mechanisms. Although survival outcome data for this trial are immature, reanalysis of mIDH inhibitor-treated responder and nonresponder patients[29] revealed the importance of the dominant cell state in tumor response. The response phenotype showed a reduced dynamic change in metabolite programs and increased AC-like signatures in progenitors, suggesting that metabolic adaptation to mIDH inhibition may be a poor indicator of response, thus providing insight into differential response in patients with oligodendroglioma and astrocytoma, observed in the INDIGO trial[3]. Greater adaptability in utilization of the Krebs cycle, probably associated with increased OPC-like enrichment, was associated with the nonresponder phenotype, suggesting that response may be independent of the 2-HG reduction observed across all patients. Whether 2-HG serves as a reliable predictor of outcome will be determined when part B of the trial is completed.

Although mIDH inhibitors are entering clinical practice, given low-response rates and almost inevitable disease progression, rational combination studies are required. Combinations with immune checkpoint inhibitors (NCT05484622) have commenced based on findings that reducing 2-HG may restore T cell function[2]. Here we confirm that T cells and macrophages traffic into tumors in response to surgery and mIDH inhibition; however, parsing out the contribution of the surgical procedure, and sufficiency to prime a response to immune checkpoint inhibitors, remains to be tested. Combination studies harnessing metabolic vulnerabilities induced by mIDH inhibition represent alternative strategies with recent evidence for targeting the hyperdependency of mIDH tumors to de novo pyrimidine nucleotide synthesis[52]. Post-safusidenib, we find an abundance of metabolites in the salvage arm of the pyrimidine pathway and sparsity of purine intermediates; thus, the combination with pyrimidine inhibitors would need to be carefully considered. This contrasts with the inhibition of glutaminase, in which inhibition is synergistic[53]. These findings must also consider emerging resistance mechanisms including *IDH1/2* second-site mutations[54,55] or isoform switching[56] seen in leukemia and cholangiocarcinoma. Persistent low 2-HG levels in patients who have progressed on safusidenib[4] suggest mIDH-independent resistance in glioma, highlighting the need to explore alternative mechanisms and combination strategies.

Glioma–neuron interactions represent a new hallmark of cancer[46–48]. We show that mIDH inhibition reduces neural excitability in patients, potentially contributing to the observed decrease in synaptic

Fig. 4 | Altered neuron signaling following safusidenib treatment. a, Spatial metabolomics detecting adenosine intensity (top) in participant O-01 pre- and post-safusidenib. Bottom: kernel density plot of smoothed intensity. **b**, Barcode plot of the 'Adora2b-mediated anti-inflammatory cytokine production' pathway in LC–MS metabolomics data (GSEA permutation-based testing, $n = 9$ participants) and normalized metabolite ratio of cyclic AMP pre- and post-safusidenib ($n = 9$ participants, paired t-test). Each box indicates the IQR, the center line is the median and the whiskers extend to the furthest points within 1.5 × IQR. **c**, Barcode plot of the 'Neuroinflammation and glutamatergic signaling' pathway in LC–MS metabolomics data (GSEA permutation-based testing, $n = 9$ participants). **d**, Spatial map of transcript niches of three participants pre- and post-safusidenib computed using GraphSAGE. **e**, Cell assignments to transcript-based niches are represented as normalized proportions. Bar plot of the proportion of cells in each niche. **f**, Spatial maps of neurons (red) in pre- and post-safusidenib samples of participant O-01 with associated density contour plot (left) and key neuronal layer markers (right). **g**, Average log expression of the 'synaptic signaling' pathway for neurons in the T7 niche pre- and post-safusidenib from participant O-01, inferred through CytoSPACE integration. Insets: cell-type annotations, with donut plots of neuron subtype proportions within the region. **h**, Dot plots of the proportion of neurons per transcript niche expressing synaptic signaling genes in matched pre- and post-safusidenib samples. The dot colors represent scaled average log expression. **i**, Example layer 2/3 pyramidal neuron filled with 5-(and-6)-tetramethylrhodamine biocytin. Inset: whole-cell patch-clamp voltage response to current step injection (130 pA, representative of $n = 25$ for $n = 7$ participants). Scale, 20 mV, 200 ms. **j**, Example whole-cell patch-clamp recordings (120 pA steps) from pyramidal neurons obtained from a single patient pre- and post-safusidenib. **k**, Firing rate (20 pA steps, 1,200 ms) from (left) the neurons and patient shown in **j** and (right) average of all neurons (pre-safusidenib ($n = 11$ neurons; 4 participants) and post-safusidenib ($n = 14$ neurons; 3 participants), ANOVA). Mean ± s.e.m. **l**–**n**, Rheobase (t-test) (**l**), membrane resistance (t-test) (**m**) and resting membrane potential (RMP) (t-test) in neurons (**n**) from tissue analyzed pre- and post-safusidenib. Panels **l** and **m** show mean ± s.e.m.

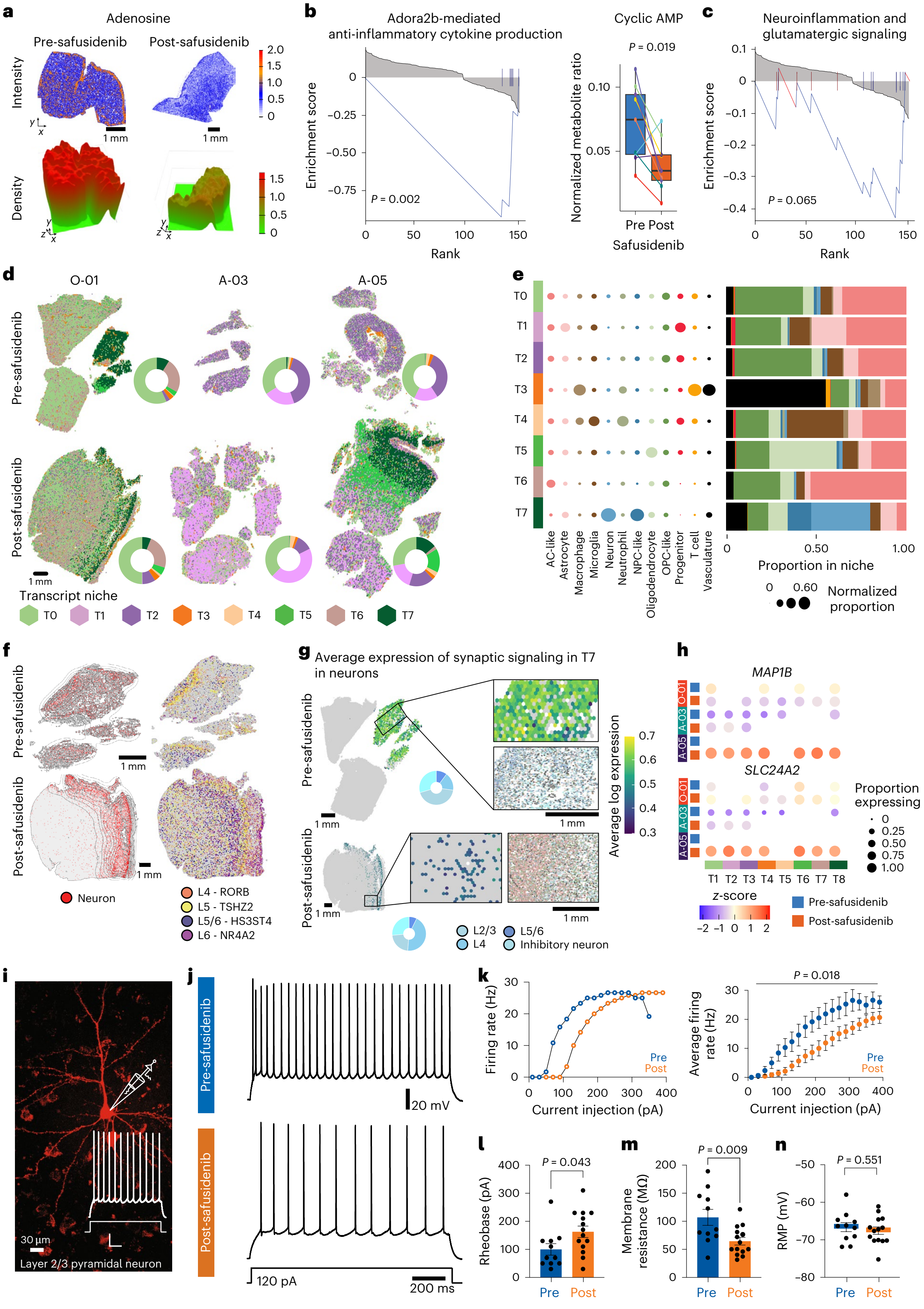
a
Adenosine
Pre-safusidenib
Post-safusidenib
Intensity
Density
2.0
1.5
1.0
0.5
0
1 mm
b
Adora2b-mediated anti-inflammatory cytokine production
Enrichment score
P = 0.002
Rank
Cyclic AMP
P = 0.019
Normalized metabolite ratio
Pre Post
Safusidenib
c
Neuroinflammation and glutamatergic signaling
P = 0.065
Rank
d
O-01
A-03
A-05
Transcript niche
T0 T1 T2 T3 T4 T5 T6 T7
e
AC-like
Astrocyte
Macrophage
Microglia
Neuron
Neutrophil
NPC-like
Oligodendrocyte
OPC-like
Progenitor
T cell
Vasculature
Proportion in niche
Normalized proportion
f
Neuron
L4 - RORB
L5 - TSHZ2
L5/6 - HS3ST4
L6 - NR4A2
g
Average expression of synaptic signaling in T7 in neurons
Average log expression
L2/3
L4
L5/6
Inhibitory neuron
h
MAP1B
SLC24A2
O-01
A-03
A-05
Proportion expressing
z-score
Pre-safusidenib
Post-safusidenib
T1 T2 T3 T4 T5 T6 T7 T8
i
30 μm
Layer 2/3 pyramidal neuron
j
20 mV
120 pA
200 ms
k
Firing rate (Hz)
Current injection (pA)
Pre
Post
Average firing rate (Hz)
P = 0.018
l
Rheobase (pA)
P = 0.043
m
Membrane resistance (MΩ)
P = 0.009
n
RMP (mV)
P = 0.551

signaling following treatment. This may reflect reduced synaptic drive from pyramidal neurons, which form excitatory connections with neighboring cells. Intriguingly, mIDH inhibition decreased synaptic signaling in neurons after mIDH inhibition, while increasing gene expression of those pathways in tumor cells. While warranting further investigation, we propose that this upregulation is a result of tumor cells receiving reduced synaptic input from neurons possibly using a mechanism akin to homeostatic synaptic plasticity[57]. Together, these findings highlight how mIDH inhibition alters the tumor microenvironment and could influence seizure potential in patients. Indeed, 2-HG has been found to promote neuronal spiking activity surrounding mIDH glioma, eliminated with mIDH inhibitors in vitro[58], and reduced seizures in preclinical models[49]. Furthermore, increased concentrations of naturally occurring L-2-HG in body fluids have been linked with the disease L-2-hydroxyglutaric aciduria, resulting in cerebellar dysfunction, including seizures[59]. This mechanistic link is underscored by recent results from the INDIGO study, which reported a significant reduction in seizures in patients on the vorasidenib arm[60].

This study is limited by the small sample size, mitigated by leveraging matched samples and showing high concordance with previous studies. However, further long-term clinical outcome data will be required to confirm our hypothesis on resistance mechanisms linked to metabolism shift following mIDH inhibition. While our findings were not modeled in vitro, where low-grade mIDH glioma is challenging to replicate, we partially overcome this by performing multitudes of measurements on our matched participant samples that consistently corroborated our findings.

In conclusion, these results not only reveal direct and indirect consequences of mIDH inhibition, but also provide proof of concept that perioperative approaches can inform drug development in glioma.

Online content

Any methods, additional references, Nature Portfolio reporting summaries, source data, extended data, supplementary information, acknowledgements, peer review information; details of author contributions and competing interests; and statements of data and code availability are available at https://doi.org/10.1038/s41591-025-03884-4.

References

1. de la Fuente, M. I. et al. Olutasidenib (FT-2102) in patients with relapsed or refractory IDH1-mutant glioma: a multicenter, open-label, phase Ib/II trial. *Neuro. Oncol.* **25**, 146–156 (2023).
2. Mellinghoff, I. K. et al. Vorasidenib and ivosidenib in IDH1-mutant low-grade glioma: a randomized, perioperative phase 1 trial. *Nat. Med.* **29**, 615–622 (2023).
3. Mellinghoff, I. K. et al. Vorasidenib in IDH1- or IDH2-mutant low-grade glioma. *N. Engl. J. Med.* **389**, 589–601 (2023).
4. Natsume, A. et al. The first-in-human phase I study of a brain-penetrant mutant IDH1 inhibitor DS-1001 in patients with recurrent or progressive IDH1-mutant gliomas. *Neuro. Oncol.* **25**, 326–336 (2023).
5. Dang, L. et al. Cancer-associated IDH1 mutations produce 2-hydroxyglutarate. *Nature* **462**, 739–744 (2009).
6. Rohle, D. et al. An inhibitor of mutant IDH1 delays growth and promotes differentiation of glioma cells. *Science* **340**, 626–630 (2013).
7. Xu, W. et al. Oncometabolite 2-hydroxyglutarate is a competitive inhibitor of alpha-ketoglutarate-dependent dioxygenases. *Cancer Cell* **19**, 17–30 (2011).
8. Bleeker, F. E. et al. The prognostic IDH1(R132) mutation is associated with reduced NADP$^+$-dependent IDH activity in glioblastoma. *Acta Neuropathol.* **119**, 487–494 (2010).
9. Bunse, L. et al. Suppression of antitumor T cell immunity by the oncometabolite (R)-2-hydroxyglutarate. *Nat. Med.* **24**, 1192–1203 (2018).
10. Kohanbash, G. et al. Isocitrate dehydrogenase mutations suppress STAT1 and CD8$^+$ T cell accumulation in gliomas. *J. Clin. Invest.* **127**, 1425–1437 (2017).
11. Notarangelo, G. et al. Oncometabolite d-2HG alters T cell metabolism to impair CD8$^+$ T cell function. *Science* **377**, 1519–1529 (2022).
12. Watanabe, T., Nobusawa, S., Kleihues, P. & Ohgaki, H. IDH1 mutations are early events in the development of astrocytomas and oligodendrogliomas. *Am. J. Pathol.* **174**, 1149–1153 (2009).
13. de la Fuente, M. I. et al. The role of vorasidenib in the treatment of isocitrate dehydrogenase-mutant glioma. *Neuro. Oncol.* **27**, 1135–1148 (2024).
14. Hotchkiss, K. M. et al. A brave new framework for glioma drug development. *Lancet Oncol.* **25**, e512–e519 (2024).
15. Mweempwa, A., Rosenthal, M. A., Dimou, J., Drummond, K. J. & Whittle, J. R. Perioperative clinical trials for glioma: raising the bar. *J. Clin. Neurosci.* **89**, 144–150 (2021).
16. Singh, K. et al. Correcting the drug development paradigm for glioblastoma requires serial tissue sampling. *Nat. Med.* **29**, 2402–2405 (2023).
17. Machida, Y. et al. A potent blood–brain barrier-permeable mutant IDH1 inhibitor suppresses the growth of glioblastoma with IDH1 mutation in a patient-derived orthotopic xenograft model. *Mol. Cancer Ther.* **19**, 375–383 (2020).
18. Cain, S. A. et al. A perioperative study of safusidenib in patients with IDH1-mutated glioma. *Future Oncol.* **20**, 2533–2545 (2024).
19. Louis, D. N. et al. The 2021 WHO classification of tumors of the central nervous system: a summary. *Neuro. Oncol.* **23**, 1231–1251 (2021).
20. Wen, P. Y. et al. RANO 2.0: update to the response assessment in neuro-oncology criteria for high- and low-grade gliomas in adults. *J. Clin. Oncol.* **41**, 5187–5199 (2023).
21. Kost, R. G. & de Rosa, J. C. Impact of survey length and compensation on validity, reliability, and sample characteristics for Ultrashort-, Short-, and Long-Research Participant Perception Surveys. *J. Clin. Transl. Sci.* **2**, 31–37 (2018).
22. Kost, R. G. et al. Assessing participant-centered outcomes to improve clinical research. *N. Engl. J. Med.* **369**, 2179–2181 (2013).
23. Capper, D. et al. 2-Hydroxyglutarate concentration in serum from patients with gliomas does not correlate with IDH1/2 mutation status or tumor size. *Int. J. Cancer* **131**, 766–768 (2012).
24. Lu, T. et al. Matrix selection for the visualization of small molecules and lipids in brain tumors using untargeted MALDI-TOF mass spectrometry imaging. *Metabolites* **13**, 1139 (2023).
25. Badur, M. G. et al. Oncogenic R132 IDH1 mutations limit NADPH for de novo lipogenesis through (D)2-hydroxyglutarate production in fibrosarcoma cells. *Cell Rep.* **25**, 1680 (2018).
26. Hvinden, I. C., Cadoux-Hudson, T., Schofield, C. J. & McCullagh, J. S. O. Metabolic adaptations in cancers expressing isocitrate dehydrogenase mutations. *Cell Rep. Med* **2**, 100469 (2021).
27. Noushmehr, H. et al. Identification of a CpG island methylator phenotype that defines a distinct subgroup of glioma. *Cancer Cell* **17**, 510–522 (2010).
28. Chowdhury, R. et al. The oncometabolite 2-hydroxyglutarate inhibits histone lysine demethylases. *EMBO Rep.* **12**, 463–469 (2011).
29. Spitzer, A. et al. Mutant IDH inhibitors induce lineage differentiation in IDH-mutant oligodendroglioma. *Cancer Cell* **42**, 904–914.e9 (2024).
30. Couturier, C. P. et al. Single-cell RNA-seq reveals that glioblastoma recapitulates a normal neurodevelopmental hierarchy. *Nat. Commun.* **11**, 3406 (2020).
31. Paraqindes, H. et al. Isocitrate dehydrogenase wt and IDHmut adult-type diffuse gliomas display distinct alterations in ribosome biogenesis and 2′O-methylation of ribosomal RNA. *Neuro. Oncol.* **25**, 2191–2206 (2023).

32. Wu, J. et al. Evolving cell states and oncogenic drivers during the progression of IDH-mutant gliomas. *Nat. Cancer.* **6**, 145–157 (2025).
33. Yeh, Y. H., Hsiao, H. F., Yeh, Y. C., Chen, T. W. & Li, T. K. Inflammatory interferon activates HIF-1alpha-mediated epithelial-to-mesenchymal transition via PI3K/AKT/mTOR pathway. *J. Exp. Clin. Cancer Res.* **37**, 70 (2018).
34. Koivunen, P. et al. Transformation by the (R)-enantiomer of 2-hydroxyglutarate linked to EGLN activation. *Nature* **483**, 484–488 (2012).
35. Williams, S. C. et al. R132H-mutation of isocitrate dehydrogenase-1 is not sufficient for HIF-1alpha upregulation in adult glioma. *Acta Neuropathol.* **121**, 279–281 (2011).
36. Vahid, M. R. et al. High-resolution alignment of single-cell and spatial transcriptomes with CytoSPACE. *Nat. Biotechnol.* **41**, 1543–1548 (2023).
37. Aosasa, S. et al. Activation of monocytes and endothelial cells depends on the severity of surgical stress. *World J. Surg.* **24**, 10–16 (2000).
38. Xu, J. et al. Astrocyte-derived CCL2 participates in surgery-induced cognitive dysfunction and neuroinflammation via evoking microglia activation. *Behav. Brain Res.* **332**, 145–153 (2017).
39. Govier-Cole, A. E. et al. Inhibiting bone morphogenetic protein 4 type I receptor signaling promotes remyelination by potentiating oligodendrocyte differentiation. *eNeuro* **6**, e0399-18 (2019).
40. Bujalka, H. et al. MYRF is a membrane-associated transcription factor that autoproteolytically cleaves to directly activate myelin genes. *PLoS Biol.* **11**, e1001625 (2013).
41. Gulati, G. S. et al. Single-cell transcriptional diversity is a hallmark of developmental potential. *Science* **367**, 405–411 (2020).
42. Abdelfattah, N. et al. Single-cell analysis of human glioma and immune cells identifies S100A4 as an immunotherapy target. *Nat. Commun.* **13**, 767 (2022).
43. Neftel, C. et al. An integrative model of cellular states, plasticity, and genetics for glioblastoma. *Cell* **178**, 835–849.e21 (2019).
44. Miyata, S. et al. Comprehensive metabolomic analysis of IDH1^{R132H} clinical glioma samples reveals suppression of β-oxidation due to carnitine deficiency. *Sci. Rep.* **9**, 9787 (2019).
45. Reitman, Z. J. et al. Profiling the effects of isocitrate dehydrogenase 1 and 2 mutations on the cellular metabolome. *Proc. Natl Acad. Sci. USA* **108**, 3270–3275 (2011).
46. Krishna, S. et al. Glioblastoma remodelling of human neural circuits decreases survival. *Nature* **617**, 599–607 (2023).
47. Taylor, K. R. et al. Glioma synapses recruit mechanisms of adaptive plasticity. *Nature* **623**, 366–374 (2023).
48. Venkatesh, H. S. et al. Electrical and synaptic integration of glioma into neural circuits. *Nature* **573**, 539–545 (2019).
49. Drumm, M. R. et al. Postoperative risk of IDH-mutant glioma-associated seizures and their potential management with IDH-mutant inhibitors. *J. Clin. Invest.* **133**, e168035 (2023).
50. Theparambil, S. M. et al. Adenosine signalling to astrocytes coordinates brain metabolism and function. *Nature* **632**, 139–146 (2024).
51. Liu, I. et al. The landscape of tumor cell states and spatial organization in H3-K27M mutant diffuse midline glioma across age and location. *Nat. Genet.* **54**, 1881–1894 (2022).
52. Shi, D. D. et al. De novo pyrimidine synthesis is a targetable vulnerability in IDH mutant glioma. *Cancer Cell* **40**, 939–956.e16 (2022).
53. McBrayer, S. K. et al. Transaminase inhibition by 2-hydroxyglutarate impairs glutamate biosynthesis and redox homeostasis in glioma. *Cell* **175**, 101–116.e25 (2018).
54. Choe, S. et al. Molecular mechanisms mediating relapse following ivosidenib monotherapy in IDH1-mutant relapsed or refractory AML. *Blood Adv.* **4**, 1894–1905 (2020).
55. Intlekofer, A. M. et al. Acquired resistance to IDH inhibition through trans or cis dimer-interface mutations. *Nature* **559**, 125–129 (2018).
56. Harding, J. J. et al. Isoform switching as a mechanism of acquired resistance to mutant isocitrate dehydrogenase inhibition. *Cancer Discov.* **8**, 1540–1547 (2018).
57. Turrigiano, G. G., Leslie, K. R., Desai, N. S., Rutherford, L. C. & Nelson, S. B. Activity-dependent scaling of quantal amplitude in neocortical neurons. *Nature* **391**, 892–896 (1998).
58. Mortazavi, A. et al. IDH-mutated gliomas promote epileptogenesis through d-2-hydroxyglutarate-dependent mTOR hyperactivation. *Neuro. Oncol.* **24**, 1423–1435 (2022).
59. Ahmed, S. et al. L-2-hydroxyglutaric aciduria—review of literature and case series. *Ann. Med. Surg.* **85**, 712–717 (2023).
60. Mellinghoff, I. K. et al. A global, randomized, double-blinded, phase 3 study of vorasidenib versus placebo in patients with adult-type diffuse glioma with an IDH1/2 mutation (indigo): updated efficacy results. *Neuro. Oncol.* **26**, viii108–viii109 (2024).

Katharine J. Drummond[1,2,14] ✉, **Montana Spiteri**[3], **Sarah A. Cain**[1], **Jordan Jones**[1,2], **Sammy Shaya**[4], **Monique Topp**[4], **Tianyao Lu**[3], **Robert Tobler**[3], **Adam L. Valkovic**[3], **Zachery Moore**[3,5], **Oluwaseun E. Fatunla**[3,5], **Jurgen Kriel**[3,5], **Joel J. D. Moffet**[3,5], **Heidi McAlpine**[1,6], **Marius Rosier**[6], **Hefei Guan**[6], **James Dimou**[1,2], **Verena Schadewaldt**[1,2], **Samuel Roberts-Thomson**[7], **David McArdle**[8,9], **Elaine Lui**[8,9], **Moritz Voelker-Albert**[10], **Simone di Sanzo**[10], **Brunda Nijagal**[11], **Vinod K. Narayana**[11], **Camilla B. Mitchell**[12,13], **Joseph H. A. Vissers**[12,13], **Sean Grimmond**[13], **Mark A. Rosenthal**[4], **Lucy M. Palmer**[6], **Sarah A. Best**[3,5,14], **Saskia Freytag**[3,5,14] & **James R. Whittle**[3,4,5,14] ✉

[1]Department of Neurosurgery, Royal Melbourne Hospital, Melbourne, Victoria, Australia. [2]Department of Surgery, University of Melbourne, Melbourne, Victoria, Australia. [3]Personalised Oncology Division, WEHI, Melbourne, Victoria, Australia. [4]Department of Medical Oncology, Peter MacCallum Cancer Centre, Melbourne, Victoria, Australia. [5]Department of Medical Biology, University of Melbourne, Melbourne, Victoria, Australia. [6]The Florey Institute of Neuroscience and Mental Health, The Florey Department of Neuroscience and Mental Health, University of Melbourne, Melbourne, Victoria, Australia. [7]Department of Anatomical Pathology, Royal Melbourne Hospital, Melbourne, Victoria, Australia. [8]Department of Medical Imaging, Royal Melbourne Hospital, Melbourne, Victoria, Australia. [9]Department of Radiology, University of Melbourne, Melbourne, Victoria, Australia. [10]MoleQlar Analytics GmbH, Munich, Germany. [11]Metabolomics Australia, Bio21 Molecular Science and Biotechnology Institute, The University of Melbourne, Melbourne, Victoria, Australia. [12]Department Clinical Pathology, MDHS, University of Melbourne, Melbourne, Victoria, Australia. [13]Collaborative Centre for Genomic Cancer Medicine, MDHS, University of Melbourne, Melbourne, Victoria, Australia. [14]These authors jointly supervised this work: Katharine J. Drummond, Sarah A. Best, Saskia Freytag, James R. Whittle. ✉e-mail: kate.drummond@mh.org.au; whittle.j@wehi.edu.au

Methods

Trial design and oversight

This is a single-arm, single-center, open-label, perioperative study designed to investigate the safety, tolerability and biological activity of safusidenib in patients with *IDH1*-mutated LGG (ClinicalTrials.gov, NCT05577416)[18]. The first participant was enrolled on 21 December 2022, and the last participant completed resection on 9 April 2024. The clinical data cutoff date was 8 November 2024. The study was conducted according to the International Council on Harmonisation of Good Clinical Practice guidelines and the principles of the Declaration of Helsinki with ethics approval from The Royal Melbourne Hospital Human Research Ethics Committee (HREC 2022.003). All participants provided written informed consent.

Participants

Adults (≥18 years) with an Eastern Cooperative Oncology Group (ECOG) performance status of 0–1 and MRI evidence of low-grade glioma (aLGG) requiring nonurgent surgical resection were eligible. Patients with previous surgery alone and known IDH1-mutant aLGG were also included. Key exclusions were radiological features of high-grade glioma, previous chemotherapy or radiotherapy, and cerebellar or brainstem tumors. Eligible patients required adequate hepatic and kidney function, and lesions evaluable by Low-Grade Glioma Response Assessment in Neuro-Oncology criteria[20].

Treatment. Surgical stage one involved open biopsy and CSF sampling via lumbar puncture. The procedure was performed via craniotomy that was appropriate for reopening for later definitive resection of the tumor to allow initial generous biopsy or partial resection of the tumor. Four neurosurgeons with neuro-oncology expertise performed all surgeries following consensus with the neurosurgical principal investigator. Tumor samples were chosen by identifying macroscopically abnormal tissue confirmed on intraoperative neuronavigation images. Tumor samples, at least 1 cm^3, were sent for analysis. At the second procedure, tumor tissue adjacent to the initial biopsy was taken.

During the operation, peri-tumoral normal brain is removed as part of the surgical approach to gain access to the tumor and to achieve a generous margin of resection where safe to do so. In standard-of-care procedures, this material is generally discarded but is available for research. Informed consent is routinely obtained from patients for the collection of peri-tumoral brain as part of our institutional ethically approved tissue banking procedures. This tissue is macroscopically and radiologically normal (on neuronavigation imaging) but immediately adjacent to the tumor and thus infiltrated by tumor. For electrophysiological examination, a section of the cortex and white matter is removed without cautery artifact and including all layers of normal anatomy and placed immediately in a cold carbogenated solution containing (in mM): 125 NaCl, 25 $NaHCO_3$, 5 HEPES, 1 $CaCl_2$, 6 $MgCl_2$, 3 KCl, 1.25 NaH_2PO_4 and 10 glucose.

Following recovery from biopsy (7–28 days) and confirmation of histopathology and *IDH1* mutation, patients commenced oral safusidenib, twice daily at 250 mg b.i.d. (21–35 days). One dose reduction and no dose escalations were permitted. Safety was monitored by physical examination, vital signs, weight, performance status, electrocardiograms and laboratory evaluations including glucose monitoring.

After treatment, patients underwent CSF sampling via lumbar puncture and planned tumor resection. The extent of resection and use of surgical adjuncts (intraoperative MRI or awake surgery with cortical mapping) were at the discretion of the treating neurosurgeon in consultation with the neurosurgical principal investigator.

Independent cohort

A comparative cohort of 11 patients with a diagnosis of LGG (Supplementary Table 8) was used to generate reference snRNA-seq, spatial metabolomics and transcriptomics data ($n = 11$). Patients were identified from the Royal Melbourne Hospital Neurosurgery Brain and Spine Tissue Bank.

Surgery-only cohort

A comparative cohort of patients with a diagnosis of LGG (Supplementary Table 7), who had undergone two surgical procedures within 3 months, without intervening treatment was generated to identify the impact of surgery alone. Patients were identified from the Royal Melbourne Hospital Neurosurgery Brain and Spine Tissue Bank.

Research Participant Perception Survey

Participants completed the validated 25-item Research Participant Perception Survey[21,22] Short Form during the study at least 3 months post-resection, to obtain data on demographics, experience with the research process and research staff, overall rating of the experience and questions about various reasons for joining, leaving or staying in the study.

Pharmacokinetics

Blood, CSF and tumor tissue were collected pre- and post-safusidenib for pharmacokinetic analysis. Blood was drawn into an EDTA tube longitudinally at days 8, 15 and 28 (±2 days), immediately before dosing. Whole blood was centrifuged 1,500 × *g* for 10 min at 4 °C, and then the plasma layer was isolated and frozen on dry ice. CSF was centrifuged at 500 × *g* for 10 min at 4 °C, after which the supernatant was snap frozen on dry ice. Tissue was snap frozen on dry ice.

PK analysis was conducted at Frontage Labs. For brain tissue, 3 ml of water was added to obtain a matrix of brain homogenate; then, 30 µl of homogenate was supplemented with internal standard (CANM-2895a, dissolved in DMSO/acetonitrile). For CSF, 30 µl was diluted with 2% Tween 20 and supplemented with internal standard. For plasma, 50 µl was supplemented with internal standard. Acetonitrile (for tissue and CSF) or 1.25% acetic acid in acetonitrile (for plasma) was added as precipitant, and the mixtures were vortexed for 5 min at 1,000 rpm. Samples were centrifuged at 6,000 × *g* for 5 min, then 200 µl of supernatant was combined with 200 µl of water, and the mixtures were vortexed for 5 min at 1,000 rpm, then centrifuged.

Samples (10 µl of CSF and tissue, 5 µl of plasma) were injected onto a liquid chromatography with tandem mass spectrometry (LC–MS/MS) system (Sciex Triple Quad 6500+ with Shimadzu HPLC pump LC-30AD and autosampler SIL-30ACMP), equipped with a Shimadzu, Shim-pack Velox PFPP, 2.1 × 50 mm, 2.7 µm HPLC column. LC–MS/MS transitions for safusidenib and CANM-2895a were 534.9 to 156.1 and 545.0 to 159.1 m/z, respectively. A gradient mobile phase consisted of mixing different proportions of 0.02% acetic acid in water and acetonitrile (0.6 ml min^{-1}). The total run time per sample was 2.5 min (CSF), 1.6 min (tissue) or 2 min (plasma).

Quantitation was accomplished by reference to a calibration curve (CSF and plasma: 1–1,000 ng ml^{-1}; tissue: 5–5,000 ng g^{-1}). Analysis of the lower limit of quantification yielded a percentage relative error within ±20% and percentage coefficient of variation no more than 20%. Analysis of quality control samples had percentage relative error within ±15% and percentage coefficient of variation no more than 15%.

Immunohistochemistry

Immunohistochemistry of IDH1-R132H (Dianova IDA-H09; 1:50 dilution; epitope retrieval: CC1 32 min at 100 °C), KI67 (Dako M7240; 1:100 dilution; epitope retrieval: CC1 32 min at 100 °C), ATRX (Sigma HPA001906; 1:300 dilution; epitope retrieval: citrate buffer, HIER for 32 min at 100 °C), TP53 (Leica Biosystems NCL-L-p53-DO7; 1:50 dilution; epitope retrieval: citrate buffer, HIER for 32 min at 100 °C), GFAP (Cell Signaling Technologies 3670; 1:200 dilution; epitope retrieval: EDTA buffer, HIER for 32 min at 100 °C), CD68 (DAKO PG-M1; 1:200 dilution; epitope retrieval: trypsin buffer, HIER for 32 min at 100 °C). Sections stained with hematoxylin and eosin and immunohistochemistry slides were scanned using the 3D Histech Brightfield (20X) and processed using CaseCentre online software.

Immunofluorescence

Sample preparation. Slides were deparaffinized using xylene, followed by wash steps in a graded ethanol series (100%–30%); then, heat-induced epitope retrieval was performed in tris-EDTA buffer for 32 min at 100 °C. Blocking solution (5% goat serum in 0.1% Tween 20 for cytoplasmic staining) was applied to slides for 1 h at 4 °C. Incubation with CD68 (DAKO PG-M1, 1:200 dilution), GFAP (Cell Signaling Technologies 3670, 1:1,000 dilution), CD31 1:500 (Abcam ab134168), IDH1-R132H (Dianova IDA-H09, 1:100 dilution), MAP2A (Thermo Fisher PA110005, 1:1,000 dilution) and Phalloidin (Thermo Fisher A22287, 1:1,000 dilution) antibodies occurred overnight at 4 °C.

Staining with corresponding secondary antibodies Alexa Fluor 594 anti-rabbit (Thermo Fisher A32740, dilution 1:1,000), Alexa Fluor 647 anti-mouse (Thermo Fisher A32728, dilution 1:1,000), Alexa Fluor 488 anti-chicken (Thermo Fisher A11039, dilution 1:1,000) and Alexa Fluor 488 anti-mouse (Thermo Fisher A11004, dilution 1:1,000) were applied for 1 h at room temperature. Slides were then incubated with DAPI for 10 min at room temperature, mounted with FluoroMount-G solution (Thermo Fisher 00-4958-02) and stored at 4 °C until imaging.

Image acquisition and analysis. Whole slide scanning was conducted at ×20 magnification using the Olympus Slideview VS200 slide scanner. Adjacent sections were registered using wsireg (v0.3.5), with the registration graph set to rigid, affine and lastly similarity transformation. Once whole slide images were registered, regions of interest were cropped.

Radiology analysis

Volumetric analysis. Pre- and post-biopsy, and pre- and post-resection fluid-attenuated inversion recovery (FLAIR) MRI sequences were used for semi-automated segmentation of the tumor. Volumes were calculated by measuring the FLAIR hyperintensities using Brainlab software (Brainlab, iPlanNet v2.3.1.215.1) at each timepoint.

Nucleic acid extraction

Tumor tissue obtained pre- and post-safusidenib was placed in RNAlater stabilization solution (Invitrogen) for at least 24 h, then either stored at −80 °C or kept in a fridge until nucleic acid extraction. Tissue was disrupted and homogenized via either mortar and pestle, liquid nitrogen and a QIAshredder (QIAGEN), or a rotor-stator homogenizer and QIAshredder. DNA and RNA were extracted from homogenized tissue using the AllPrep DNA/RNA mini kit (QIAGEN), following the manufacturer's instructions. Germline DNA was obtained from the buffy coat of blood collected in either an EDTA blood collection tube or cell-free DNA blood collection tube (Streck), using the QIAamp DNA blood mini kit (QIAGEN), following the manufacturer's instructions.

Whole-genome profiling

Library preparation for whole-genome sequencing was conducted using genomic DNA from pre- and post-safusidenib tumor samples, along with matched germline DNA. An input of 200 ng was used with the TruSeq DNA Nano kit (Illumina), which was conducted and sequenced to a depth of 40× for normal and 80× for tumor on an Illumina NovaSeq 6000 at the University of Melbourne Center for Cancer Research (Melbourne, Australia) and aligned using Illumina DRAGEN (v4.2). Detected genomic variants were analyzed and classified by the level of evidence based on clinical significance according to Association for Molecular Pathology, American Society of Clinical Oncology and College of American Pathologists guidelines[61].

Epigenetic analyses

Sample preparation for histone modification analysis by MS. Equal amounts (20 mg) of frozen pre- and post-safusidenib brain tumor biopsies were moved to tissueTUBES (520001, Covaris) and connected with 1 ml miliTUBE (520130, Covaris). Samples were hammered until reaching a powder consistency. Then, the tissueTUBES were flipped upside down to transfer the sample into the miliTUBE. Cooled 500 µl of homogenization buffer (60 mM KCl, 15 mM NaCl, 4 mM $MgCl_2$, 15 mM HEPES, 0.5% Triton X-100, 1 mM dithiothreitol (DTT), Roche Protease mix) was added, and samples were sonicated at 10 °C, 6 min, peak incident power 150 W, 200 cycles per burst, 10% duty factor (E220 focused-ultrasonicator, Covaris). Samples were centrifuged for 30 min at 4 °C, 16,000 *g*. The supernatant was stored at −20 °C, while the pellet was further processed by adding 75 µl of 0.2 M H_2SO_4, and overnight acidic extraction was performed at 4 °C, 1,000 rpm in a table-top thermomixer. Acid-extracted histones were processed according to an SP3 protocol as described previously[62]. However, proprietary steps developed by MoleQlar Analytics GmbH have been added to adjust the protocol for histone-specific aspects. Following 2 h of digestion at 37 °C, samples were acidified by adding 5 µl of 5% trifluoroacetic acid (TFA) and quickly vortexed. Beads were immobilized on a magnetic rack, and peptides were recovered by transferring the supernatant to new tubes. Samples were dried down using a vacuum concentrator and reconstituted by adding 20 µl of 0.1% formic acid (FA) to reach a peptide concentration of approximately 0.2 µg μl^{-1}. MS injection-ready samples were stored at −20 °C.

LC–MS analysis of histone modifications. From each sample, 200 ng of peptides was separated on a C18 column (Aurora Elite TS, 15 cm × 75 µm inner diameter, 1.7 µm, IonOpticks) with a gradient from 5% B to 25% B (solvent A 0.1% FA in water, solvent B 100% acetonitrile (ACN), 0.1% FA) over 49 min at a flow rate of 300 nl min^{-1} (Vanquish Neo UHPLC-Systems, Thermo Fisher) and directly sprayed into an Exploris 240 mass spectrometer (Thermo Fisher Scientific). The mass spectrometer was operated in full-scan mode to identify and quantify specific fragment ions of N-terminal peptides of human histone 3.1 and histone 4 proteins. Survey full-scan MS spectra (from m/z 250 to 1,600) were acquired with a resolution of 60,000 at m/z 400 (automatic gain control target of 3×10^6). Typical mass spectrometric conditions were as follows: spray voltage, 1.9 kV; no sheath and auxiliary gas flow; and heated capillary temperature, 300 °C.

Quantification of histone modifications. Data analysis was performed with Skyline (v23.1.0.455) by using doubly and triply charged peptide masses for extracted ion chromatograms. Peaks were selected manually. Heavy arginine-labeled spiketides (13C6; 15N4) were used to confirm the correct retention times and for signal normalization purposes, because all heavy standards were incorporated across all samples at the same concentration. Integrated peak values (total area MS1) were used for further calculations. Endogenous post-translational modification signals were normalized according to the variation of the signal of the spiked-in heavy standards and using median normalization. The percentage of each modification within the same peptide is derived from the ratio of this structural modified peptide to the sum of all isotopically similar peptides. Therefore, the total area MS1 value was used to calculate the relative abundance of an observed modified peptide as percentage of the overall peptide. The unmodified peptide of histone 3.1 (amino acids 41–49) was used as indicator for total histone 3.1. Coeluting isobaric modifications were quantified using three unique MS2 fragment ions. Averaged integrals of these ions were used to calculate their respective contribution to the isobaric MS1 peak (for example, H3K36me3 and H3K27me2K36me1).

Visualization. To inspect each individual histone monomethylation mark, we created a heatmap depicting the $\log_2$(FC) of the relative abundance (median-normalized) between the pre- and post-safusidenib samples. In addition, we created box plots to visualize the relative abundance of histone marks per participant to compare the pre- and post-safusidenib conditions. Paired *t*-test and Wilcoxon test on the post-translational modification relative abundance and Benjamini–Hochberg (multiple-testing procedure using the median-normalized data) were applied for statistical testing.

Single-nuclei RNA expression profiling

Experimental procedure. Pre- and post-safusidenib tissue was frozen on dry ice and stored at −80 °C until nuclei isolation. All steps involved in isolation of nuclei were conducted using pre-chilled buffers and a centrifuge pre-set to 4 °C. Tissue was transferred to a Dounce homogenizer containing homogenization buffer (250 mM sucrose, 25 mM KCl, 5 mM $MgCl_2$, 10 mM Tris pH 8.0, 1 mM DTT, 0.2 U μl^{-1} RNasin ribonuclease inhibitor and 0.1% Triton X-100) and incubated for 1 min before homogenization. Tissue was homogenized using a combination of loose and/or tight pestles and a 1-ml pipette tip, depending on the individual piece of tissue. The homogenates were filtered through a 30-µm strainer and centrifuged at 500 × *g* for 5 min. Supernatant was discarded and the pellet was resuspended in wash and resuspension buffer (Dulbecco's phosphate-buffered saline (PBS) containing 1% bovine serum albumin, 1 mM DTT and 0.2 U μl^{-1} RNasin ribonuclease inhibitor). A further 1 or 2 washes were conducted, depending on pellet size. Nuclei were counted using trypan blue and a hemocytometer. For snRNA-seq of fresh nuclei, 10,000 nuclei per sample were targeted on the Chromium controller, after which library preparation was conducted using the Chromium Next GEM single cell 5′ v2 (dual index) kit (10x Genomics), following the manufacturer's instructions. For snRNA-seq of fixed nuclei (independent LGG cohort), nuclei were fixed for ~20 h using the Chromium Next GEM single cell fixed RNA sample preparation kit (10x Genomics), according to the manufacturer's instructions. A total of 10,000 nuclei per sample were targeted on the Chromium controller, after which library preparation was conducted using the human transcriptome Chromium Fixed RNA kit (4 reactions × 4 barcodes), according to the manufacturer's instructions (10x Genomics), with probe hybridization conducted for ~19 h. Libraries were sequenced on either a NextSeq 2000 or a NovaSeq X (Illumina), targeting 20,000 reads per nucleus. For the clinical cohort, we found on average 30,558 reads per nucleus. For the independent LGG cohort, we found an average of 44,932 reads per nucleus.

All figures were created using ggplot2 (v3.5.1), and all computational analysis methods were run using default parameters unless otherwise specified.

Preprocessing. Data were first processed using Cell Ranger (10x Genomics, v7.1.0) to align FASTQ format files to the hg38 reference genome and perform unique molecular identifier counting. CellBender (v0.3.0) was applied to each sample to estimate and remove ambient RNA. Filtered CellBender output files were further processed with R (v 4.4). To identify and remove doublets, we used Scrublet (v0.2.3), setting an estimated threshold based on the multiplet rate, with an upper limit cutoff of 0.25. We calculated mitochondrial expression percentage for nuclei using scater (v1.28.0) and identified outlier nuclei using the median absolute deviation (MAD) approach to dynamically set thresholds for minimum unique molecular identifier counts and minimum detected genes. We filtered nuclei using the computed thresholds and removed those with a mitochondrial expression percentage >10% (Supplementary Table 4). Overall, 158,487 nuclei passed quality controls, with on average 2,416 genes detected per nucleus. We then applied a log-normalization to the raw gene expression matrix using scater in combination with SingleCellExperiment (v1.22.0). We modeled the gene variance with scran (v1.33.1) to identify the top 5,000 highly variable genes. We thoroughly investigated potential confounders influencing overall gene expression using multidimensional scaling plots. Investigated confounders included age, sex, *IDH* mutation, diagnosis, timing from last dose to sampling, tumor location, and pre-biopsy, post-biopsy or change in tumor volume. None of the investigated confounders appeared to result in clustering.

Sample integration. We merged all filtered datasets and performed an additional sample-wide filtration step once again implementing the MAD approach to set a general threshold for minimum counts. We further filtered low-quality nuclei with total detected counts less than 1,000. The combined dataset contained 178,567 nuclei following quality filtration.

For data integration across samples, we used a variational autoencoder from the scVI (ref. 63) toolkit (v1.1.5). Briefly, the scVI model creates a low-dimensional shared latent space representation of nuclei. We used default parameters to generate the latent space representation with the X_scVI latent space representation used for processing. We next generated a uniform manifold approximation and projection (UMAP) embedding based on the scVI reduced dimensions with spread set to 3 and mindist set to 0.1 with 15 nearest neighbors (n_neighbors). Note that the low-dimensional shared latent space representation of nuclei was used only for cell type annotation and not differential gene expression analysis.

Cell type annotation. Nuclei were clustered based on the scVI reduced dimensions via Leiden clustering using default parameters implemented in bluster (v1.10.0). Clustering of the entire dataset produced 36 cell clusters. Nuclei were automatically annotated using SingleR (v2.2.0) using references including a downsampled glioblastoma (GBM) harmonized dataset[64], a GBM tumor dataset modeling a normal neurodevelopmental hierarchy[30] and a dataset capturing a normal human prefrontal cortex from gestation through to adulthood[65].

Clusters were first manually annotated according to the predicted cell type labels from SingleR and marker gene expression. Normal cell types identified included vasculature, immune, neuron, oligodendrocyte, astrocyte and OPC, and tumor cell types included AC-like, OPC-like and progenitor (vasculature: *IGFBP7*, *COL4A2*; immune: *PTPRC*, *CD68*; neuron: *C1QL3*, *NPTXR*; oligodendrocyte: *MBP*, *ERMN*; astrocyte: *NTRK2*, *MGST1*; OPC: *CNP*, *CSPG4*; AC-like: *AQP4*, APOE; OPC-like: *APOD*, *OLIG1/2*; progenitor: *TOP2A*). Nuclei in the immune and neuron compartment were reclustered following the process outlined above. Clusters for both immune cells were annotated according to the predicted labels and known marker genes. From the immune compartment, myeloid cell types including macrophages were identified, and a lymphoid compartment comprised of T cells. Microglia were also identified (macrophage: *CD163*, *CD6*; T cell: *CD4*, *CD8A*, *FOXP3*; microglia: *P2RY12*, *CX3CR1*).

The independent cohort of 11 LGG samples were preprocessed, integrated and annotated following the same specifications as the pre- and post-safusidenib samples—with MAD filtering used as the final quality control step, additionally retaining nuclei with fewer than 1,000 nuclei. This resulted in 75,963 nuclei across 77 clusters that were similarly clustered and annotated in smaller subsets after initial manual annotations. A poor-quality population was identified featuring higher levels of mitochondrial reads and was removed from further analyses.

CNV analysis. To assess somatic copy number variations (CNV) in each sample individually, we implemented Numbat[66] (v1.4.0). Briefly, the algorithm processes aligned sequencing reads to detect CNVs by normalizing read depth and segmenting the genome to identify deviations from expected copy numbers. CNV analysis was implemented to discern malignant (presence of aberrant CNVs) from nonmalignant nuclei, helping to validate assigned cell type annotations.

We identified an ambiguous population ($n = 10,691$ nuclei) with a high number of detected genes and no detected CNVs by Numbat. We therefore excluded this population from subsequent analysis. Consistent with our findings from other technologies, participant A-04 was detected as having low tumor purity in both pre- and post-safusidenib samples and was therefore also excluded. In total, we were left with 158,487 nuclei in our combined and processed dataset.

Cell cycle analysis. We used the CellCycleScoring function from Seurat (v5.1.0) to assign G1, G2M and S phase cell cycle scores to cells, using the G2M and S gene sets.

Differentiation potential analysis. We used CytoTRACE2 (v1.0.0)[67] to infer the differentiation potential of malignant nuclei. CytoTRACE2 is an interpretable deep learning framework for characterizing potency and delineating single-cell differentiation landscape. We implemented a pairwise *t*-test to evaluate the significance in differentiation potency scores between tumor populations from the pre- and post-safusidenib conditions.

Furthermore, two-dimensional meta-module butterfly plots were constructed for the progenitor tumor populations from pre- and post-safusidenib samples. Tumor gene sets used to construct the meta-module plots were collected from Neftel et al.[43]. Shannon $\log_2$ entropy scores were calculated from meta-module assignment proportions of progenitor cells using entropy (v1.3.1). We used permutation testing (1,000 permutations) to assess the difference in heterogeneity in the progenitor cell population between treatment conditions.

Correlation plots. We performed a correlation test to investigate the association between IFN and AC-like programs in the AC-like tumor population. The analysis used the differences in average log expression for each gene module between pre- and post-safusidenib samples across participants, derived from snRNA-seq data. The AC-like and IFN gene programs were curated as described ('Gene set acquisition'). Significance was assessed by linear regression performed using stats (v4.4.1). We similarly performed correlation tests between the IFN program and STING/HIF1-α program, as well as IFN and change in immune cell proportion between pre- and post-safusidenib samples.

Ternary plots. We evaluated the metabolic preferences of cell-state populations for glycolysis, Krebs cycle and lactate metabolic modules using ternary plots. The three metabolic gene sets were obtained as described ('Gene set acquisition'). For each nucleus in the AC-like and OPC-like tumor populations across an independent cohort of 11 LGG samples, we calculated the average log expression for each module. The scores for the three modules were normalized to sum to 1 for each nucleus. These normalized scores were then visualized in ternary plots, colored by cell type, using ggtern (v3.5.0).

We also created a box plot to visualize the average log expression of the glycolysis gene module across donors from the independent LGG cohort for each cell type. To assess the enrichment of the average log expression of the glycolysis module across donors, we applied a Welch *t*-test, comparing AC-like and astrocyte cell types individually against all other populations, excluding the respective cell type under analysis. We next evaluated the enrichment of the Krebs cycle and lactate metabolism modules in OPC-like tumor cells compared with AC-like tumor cells using a pairwise *t*-test. *P* values were adjusted by Benjamini–Hochberg to correct for multiple testing.

Differentially expressed gene analysis. Differentially expressed gene (DEG) analysis was conducted for each cell population separately using limma (v3.61.9) and edgeR (v4.3.11). Before the analysis, genes expressed in less than 1% of nuclei were excluded to reduce noise in the data. Counts and metadata were then aggregated to create pseudobulk profiles, allowing for comparison between pre- and post-safusidenib samples. To ensure statistical robustness, only aggregated profiles with at least 10 nuclei were retained. We performed DEG analysis using 'pseudoBulkDGE' to model the effect of the treatment condition on gene expression while accounting for participant variability. The design matrix included terms for sample treatment status (pre- and post-safusidenib) and participant as covariates, with the coefficient of interest being the differential expression associated with the treatment status. Significance was determined by a false discovery rate threshold of <0.05. In addition, we conducted DEG analysis on the tumor compartment, comprising malignant cell types: AC-like, OPC-like and progenitor. Furthermore, RRHO2 (v1.0) plots were used to assess sensitivity when individual patients were dropped from the analysis. This confirmed broad concordance of results for all patients.

Gene set acquisition. We curated gene sets associated with malignant cellular states based on extensive review of previously published studies. The malignant gene sets that reflect glioma cellular developmental hierarchy include AC-like, OPC-like, NPC-like and MES-like programs[30,65]. In parallel, we compiled gene sets from various sources reflecting development in the normal brain, labeled here as astrocyte, OPC, oligodendrocyte, and the G1/S and G2/M programs[64].

GSEA. We initially conducted GSEA from ranked lists generated using results from DEG analysis. For each cell type annotation, we created a ranked list of genes using $-\log_{10}$(*P* value) while accounting for the direction of log(FC). GSEA was then performed using fgsea (v1.30.0), including a total of 10,520 gene sets in the analysis: 10,461 Gene Ontology gene sets and 50 hallmark gene sets obtained from mSigDB (v10.0.2), as well as 4 malignant and 5 nonmalignant gene sets ('Gene set acquisition'). In addition, we performed GSEA on the tumor compartment with genes once again ranked using DEG results.

For each cell type population separately, as well as the tumor compartment together, we generated a volcano plot based on the GSEA results. In these plots, the *x*-axis represents the normalized enrichment score, while the *y*-axis represents the $-\log_{10}$(adjusted *P* value).

Significantly enriched gene sets were grouped into semantic terms based on biological relevance in an unsupervised manner. We summarized this information as a dot plot depicting the proportion of significant gene sets for each semantic term per cell type population and colored by enrichment direction.

For each tumor cell population, we also annotated the ranked gene lists based on their inclusion in the malignant AC-like, OPC-like, NPC-like and MES-like gene sets. We then calculated the proportion of genes in each ranked list that were associated with a specific glioma state, using overlapping windows of 30 genes and moving in 0.10 increments along the spectrum of $-\log_{10}$(*P* value) in the direction of log(FC).

We also conducted GSEA following the methodology described by Spitzer et al.[29]. Briefly, for each cell type annotation, we created bulk gene expression profiles using log(counts) for pre- and post-safusidenib samples for each participant individually. We then calculated the average expression of each gene across these bulk profiles for both pre- and post-safusidenib conditions. To prepare for GSEA, we generated a ranked list of genes by $\log_{10}$(ratio), calculated by subtracting the average expression of pre-safusidenib samples from that of post-safusidenib samples. We then proceeded with GSEA as previously described using fgsea. GSEA was also performed in this way on the tumor compartment by generating a bulk expression profile for malignant cell types: AC-like, OPC-like and progenitor combined.

Spitzer comparison. We next endeavored to compare these GSEA results to those published by Spitzer et al.[29]. We performed a rank–rank hypergeometric overlap test to assess the concordance of the ranked lists accounting for all cell types between the two studies with RRHO2 (ref. 68).

To compare cell type annotations, we performed an automatic annotation of our single-cell dataset with SingleR using the matched oligodendroglioma dataset from Spitzer et al.[29]. We also used a Jaccard index to quantify the degree of similarity in this comparison.

We next compared the progenitor compartments of matched pre- and post-mIDH inhibitor samples from a responder (oligodendroglioma) and a nonresponder (astrocytoma) ($n = 1$ each)[29]. We first calculated the log(FC) for each gene between pre- and post-mIDH inhibitor samples for both patients. A ranked gene list was then generated by subtracting the log(FC) values of the nonresponder from those of the responder. Finally, we assessed the proportion of genes in the ranked list that were associated with a specific glioma state, as previously described ('GSEA').

We also generated ternary plots for progenitor cells from the responder and nonresponder samples, using a similar approach as previously described ('Ternary plots'), and colored them by treatment exposure status. In addition, we plotted the overall mean scores for each condition and patient across the metabolic programs.

Metabolomics

Sample preparation. Whole blood in a heparin collection tube was centrifuged 1,500 × *g* for 15 min at 4 °C, and then the plasma layer was isolated and snap frozen in dry ice. CSF was centrifuged at 500 × *g* for 10 min at 4 °C, after which the supernatant was snap frozen on dry ice. Tissue for bulk metabolomics was frozen in liquid nitrogen. For spatial metabolomics, tissue was flash frozen in an isopentane bath in liquid nitrogen, then stored at −80 °C until cryosectioning. An additional untreated sample was processed to the same specifications.

Bulk LC–MS. Tissue samples of 20 mg each were extracted for LC–MS analysis by homogenization in a Precellys 24 Tissue homogenizer coupled to a Cryolys cooling system (Bertin Technologies) in 500 µl of 3:1 methanol–Milli-Q water (containing internal standards). Extracts were vortexed and mixed on a thermomixer (10 min) to ensure complete metabolite extraction and then centrifuged at 4 °C for 10 min at 18,213 × *g* to remove the tissue pellet.

Analyses of polar analytes in the samples were performed on the Orbitrap ID-X Tribrid mass spectrometer (Thermo Scientific) coupled to a Vanquish Horizon UHPLC system (Thermo Scientific). Separation of polar metabolites was performed on a Merck SeQuant ZIC-pHILIC column (150 mm × 4.6 mm, 5 µm particle size) maintained at 25 °C, using a binary gradient consisting of solvent A: 20 mM ammonium carbonate (pH 9.0; Sigma-Aldrich) and solvent B: 100% ACN. The gradient run was as follows: time (t) = 0.0 min, 80% B; t = 0.5 min, 80% B; t = 15.5 min, 50% B; t = 17.5 min, 30% B; t = 18.5 min, 5% B; t = 21.0 min, 5% B; and t = 23–33 min, 80% B, at a solvent flow rate of 300 µl min^{-1}.

Bulk GC–MS. For GC–MS polar analysis, aliquots of 2 × 50 µl tissue lysates and pooled biological quality control were transferred into glass inserts and dried completely in a rotational vacuum concentrator (RVC 2–33, CDplus) at 20 °C, with a further 50 µl of methanol wash to ensure complete removal of residual water. This was followed by a two-step online derivatization process for the methoximation (with 25 µl of methoxylamine hydrochloride (30 mg ml^{-1} in pyridine, Sigma) for 2 h at 37 °C) and trimethylsilylation (25 µl of *N*,*O*-bis(trimethylsilyl) trifluoroacetamide containing trimethylchlorosilane (BSTFA + 1% TMCS) for 1 h at 37 °C with continuous mixing) of the polar metabolites with an autosampler robot (PAL RTC). The derivatized samples equilibrated for 1 h at room temperature before 1 µl was injected (1:10 split ratio) onto the gas chromatography–triple quadrupole–mass spectrometer (GC–QqQ–MS).

Polar metabolite analysis was performed using a GC-TQ8050NX (Shimadzu) equipped with a DB-5 capillary column (30 m × 0.25 mm, 1 µm film thickness; Agilent Technologies). The inlet temperature was kept at 280 °C and helium was used as a carrier gas (column flow = 1 ml min^{-1}). The GC oven temperature was ramped from 100 °C and held for 4 min, to 320 °C at 10 °C min^{-1}, and then held for 11 min at 320 °C. The transfer line and ion source temperatures were 280 °C and 200 °C, respectively. Argon was used as the collision-induced dissociation gas.

Shimadzu GCMSsolution Realtime Analysis (v5.34) enabled target metabolite detection through the utilization of the Shimadzu Smart Metabolites Database (v3) containing up to 629 targets with multiple reaction monitoring transitions including precursor ion, product ion, collision energy, retention index and time, with a minimal dwell time of 2 ms setup for the acquisition method. Data analysis was undertaken in Shimadzu LabSolutions InSight software (v3.6) by peak area integration and alignment to the quantifier and qualifier multiple reaction monitoring in the metabolite database.

Quantification of 2-HG. For the quantification of 2-HG, a standard plot of the isotopically labeled metabolite (^{13}C-2-HG) was run in the biological matrix to determine the physiological range. Once the physiological range was determined, the ^{13}C-2-HG was added into the extraction solvent and all study samples were spiked with 0.5 µM of the ^{13}C-2-HG.

For the LC–MS, targeted peak picking of both the isotopically labeled metabolite and endogenous metabolite areas were obtained using TraceFinder Software (v4.1, Thermo Scientific). Peak areas were measured using the ICIS detection algorithm with default settings and smoothing set to 9. The endogenous concentration of the metabolite was determined by calculating the ratio of ^{12}C to ^{13}C and multiplied by the spiked concentration of the isotopically labeled metabolite (^{12}C area /^{13}C area × 0.5 µM).

For the GC–MS, the ^{12}C and ^{13}C metabolite areas were obtained using Shimadzu LabSolutions InSight software. The endogenous concentration of the metabolite was determined as described above. The linear dynamic range of 2-HG in tissue on the GC–MS was lower than that of the LC–MS, with a decreased response factor observed above 30 µM. This was probably confounded by the rich biological matrix compromising the derivatization efficiency.

Statistical analysis of LC and GC metabolomics data. Data analysis was undertaken in El Maven software (v0.12.1). Level 1 metabolite identification, according to the Metabolite Standard Initiative, was based on matching accurate mass and retention time to the 550 authentic standards in the Metabolomics Australia in-house library. Batch effects were removed using the function limma::removeBatchEffect.

We thoroughly investigated potential cofounders influencing metabolite abundance using multidimensional scaling plots. Investigated confounders included age, sex, IDH mutation, diagnosis, timing from last dose to sampling, tumor location, and pre-biopsy, post-biopsy or change in tumor volume. None of the investigated confounders appeared to result in clustering.

For the differential analysis of metabolites in bulk LC– and GC–MS data, we used the scale function from the R base package to normalize the raw abundance counts for each metabolite on a row-wise basis. Subsequently, a paired t-test was performed to assess the significance of differentially expressed metabolites between the pre- and post-safusidenib samples. To evaluate the log(FC) of metabolites, we computed the logarithm of the ratio of the average normalized abundance in the post-safusidenib samples relative to the pre-safusidenib samples. P values were adjusted by Benjamini–Hochberg to account for multiple testing and the significance threshold was set at 0.1.

We generated an expression rank list based on the log(FC) of each individual metabolite. The pathway database was constructed using the Relational Database of Metabolomics Pathways (RaMP-DB, v2.0) to access metabolic elements within nominated pathways[69]. For each pathway, the enrichment score was calculated using the fgsea::fgsea function, with 2,000 permutations performed to obtain the empirical P value.

Spatial metabolomics. Frozen tissue was sectioned at a thickness of 10 µm directly onto indium tin oxide-coated glass slides (surface resistance of 70–100 Ω). Frozen sections were dried in a freeze dryer (MODULYOD, Thermo Electron Corporation) for 30 min, followed by collection of optical images using the light microscope embedded in the MALDI-TOF MSI instrument (iMScope QT) before matrix application.

Matrix deposition with α-cyano-4-hydroxycinnamic acid (CHCA, P# C2020, Sigma-Aldrich) was performed using iMLayer AERO (Shimadzu) for matrix spraying to recrystallize and obtain fine matrix crystals, which enable high sensitivity and high spatial resolution (0.7 µm at 250 °C). For CHCA matrix spraying, 8 layers of 10 mg ml^{-1} CHCA in acetonitrile/water (50:50, v/v) with 0.1% trifluoroacetic acid solution were used. The stage was kept at 70 mm s^{-1} with 1 s of dry time at a 5-cm nozzle distance and pumping pressure kept constant at 0.1 MPa and 0.2 MPa, respectively.

All MSI experiments were performed using an iMScope QT instrument (Shimadzu). The instrument is equipped with a laser-diode-excited Nd:YAG laser and an atmospheric pressure MALDI. Data were acquired using a laser intensity at 60 for 10 µm spatial resolution, detector voltage was set at 2.36 kV, laser repetition frequency was set at 2,000 Hz, desolvation line temperature was maintained at 250 °C and a laser irradiation count of 50 shots were accumulated per pixel.

Data were imported into R and analyzed with Cardinal (v2.6.5), including normalization via total ion current, spectrum smoothing, baseline correction, peak picking, alignment and filtering. Note that peaks that were also found in matrix-only sample preparations (no tissue) on a minimum detection frequency in at least 5% of the pixels were also removed. Next, the processed spectrum was subjected to binning to obtain the final spectrum information. Peaks were matched against the Human Metabolome Database (v5.0)[70] by using the k-nearest neighbor methodology. For each peak, a set of 30 nearest neighbors from the generated Human Metabolome Database peak list, for which the mass is less than 50 ppm distant, is identified.

For effective visualization of the intensity of any peak, we used Gaussian kernel density estimation. The computation of the kernel density estimation was done using the stats::density function.

Alignment of spatial metabolomics and transcriptomics. Serial sections of untreated sample A–E (Supplementary Table 7), featuring spatial metabolomics (MALDI-TOF) and transcriptomics (Xenium), respectively, were aligned according to the principles established in Kriel et al.[71,72] Briefly, the python (v3.11) package STalign (v.1.0.1)[73] received numpy arrays of cell centroid coordinates as source and metabolite coordinates as target datasets. A pre-alignment script aligned datasets to a similar angle, before cell centroid positions were rasterized and landmarks for registration were manually determined. Cell centroid coordinates then underwent large deformation diffeomorphic metric mapping using the function Stalign. Large deformation diffeomorphic metric mapping was performed before the mapping was applied to the metabolite coordinates. Metabolite expression was aligned to individual cells by calculating the average expression of each metabolite across grid points within 20 µm of each cell.

Association of cell state and metabolite profile. To reliably capture cell states and metabolite profiles within the tumor core region, we histologically differentiated tumor core and leading edge. The tumor core region was divided into nonoverlapping 100 × 100 µm^2 grids. The ratio of AC-like to OPC-like populations was calculated for each grid. Only grids where AC-like and OPC-like cells together comprised over 50% of the total population were included in further analysis. Average metabolite abundance was determined for each of the grids using the alignment. Next, we fitted a linear regression of the metabolite abundance versus the ratio, allowing determination of significant association via a *t*-test of the coefficient.

DNA methylation profiling

Experimental procedure. The Infinium MethylationEPIC v2.0 BeadChip assay (Illumina) was conducted using genomic DNA obtained from all 10 matched pre- and post-safusidenib tumor samples, which was conducted at the Australian Genome Research Facility.

Preprocessing. Raw DNA methylation profiling data were retrieved and preprocessed using functionalities available from minfi (v1.50.0). All samples showed a mean detection *P* value of probes below 0.05, ensuring their inclusion in the analysis. We performed functional normalization and filtered out any failed probes in one or more samples based on detection *P* values. Probes located on sex chromosomes, within 10 base pairs of common single-nucleotide polymorphisms, or identified as potentially cross-reactive were also removed. A total of 813,133 CpG sites passed quality control.

Global methylation. We calculated beta density values to characterize CpG site intensities for each sample. To evaluate significant changes in global methylation, we used a one-sided Kolmogorov–Smirnov test.

Spatial transcriptomics

10x Xenium spatial transcriptomics was performed at single-cell resolution on three matched pre- and post-safusidenib samples. An additional untreated sample with aligned spatial metabolomics was also processed according to the same procedure. Data were preprocessed, including nuclei segmentation and normalization, and filtered to retain only nuclei with robust data. Nuclei were annotated using a hierarchical strategy combining manual and automated annotation.

Gene panel design. The Xenium In Situ technology uses targeted panels to detect gene expression. A total of 339 genes for cell type identification were selected (Supplementary Table 6). Probes contain two complementary sequences that hybridize to the target RNA and a third region encoding a gene-specific barcode. This design ensures high specificity by preventing off-target signals. Upon probe binding to the target RNA, the paired ends ligate to generate a circular DNA probe.

Experimental procedure. We first sectioned a 10-µm formalin-fixed paraffin-embedded tissue section onto a Xenium slide (12 × 24 mm), followed by deparaffinization and permeabilization to make the mRNA accessible. Probe hybridization of genes and two negative control genes occurred at 50 °C overnight with a probe concentration of 10 nM. This was followed by stringency washing to remove unhybridized probes and another round of probe ligation and annealing of rolling circle amplification primer at 37 °C for 2 h. The resulting circularized probes were then enzymatically amplified for 1 h at 4 °C followed by 2 h at 37 °C. After washing, background fluorescence was quenched chemically.

Sections were then imaged using the fully automated Xenium Analyzer instrument. On the Xenium Analyzer, image acquisition is performed in 15 cycles that include reagent cycling, incubation, fluorescent probe hybridization, imaging and probe removal. In each cycle, fluorescent-labeled oligonucleotides are bound to amplified barcodes and the fluorescent intensity in each of the four Xenium color channels is measured, which is used to identify a target gene. Only transcripts that had a quality value >20 were kept. *z*-stacks were taken with a 0.75-µm step size across the entire tissue thickness, which are stitched back together to make a spatial map of the transcripts across the tissue.

Nuclei segmentation. To assign mRNAs to nuclei, and thus enable downstream analysis, DAPI images were used to detect nuclei using a 10x Genomics-supplied neural network algorithm. Purely for visualization purposes, cell segmentation supplied by Xenium Analyzer (v3) is used.

Post-staining. For post-staining Xenium slides, no additional fixation or permeabilization was required. Slides were incubated with blocking buffer (0.1% Tween 20 in 1× PBS with 5% goat serum) for 1 h at 4 °C. After the slides were washed three times with PBS-T, a 1:1,000 dilution of GFAP primary antibody (Thermo Fisher Scientific, PA1-10004) and 1:500 dilution of Alexa Fluor 647 phalloidin (Thermo Fisher

Scientific, A22287) were applied and incubated overnight at 4 °C. The slides were then washed three times with cold PBS-T before the secondary antibodies were added. Staining with Alexa Fluor 488 anti-chicken (Thermo Fisher, A11039; dilution 1:1,000) was applied for 1 h at room temperature. Slides were then incubated with DAPI for 10 min at room temperature and mounted with FluoroMount solution. Slides were stored at 4 °C until imaging.

Image acquisition. After stage calibration, a low-resolution tilescan (256 × 256 pixels) of the entire sample area was taken at ×10 magnification with regions of interest drawn accordingly for each section on the sample area. To ensure that all tiles were captured at adequate focus, 10–20 support points were added to each section depending on their size. After the support points were added, the objective was switched to a ×25 oil immersion lens and the appropriate strength of 405, 488 and 647 laser lines was determined. Thereafter, the *z*-position of each support point was calibrated manually. Final tile scans were acquired at a tile size of 3,852 × 3,852 pixels with a scan speed of 6 at a bidirectional direction, with small *z*-stacks of 5 or 6 slices per tile. Orthogonal projections and stitching of tile scans were completed using ZEN Blue software (v3.8).

Preprocessing. We next generated a single-cell expression matrix by counting molecules of each gene within the nucleus-bound area assigned to a cell by the segmentation algorithm (distance to nucleus equal to zero). We removed any cells with fewer than 20 total transcripts within the nucleus (Supplementary Table 4). We then applied log-normalization to the raw gene expression matrix using scater in combination with SingleCellExperiment.

Cell type annotation. Data dimensions were reduced using principal component analysis (PCA) and the number of components kept was determined via a global maximum likelihood based on a translated Poisson mixture model approach with 20 nearest neighbors implemented in intrinsicDimension (v1.2.0). This approach has been shown to be particularly sensitive to separation of challenging subpopulations[74]. We also generated a UMAP embedding based on the PCA with spread set to 1 and mindist set to 0.1 with 15 nearest neighbors (n_neighbors). Cells were then clustered based on the PCA via Leiden clustering implemented in bluster. Cells from each sample were automatically annotated separately using SingleR using references including a downsampled GBM harmonized dataset, a GBM tumor dataset modeling a normal neurodevelopmental hierarchy and a dataset capturing a normal human prefrontal cortex from gestation through to adulthood. Cluster annotation then proceeded as described earlier for snRNA-seq data with the addition of identification of an NPC-like tumor population and neutrophil immune population (NPC-like: *HES6*, *SOX11*; neutrophil: *ITGAX*, *SLC11A1*).

Co-localization analysis. To assess inflammatory response in tumor cells co-localized to immune cells in our Xenium samples, we used functionalities available from sf (v1.0-17). We first created a spatial point geometry object using sf_point from integrated spatial transcriptomics and snRNA-seq data inferred using CytoSPACE[36] ('Multi-omics integration'). We next generated a 30-µm buffer around each immune cell with st_buffer and subsequently classified any tumor cells located within any immune cell buffer as co-localized. Welch's *t*-test was used to compare the average log expression of the inflammatory response module between tumor cells that were co-localized with immune cells and those that were not.

To quantify the co-localization of immune cell types (T cells and macrophages) to vasculature in our Xenium samples, we used the Kontextual framework provided by Statial (v1.7.0)[75]. Briefly, Kontextual is a method that characterizes the localization relationship between cell types spatially. The program contextualizes these relationships relative to the spatial behavior of a third parent cell population, building on the L-function. We used kontextCurve to estimate localization relationships from each immune cell type of interest to the vasculature with the parent population as all immune cells. Kontextual was evaluated over radii of 10 µm to 250 µm, at intervals of 20 µm (rs) and inhom set to true. To create plots, kontextPlot was used.

Transcript niches. To identify transcript-based niches, we adapted the deep learning framework by Vannan et al.[76], which uses GraphSAGE (v1)[77], a 2-hop graph neural network. Briefly, to infer structures in the data, transcript-based niches were identified using all detected nuclei transcripts as nodes, ignoring cell segmentation, and edges between nodes drawn based on Euclidean distances. Before building sample graphs, we removed poor-quality transcripts (qv < 20) and retained only nuclei-bound transcripts (nuclei distance < 0). For each sample, a graph was constructed and then subsampled to reduce memory usage. All subgraphs were aggregated into a single joined graph for model training (4,586,495 nodes, 113,592,432 edges). Other parameters used for graph construction and training remained as previously reported[76]. We trained the model on the merged graph with 10 epochs and achieved a training accuracy of 0.82.

We extracted the embedding representation for all transcript nodes across nine samples using the trained model. All sample nodes were then clustered (102,129,436 total nodes) using GaussianMixtureModel ($k = 8$) from the PyCave (v3.2.1) library (https://github.com/borchero/pycave).

For each sample, transcripts were consolidated into hexbin plots using hexbin (v1.28.3) and visualized with ggplot2. A consistent bin width of 70 was used to ensure uniform bin sizes across samples. Each bin was distinctly labeled and color coded based on the predominant node label among the contained transcripts. Bins with fewer than 10 transcripts were excluded from the analysis. Cell assignment to transcript-based niches was determined by calculating the Euclidean distance from each cell centroid to the nearest hexbin centroid. We computed the cell type enrichment scores for each transcript-based niche across samples using a simple chi-square test approach. We also calculated the proportion of cells assigned to each transcript niche, both normalized across niches and cell types.

For each participant, we systematically summarized the expression of critical synaptic signaling genes across transcript-based niches for both pre-safusidenib and post-safusidenib samples. We normalized these computed proportions and excluded combinations that included fewer than 20 bins to maintain robust data integrity.

Multi-omics integration. For each sample, we integrated spatial transcriptomics data with its corresponding snRNA-seq data using CytoSPACE[36] (v1.1.0). Briefly, CytoSPACE uses a shortest augmenting path optimization algorithm to align single-cell transcriptomes with in situ spatial transcriptomics data. As a result, it provides globally optimal cell-to-centroid assignments along with an inferred gene expression matrix. The raw gene expression matrix output from CytoSPACE was log-normalized using the scater package. This integration enabled us to visualize gene modules that were previously inaccessible with the limited gene panel available in our Xenium dataset. To create summary plots of the inferred gene module expression, we used the hexbin assignments of cells (Transcript niches). We first calculated the average expression of the target gene set in each cell using the CytoSPACE-inferred matrix, then aggregated cells within their respective hex bins to compute the average expression per bin. For the analysis specific to the T7 niche, we used the same methodology, selectively focusing on this niche alone.

Whole-cell patch-clamp recordings

Slice preparation. All procedures were performed with the approval of the Royal Melbourne Hospital HREC (HREC numbers 2001:85 and

2020:214). After the resection (on average <4 h after surgery), tissue was placed immediately in a carbogenated solution containing (in mM) 125 NaCl, 25 $NaHCO_3$, 5 HEPES, 1 $CaCl_2$, 6 $MgCl_2$, 3 KCl, 1.25 NaH_2PO_4 and 10 glucose. Samples were rapidly transported on ice to the laboratory (less than 10 min) where they were immediately sectioned into 300-µm-thick slices using a vibrating tissue slicer (Leica Microsystems) in ice-cold carbogenated solution containing (in mM) 110 choline chloride, 26 $NaHCO_3$, 11.6 Na-ascorbate, 7 $MgCl_2$, 3.1 Na-pyruvate, 2.5 KCl, 1.25 NaH_2PO_4, 0.5 $CaCl_2$ and 10 glucose. Slices were incubated in carbogenated solution containing (in mM): 125 NaCl, 25 $NaHCO_3$, 5 HEPES, 1 $CaCl_2$, 6 $MgCl_2$, 3 KCl, 1.25 NaH_2PO_4 and 10 glucose at 35 °C for 30 min and thereafter at room temperature until required. Recordings were performed in artificial CSF with the following composition (in mM): 125 NaCl, 25 $NaHCO_3$, 3 KCl, 1.2 $CaCl_2$, 0.7 $MgCl_2$, 1.25 mM NaH_2PO_4 and 10 glucose.

Electrophysiology. Whole-cell patch-clamp recordings were performed from pyramidal neuron somas using an Olympus BX51 WI microscope equipped with a fluorescent imaging system. Slices were continuously perfused with carbogenated artificial CSF (2 ml min^{-1}) at physiological temperature (33–36 °C). Borosilicate glass recording pipettes (4–6 MΩ) were filled with intracellular solution of the following composition (in mM): 130 K-gluconate, 10 KCl, 10 HEPES, 4 Mg^{2+}-ATP, 0.3 Na_2-GTP and 10 Na_2-phosphocreatine (pH set to 7.25 with KOH, osmolarity 285 mosmol l^{-1}). The intracellular solution also included 0.02% 5-(and-6)-tetramethylrhodamine biocytin (Thermo Fisher Scientific) for post hoc visualization and cell identity confirmation. Following whole-cell configuration, neuron morphology was confirmed using the QImaging Rega ELECTRO CCD Camera mounted on the Olympus BX51 WI microscope (530 nm LED excitation). Where possible, detailed neuron morphology was also recorded using confocal microscopy (Zeiss 900; 544 nm excitation, 571 nm emission). Voltage recordings were made in current-clamp configuration using a Multiclamp 700B amplifier. Data were filtered at 10 kHz and acquired at 50 kHz using a Digidata 1440A (Axon Instruments) with no junction potential correction. pClamp and Clampfit softwares (Axon Instruments) were used for data acquisition and analysis, respectively. To characterize the excitability of recorded neurons, steps of current (1,200 ms duration) were injected via the recording pipette at increments of 20 pA. Rheobase was measured as the current step, which first evoked action potentials; membrane resistance was measured in response to a small hyperpolarizing current pulse (−10 pA, 1,200 ms); and resting membrane potential was measured upon break-in in the 200 ms before current step injection. Action potential width was measured as full width at half amplitude. Data were analyzed using minitab (v22.1) using a linear mixed model approach.

Statistical analysis

Statistical details are available in the figure legends. *P* values were calculated using GraphPad Prism (v10.0.0) or R (v4.4) and represent the results of Student's *t*-test, one-way ANOVA with multiple comparisons or linear regression test.

Reporting summary

Further information on research design is available in the Nature Portfolio Reporting Summary linked to this article.

Data availability

Study-level clinical and spatial data from this study will be made available upon reasonable request to the corresponding authors, from a qualified medical or scientific professional for the specific purpose laid out in that request, and may include deidentified individual participant data (requests evaluated within 4 weeks). The data for this request will be available after a data access agreement has been signed. Further translational data are available from dbGAP under accession code phs003976 after provision of IRB ethics approval, and the snRNA-seq data for the independent LGG cohort are available on GEO under accession code GSE292732. Data for the matched spatial transcriptomics and metabolomics data from sequential sections of the same LGG tumor are available on BioImage Archive at https://doi.org/10.6019/S-BIAD1426. Publicly available data from Spitzer et al.[29] are available on GEO under accession number GSE26099 under the terms and conditions specified by the data provider. Single-cell sequencing reads were aligned and quantified using the GRCh38 human reference genome (2020-A), a pre-built reference package provided by 10x Genomics (GENCODEv32/Ensembl98). The reference package is available at https://www.10xgenomics.com/support/software/cell-ranger/latest/release-notes/cr-reference-release-notes#2020-a. Whole genome sequencing reads were aligned using the hg38 reference available on DRAGEN Illumina at https://sapac.support.illumina.com/downloads/dragen-reference-genomes-hg38.html. Source data are provided with this paper.

Code availability

All original code is publicly available on GitHub at https://github.com/MontanaSpiteri/AnHeart. Any additional information required to reanalyze the data reported in this paper is available from the corresponding authors upon request.

References

61. Li, M. M. et al. Standards and guidelines for the interpretation and reporting of sequence variants in cancer: a joint consensus recommendation of the association for molecular pathology, American Society of Clinical Oncology, and College of American Pathologists. *J. Mol. Diagn.* **19**, 4–23 (2017).
62. Hughes, C. S. et al. Single-pot, solid-phase-enhanced sample preparation for proteomics experiments. *Nat. Protoc.* **14**, 68–85 (2019).
63. Lopez, R., Regier, J., Cole, M. B., Jordan, M. I. & Yosef, N. Deep generative modeling for single-cell transcriptomics. *Nat. Methods* **15**, 1053–1058 (2018).
64. Ruiz-Moreno, C. et al. Charting the single-cell and spatial landscape of IDH- wild-type glioblastoma with GBmap. *Neuro. Oncol.* noaf113 (2025).
65. Herring, C. A. et al. Human prefrontal cortex gene regulatory dynamics from gestation to adulthood at single-cell resolution. *Cell* **185**, 4428–4447.e28 (2022).
66. Gao, T. et al. Haplotype-aware analysis of somatic copy number variations from single-cell transcriptomes. *Nat. Biotechnol.* **41**, 417–426 (2023).
67. Kang, M. et al. Mapping single-cell developmental potential in health and disease with interpretable deep learning. Preprint at *bioRxiv* https://doi.org/10.1101/2024.03.19.585637 (2024).
68. Cahill, K. M., Huo, Z., Tseng, G. C., Logan, R. W. & Seney, M. L. Improved identification of concordant and discordant gene expression signatures using an updated rank–rank hypergeometric overlap approach. *Sci. Rep.* **8**, 9588 (2018).
69. Braisted, J. et al. RaMP-DB 2.0: a renovated knowledgebase for deriving biological and chemical insight from metabolites, proteins, and genes. *Bioinformatics* **39**, (2023).
70. Wishart, D. S. et al. HMDB 5.0: the Human Metabolome Database for 2022. *Nucleic Acids Res.* **50**, D622–D631 (2022).
71. Kriel, J. et al. An integrative spatial multi-omic workflow for unified analysis of tumor tissue. Preprint at *bioRxiv* https://doi.org/10.1101/2024.10.15.618574 (2024).
72. Kriel, J. et al. An integrative spatial multi-omic workflow for unified analysis of tumor tissue. *BioImage Archive* https://doi.org/10.6019/S-BIAD1426 (2024).
73. Clifton, K. et al. STalign: alignment of spatial transcriptomics data using diffeomorphic metric mapping. *Nat. Commun.* **14**, 8123 (2023).

74. Raimundo, F., Vallot, C. & Vert, J. P. Tuning parameters of dimensionality reduction methods for single-cell RNA-seq analysis. *Genome Biol.* **21**, 212 (2020).
75. Ameen, F., Robertson, N., Lin, D. M., Ghazanfar, S. & Patrick, E. Kontextual: reframing analysis of spatial omics data reveals consistent cell relationships across images. Preprint at *bioRxiv* https://doi.org/10.1101/2024.09.03.611109 (2024).
76. Vannan, A. et al. Spatial transcriptomics identifies molecular niche dysregulation associated with distal lung remodeling in pulmonary fibrosis. *Nat. Gen.* **57**, 647–658 (2025).
77. Hamilton, W. L., Ying, R. & Leskovec, J. Inductive representation learning on large graphs. Preprint at https://arxiv.org/abs/1706.02216 (2017).

Acknowledgements

We thank A. Fakhri and S. Stylli for expert curation of the Royal Melbourne Hospital Neurosurgery Brain and Spine Tumour Tissue Bank, R. Linklater and R. Huynh for expert study management, M. Bisignano for assistance at the RMH Anatomical Pathology Department, E. Tsui for assistance at the WEHI Histology core and C. Anttila and L. Ling for assistance at the WEHI genomics facility, and J. Frederik Wojak and W. Najjar for volumetric analysis of imaging. At Metabolomics Australia, we thank P. Quiambao for assistance with sample preparation and extraction and A.L. Peterson for early optimization and data analysis of metabolomic data. We thank N. Schlesinger and R.G. Kost for support and access to the RPPS instrument. We thank M.L. Labat, M. Eckersley-Maslin and D. McCarthy for critical review. This trial was funded by AnHeart Therapeutics Inc and the Victorian Government, under The Brain Perioperative Clinical Trial Program (Brain-POP) Grant. This study was made possible and financially supported in part through the authors' membership of the Brain Cancer Centre, through support from Carrie's Beanies 4 Brain Cancer and through the Victorian State Government Operational Infrastructure Support and Australian Government NHMRC Independent Research Institutes Infrastructure Support Scheme (IRIISS). Further support included funding from the Venture Grants Scheme administered by Cancer Council Victoria (VG2022 to S.A.B., S.F. and J.R.W.), support from the NHMRC (2033815 to J.R.W.; 1178568 to S.G.), support from the Medical Research Future Fund (MRF2019448 to K.J.D., S.G., L.M.P., S.A.B., S.F. and J.R.W), Victorian Cancer Agency Mid-Career Research Fellowship (MCRF22003 to S.A.B.), WEHI Page Betheras Award (S.A.B.), WEHI IPSI Scholarship (O.E.F.), WEHI Johnson PhD Scholarship (J.J.D.M.), Australian Government Research Training Program Scholarship (J.J.D.M. and M.S.), Dine for a Cure Legacy Scholarship (M.S.), CSL Translational Data Science Scholarship (J.J.D.M.) and Gregg Symons Scholarship for Brain Cancer Research (O.E.F.). The funders had no role in study design, data collection and analysis, decision to publish or preparation of the paper.

Author contributions

K.J.D., M.A.R., S.A.B., S.F. and J.R.W. conceptualized the study. K.J.D., R.T., M.A.R. and J.R.W. obtained funding for the study. K.J.D., V.K.N., B.N., L.M.P., S.G., M.A.R., S.A.B., S.F. and J.R.W. developed the methods. K.J.D., S.A.C., J.J., S.S., M.T., J.D., M.A.R. and J.R.W. were clinical investigators for the study. A.L.V., Z.M., O.E.F. and S.R.-T. processed tissue for the study. O.E.F. and S.R.-T. performed pathology analysis. J.J., D.M. and E.L. performed radiology analysis. T.L., V.K.N., B.N. and S.A.B. performed metabolomic studies and related analysis. M.V.-A. and S.d.S. planned, performed and analyzed histone modifications. C.B.M., J.H.A.V. and S.G. performed whole genome sequencing and curation. M.S. and S.F. performed the methylation analysis. M.S., J.J.D.M., Z.M. and S.F. developed the snRNA-seq methods and analyzed the data. M.S., J.K. and S.F. performed spatial transcriptomic studies and associated analyses. J.K. performed imaging processing and analysis. M.S., T.L. and S.F. performed bioinformatic analyses. H.M., M.R., H.G. and L.M.P. performed patch clamping and associated analyses. K.J.D., V.S. and S.F. analyzed RPPS data. S.A.B., S.F. and J.R.W. drafted the paper. All authors reviewed and approved the final paper.

Competing interests

K.J.D. reports research funding from AnHeart Therapeutics to the institute (Royal Melbourne Hospital). J.R.W. reports research funding from AnHeart Therapeutics to the institute (WEHI), receiving consulting fees from AnHeart Therapeutics and Servier, being on advisory boards for Roche and Merck, and being a data safety monitoring member for Telix Pharmaceuticals. The other authors declare no competing interests.

Additional information

Extended data is available for this paper at https://doi.org/10.1038/s41591-025-03884-4.

Supplementary information The online version contains supplementary material available at https://doi.org/10.1038/s41591-025-03884-4.

Correspondence and requests for materials should be addressed to Katharine J. Drummond or James R. Whittle.

Peer review information *Nature Medicine* thanks Shawn Hervey-Jumper, Chen Hu, Diana Shi, Alpaslan Tasdogan and the other, anonymous, reviewer(s) for their contribution to the peer review of this work. Primary Handling Editor: Ulrike Harjes, in collaboration with the *Nature Medicine* team.

Reprints and permissions information is available at www.nature.com/reprints.

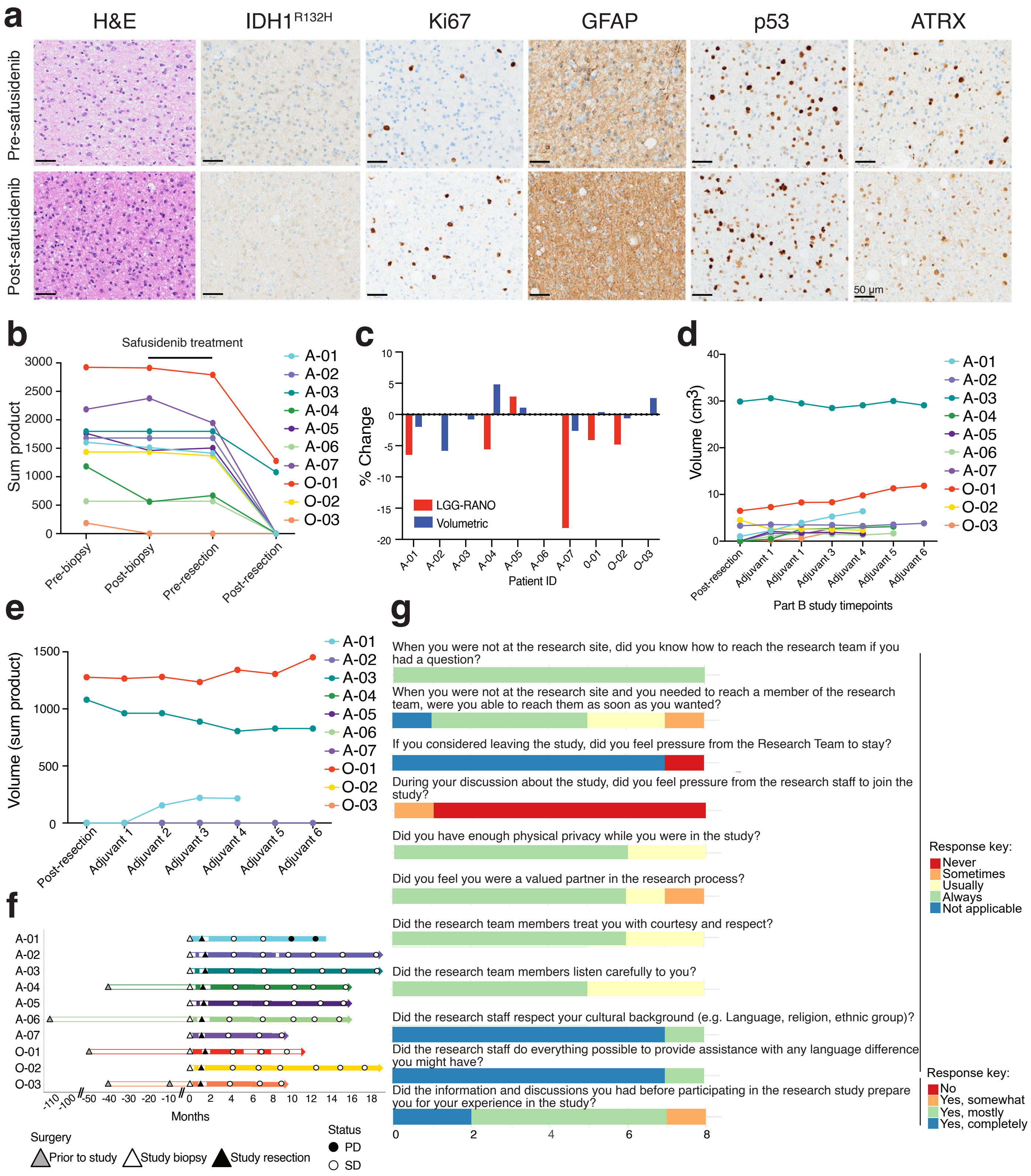

Extended Data Fig. 1 | Part A outcome data. a. Immunohistochemistry staining of participant O-01 pre- and post-safusidenib treatment (mIDH-R132H, ATRX, GFAP, P53, Ki67) and Hematoxylin and Eosin (H&E) stain. Scale, 50 µm. Representative of immunohistochemistry staining across n = 10 participants. **b.** LGG RANO values from participants through Part A of the study. **c.** Percent change in tumor size pre- and post-safusidenib treatment according to LGG-RANO or volumetric assessment. **d.** Volumetric analysis of tumor volume (cm^3) for T2/FLAIR sequences in each participant over time in Part B of the study. **e.** LGG RANO values from participants through Part B of study. **f.** Swimmer plot depicting response assessment by LGG-RANO in months post biopsy. Triangles indicate surgical procedures and circles indicate study status. PD refers to progressive disease and SD refers to stable disease. Safusidenib treatment periods are depicted by solid colored lines, and arrowheads indicate ongoing treatment. Note that breaks in the x-axis indicate non-continuous intervals. **g.** Research Participant Perception Survey (RPPS) results from n = 8 participants who completed the survey.

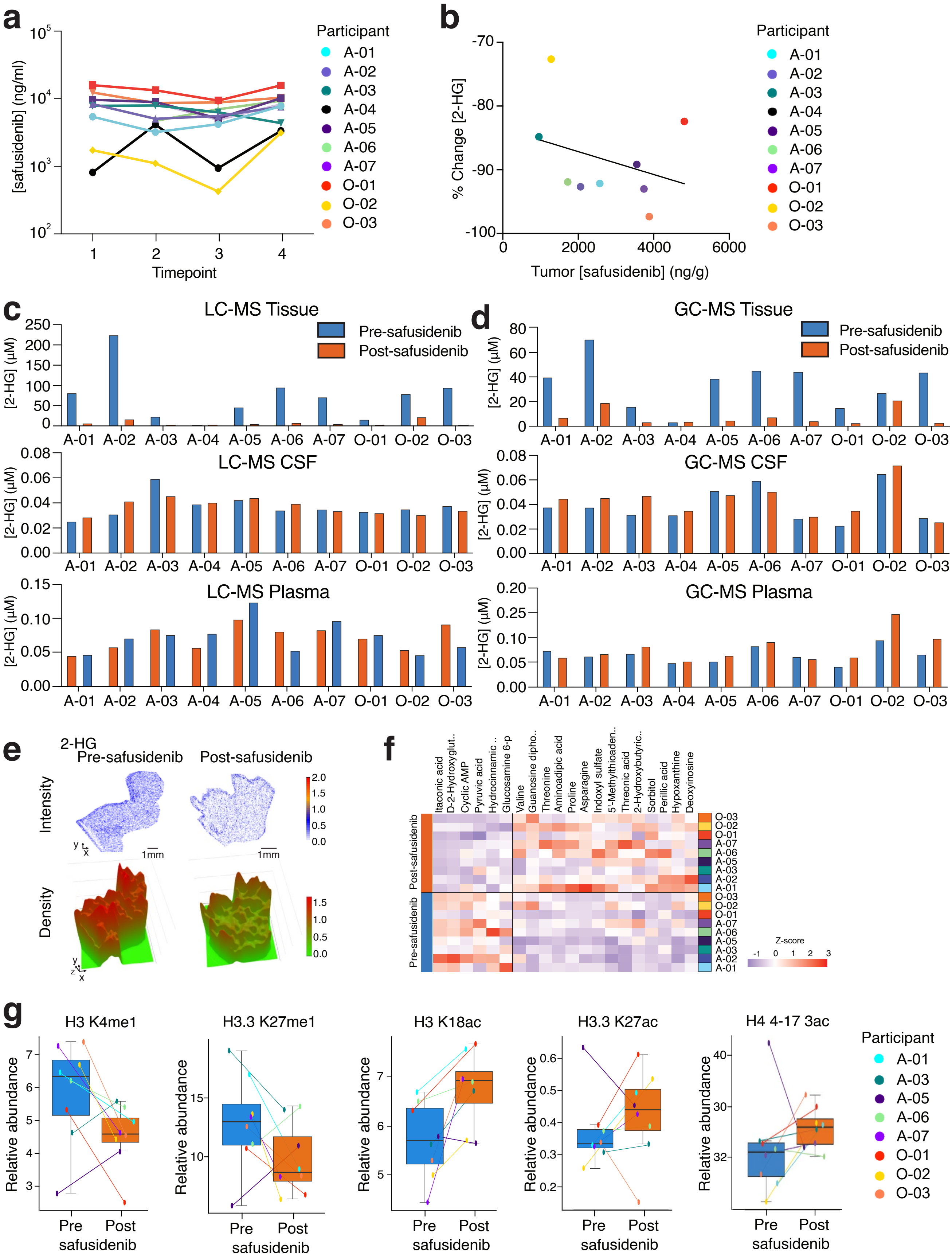

Extended Data Fig. 2 | See next page for caption.

Extended Data Fig. 2 | Metabolic and histone changes following safusidenib treatment. a. Longitudinal concentration (ng/mL) of safusidenib in the plasma over the four post-safusidenib study timepoints: days 1, 8, post 15, 28, and day of surgery (± 2 days) (n = 10 matched longitudinal samples). **b**. Correlation of percent change in 2-HG with participant tumor safusidenib concentration (n = 10 participants). **c**. 2-hydroxyglutarate (2-HG) quantification (μM) by LC-MS in tissue, CSF and plasma at the pre- and post-safusidenib timepoints (n = 10 matched samples). **d**. 2-HG quantification (μM) by GC-MS in tissue, CSF and plasma at the pre- and post-safusidenib timepoints (n = 10 participants). **e**. Spatial metabolomics examining 2-HG (m/z: 209.10 adducts: M+IsoProp+H) in participant A-05. Detected intensity score, above, 3D density map extrapolated from intensity, below. Scale, 1 mm. **f**. Heatmap of the top altered metabolites in each sample. **g**. Specific histone marks altered pre- and post-safusidenib (n = 8 participants). Box indicates IQR, centre line is median; whiskers extend to the furthest points within 1.5 × IQR.

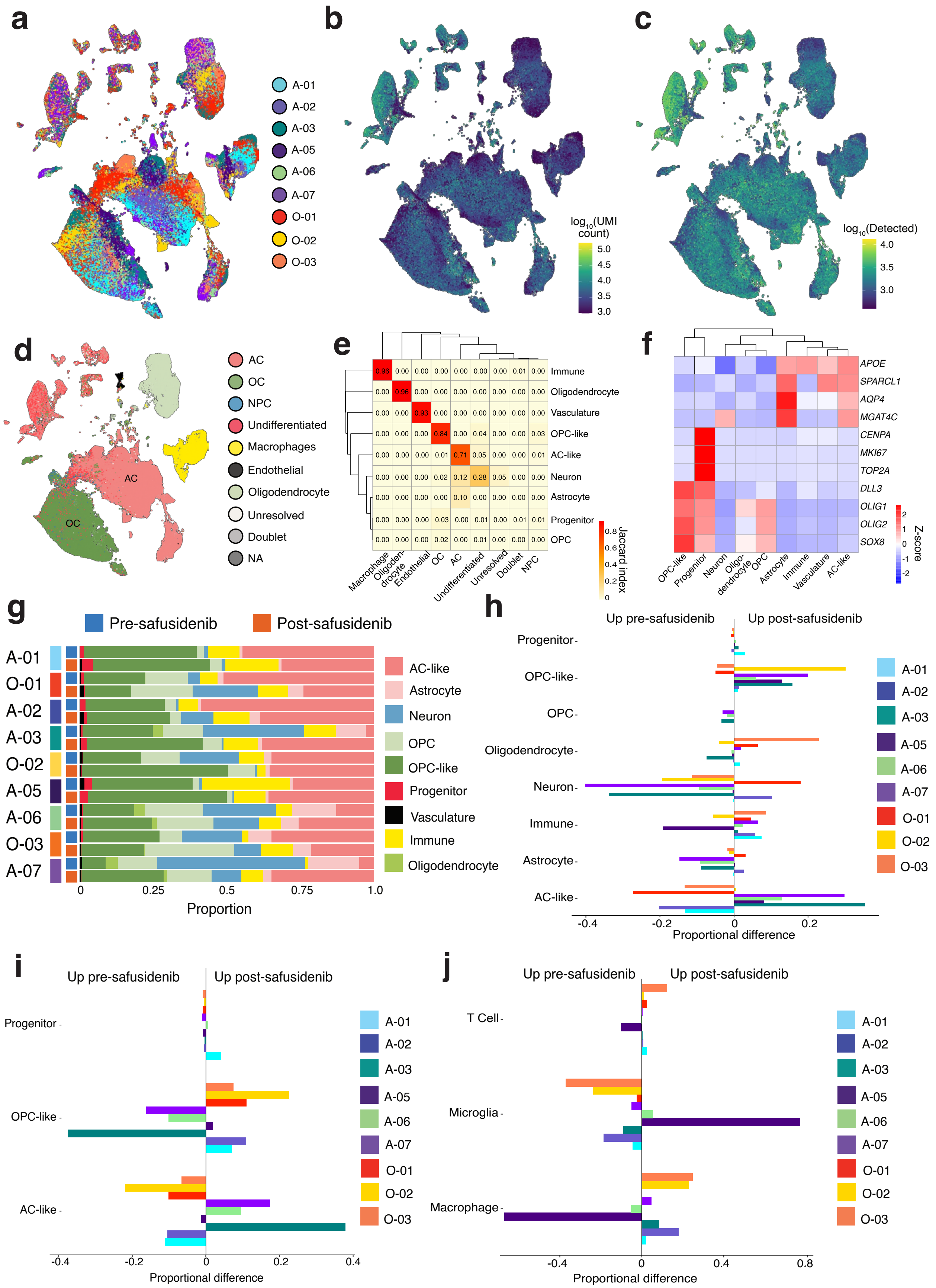

Extended Data Fig. 3 | See next page for caption.

Extended Data Fig. 3 | Safusidenib impact on tumor microenvironment composition. a. UMAP overlaid with participant origin for each nucleus. **b**. UMAP colored by UMI count ($\log_{10}$ transformed). **c**. UMAP colored by number of detected genes ($\log_{10}$ transformed). **d**. UMAP of snRNA-seq data colored by closest cell annotation match in *Spitzer* et al.[29] predicted using SingleR. **e**. Confusion matrix of proposed cell annotation versus predicted *Spitzer* at al. cell annotation. **f**. Heatmap of z-score of average expression of well-established markers in different cell types. **g**. Bar plot of proportion of cell types pre- and post-safusidenib for each participant from snRNA-seq data. **h**. Difference in proportion of all major cell types between snRNA-seq samples pre- and post-safusidenib. **i**. Difference in proportion of tumor cell types between snRNA-seq samples pre- and post-safusidenib. **j**. Difference in proportion of immune cell types between snRNA-seq samples pre- and post-safusidenib.

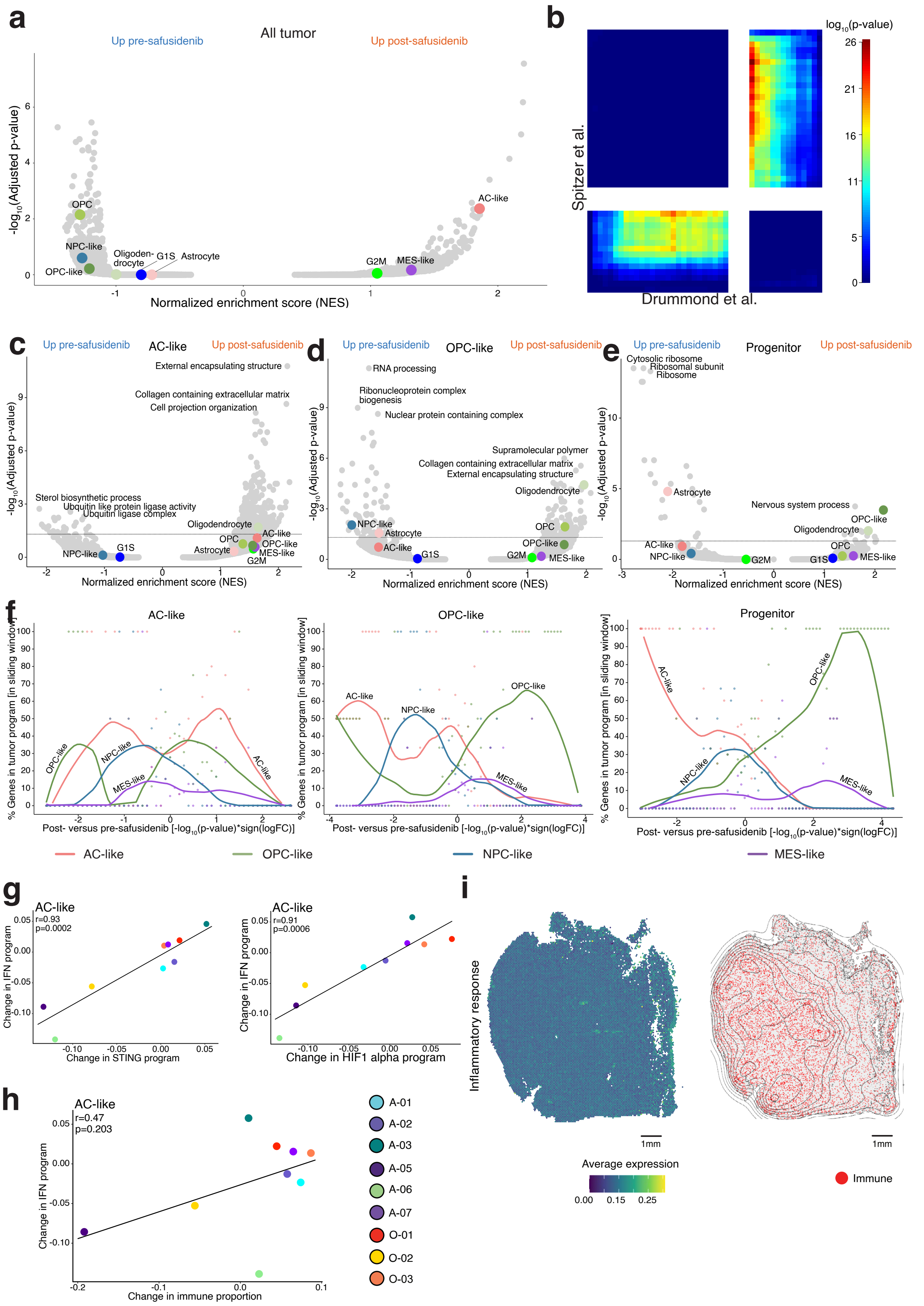

Extended Data Fig. 4 | See next page for caption.

Extended Data Fig. 4 | Gene program changes in response to safusidenib treatment. a. Comparison of all tumor cells in matched pre- and post-safusidenib samples using GSEA following the methodology described by *Spitzer* et al[1]. Each dot represents a gene-set. X axis shows the GSEA normalized enrichment score (NES), Y axis shows the Adjusted p-value. **b**. RRHO2 plot comparing GSEA results for all cells to GSEA analysis performed by *Spitzer* et al. Negative $\log_{10}$ p-values represent the correlation strength, and low p-values in the upper right and lower left quadrants represent concordant up and down regulation, respectively. **c**. Comparison of AC-like tumor cells in matched pre- and post-safusidenib samples using GSEA via ranked lists according to DEG results. Each dot represents a gene-set and color indicates whether the gene-set belongs to a glioma program and top enriched pathways are annotated. X axis shows the GSEA normalized enrichment score (NES), Y axis shows the adjusted p-value. Line indicates significance threshold (Adjusted p-value 0.05). **d**. As in (c) for OPC-like tumor cells. **e**. As in (c) for Progenitor tumor cells. **f**. Enrichment of the ranked list used for GSEA via ranked lists according to DEG results for AC-like (left), OPC-like (middle) and progenitor cells (right). Dots represent the percentage of genes, in a sliding window of 30 genes at fixed intervals of 0.10 (by $-\log_{10}$ p-value accounting for the direction of logFC), that overlap four main glioma programs. Trend line was computed using LOESS regression. **g**. Log-fold change in the IFN program compared to log-fold change in STING and HIF-1-alpha programs in AC-like tumor cells pre- relative to post-safusidenib treatment (n = 9 participants, t-test). Participant legend as in (h). **h**. Log-fold change in the IFN program in AC-like tumor cells compared to proportional change in immune cells pre- relative to post-safusidenib treatment (n = 9 participants, t-test). **i**. Spatial maps of the average log expression of genes in “Inflammation Response” pathway (left) and cells annotated as immune cells (right) with cell density indicated by contour plots for participant O-01. Pathway inferred by CytoSPACE integration of spatial transcriptomics and snRNA-seq and summarized as hex bins. Scale, 1 mm.

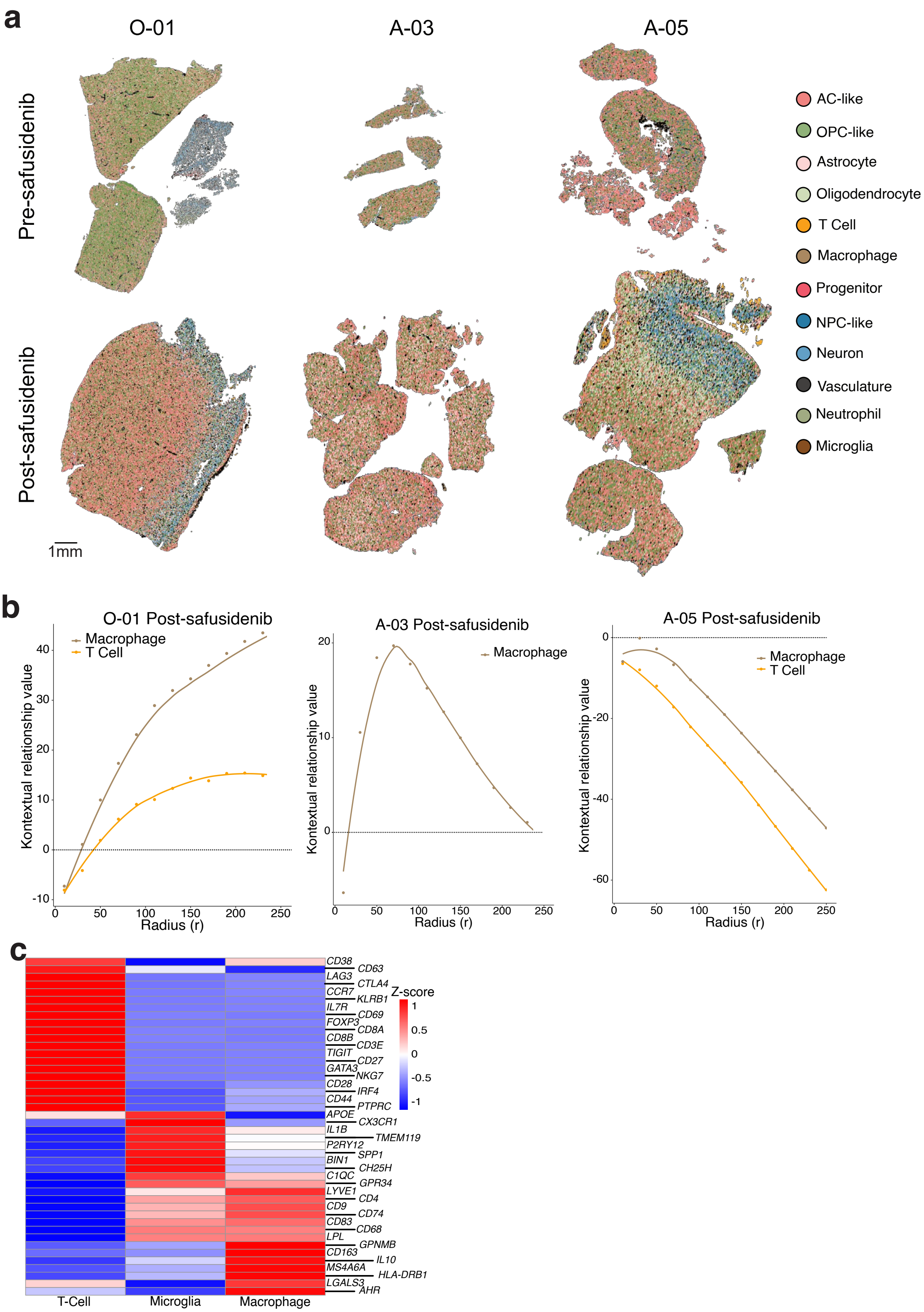

Extended Data Fig. 5 | Spatial distribution of cell states in the tumor microenvironment. a. Spatial map of cell type annotations for participants O-01, A-03 and A-05 matched pre- and post-safusidenib Xenium samples. Scale, 1 mm. **b**. Co-localization plots for Xenium post-safusidenib samples from infiltrating immune cell types to vasculature in the spatial context of all immune populations. Kontextual relative score evaluated over radii of 10 µm to 250 µm, at intervals of 20 µm. **c**. Heatmap of z-score of average expression of well-established immune markers across immune cell types from snRNA-seq data.

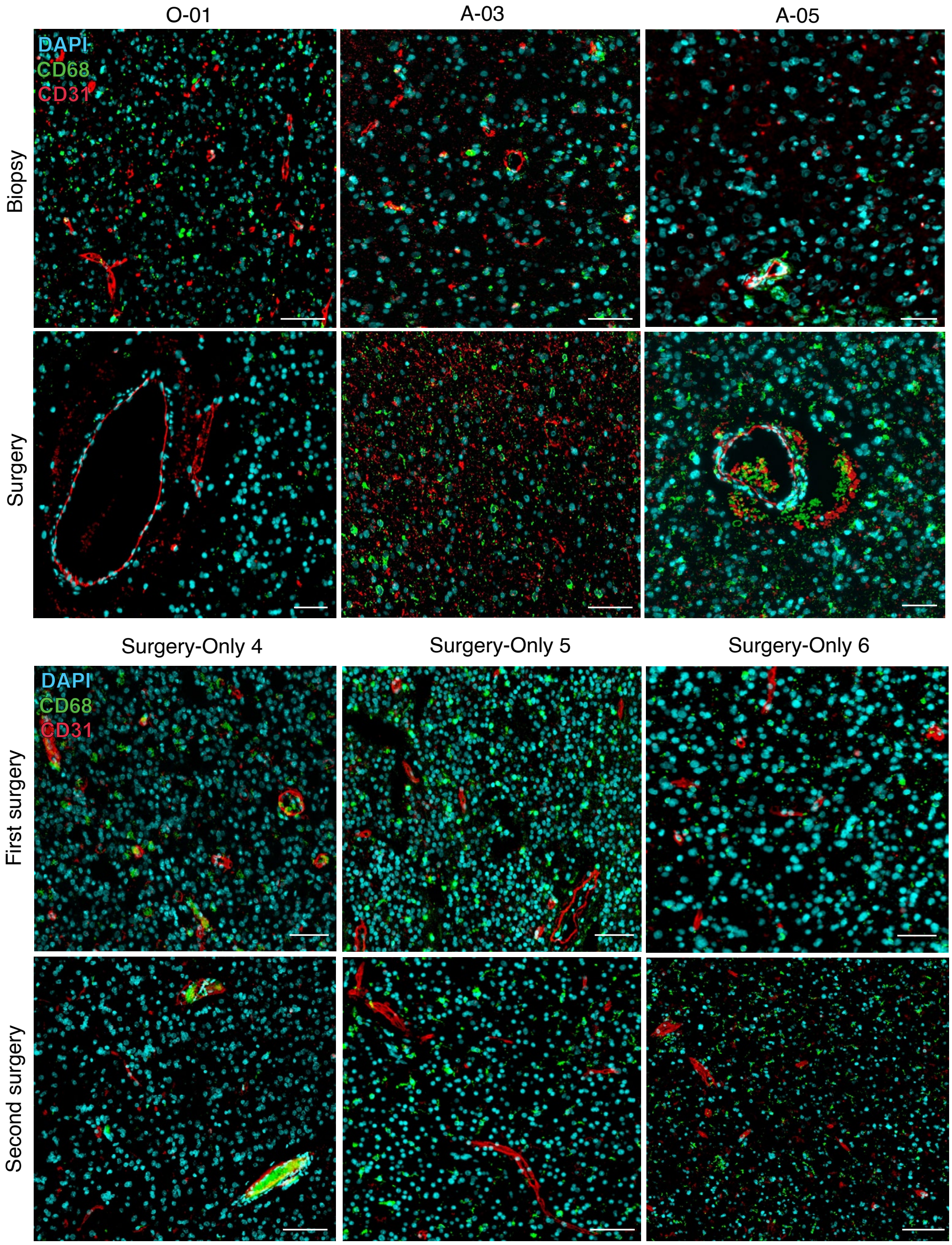

Extended Data Fig. 6 | Macrophage distribution changes as a result of surgery. Immunofluorescence conducted for DAPI (cyan), CD68 (green) and CD31 (red). Top panels, trial participant samples O-01, A-03 and A-05 biopsy (pre-safusidenib, n = 3 participants) and surgery (post-safusidenib, n = 3 participants). Bottom panels, surgery-only (no intervening treatment) samples 4, 5, 6, at first surgery and second surgery (n = 6 patients per condition). Scale bar, 50 µm.

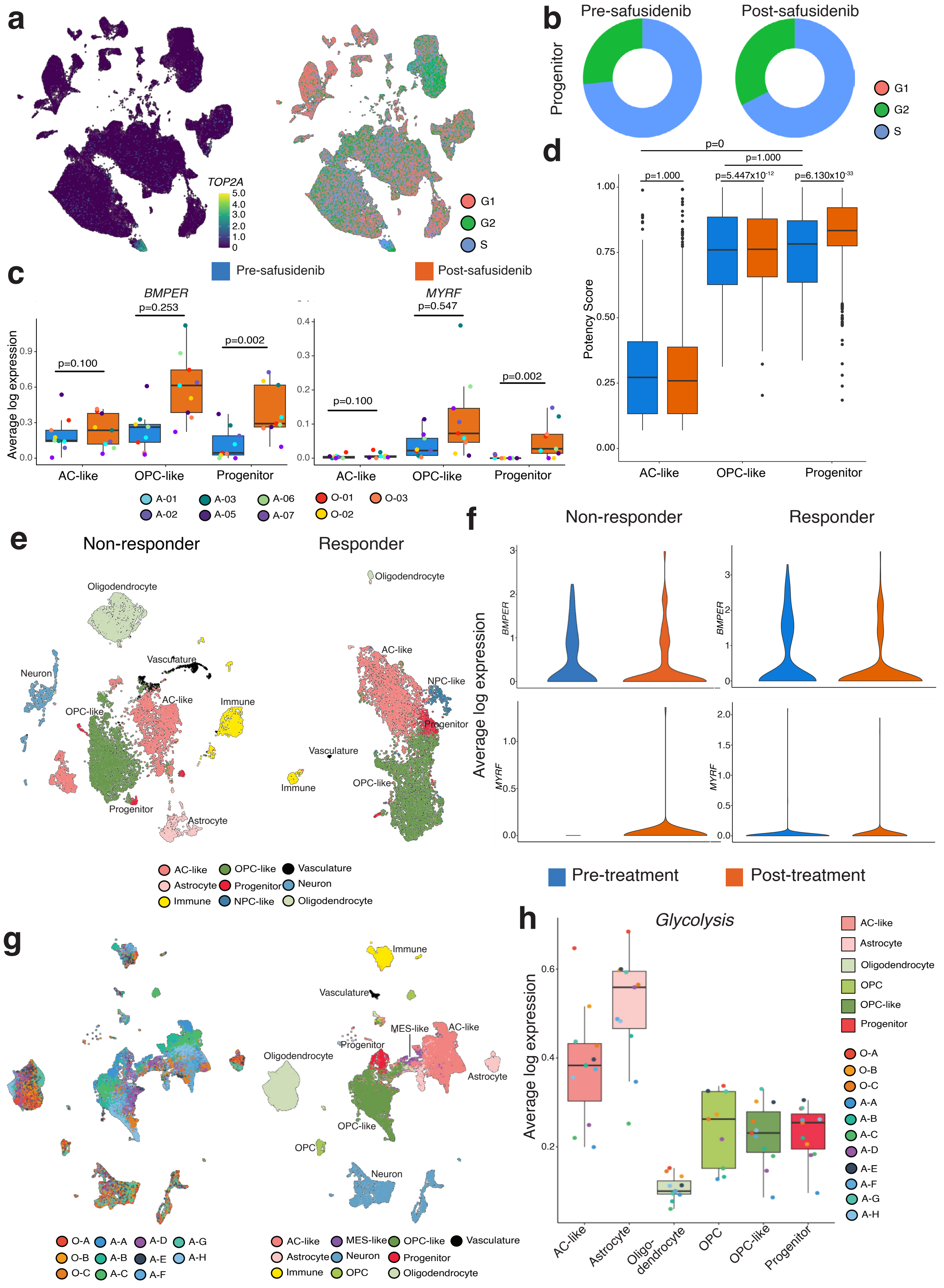

Extended Data Fig. 7 | See next page for caption.

Extended Data Fig. 7 | Differentiation features of response. a. UMAP colored by TOP2A log expression (left) and inferred cell cycle phase inferred by Seurat (right). **b**. Donut plot of proportion of cell cycle phases in Progenitor cells pre- and post-safusidenib. **c**. Average log expression per tumor cell population for each participant pre- and post-safusidenib for *BMPER* (left) and *MYRF* (right). Significant comparisons are indicated (n = 9 participants, DEG testing with limma). Box indicates IQR, centre line is median; whiskers extend to the furthest points within 1.5 × IQR. **d**. Box plot of differentiation potency scores for each tumor cell population pre- and post-safusidenib. Significant comparisons are indicated (n = 9 participants, pairwise t-test and one-sided t-test). Box indicates IQR, centre line is median; whiskers extend to the furthest points within 1.5 × IQR. Participant sample legend as in (**c**). **e**. UMAP of Responder and Non-responder with matched pre- and post- mIDH inhibitor samples from *Spitzer* et al[1] colored by cell annotation. **f**. Violin plot of *MYRF* and *BMPER* gene expression in progenitor population pre- and post-mIDH inhibitor for responder (left) and non-responder (right). **g**. UMAP of LGG reference cohort of 11 patients colored by donor (left) and cell annotation (right). **h**. Box plot of glycolysis average log expression per sample in different cell populations in LGG reference cohort (n = 11 patients). Box indicates IQR, centre line is median; whiskers extend to the furthest points within 1.5 × IQR.

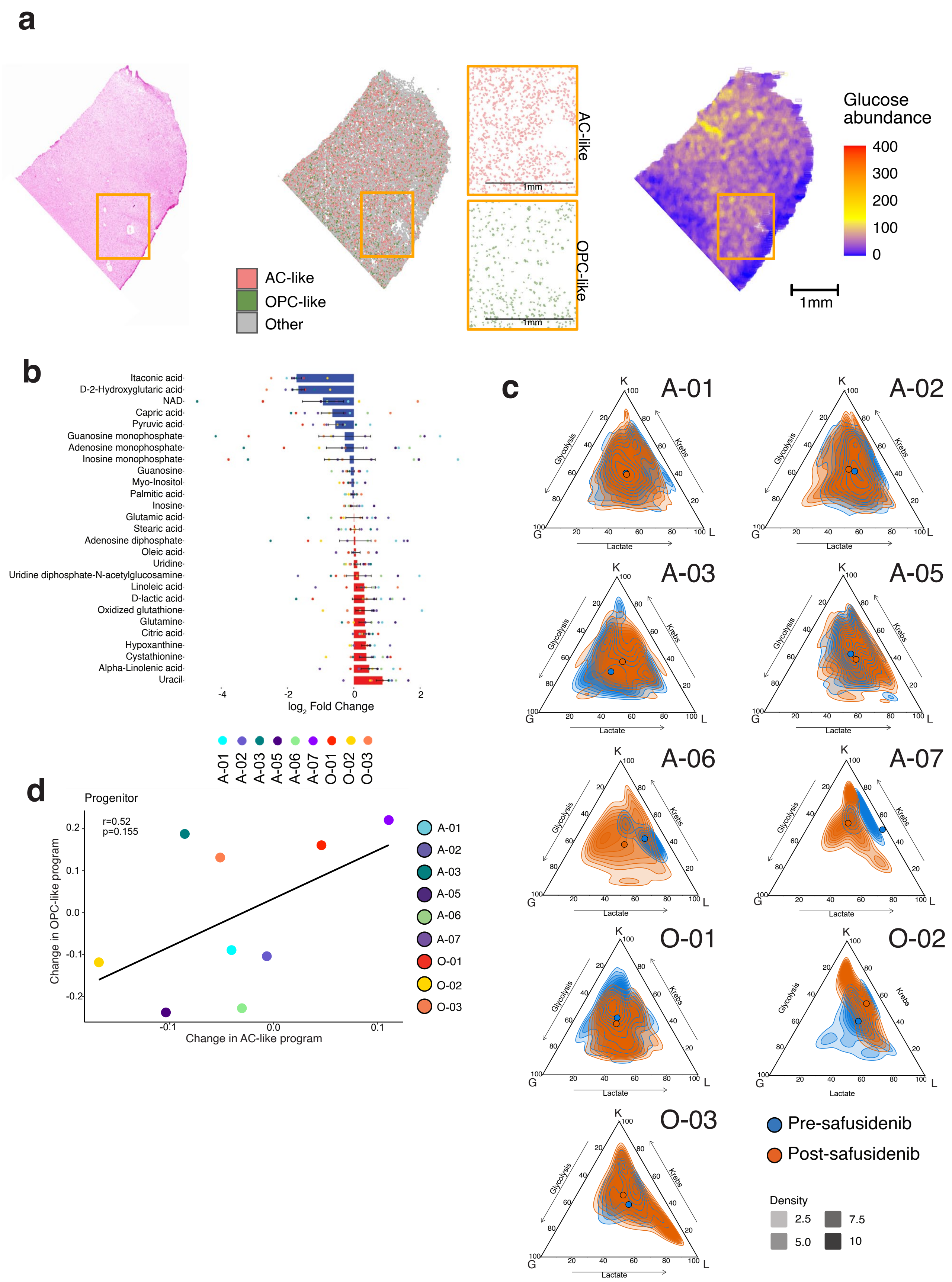

Extended Data Fig. 8 | See next page for caption.

Extended Data Fig. 8 | Multiparametric analysis of tumor metabolism. a. H&E (left), spatial map indicating location of all AC-like and OPC-like tumor cells, with insets indicating the individual spatial distribution of each cell type separately (middle) and spatial metabolomics of average glucose abundance (m/z: 203.05 Adducts: M+Na) visualized in grids (right). The orange box indicates example tumor region depicted in Fig. 2e. **b**. Waterfall plot of the log-fold change in top 25 altered metabolites in pre- compared to post-safusidenib samples. Each participant sample is depicted by a colored point (n = 9 participants). Mean values ± SEM. **c**. Ternary plots comparing transcriptional metabolic programs in progenitor cells for Krebs, Lactate and Glycolysis in pre- compared to post-safusidenib. **d**. Log-fold change in the OPC-like program versus log-fold change in AC-like program in progenitor tumor cells pre- relative to post-safusidenib treatment (n = 9 participants, t-test).

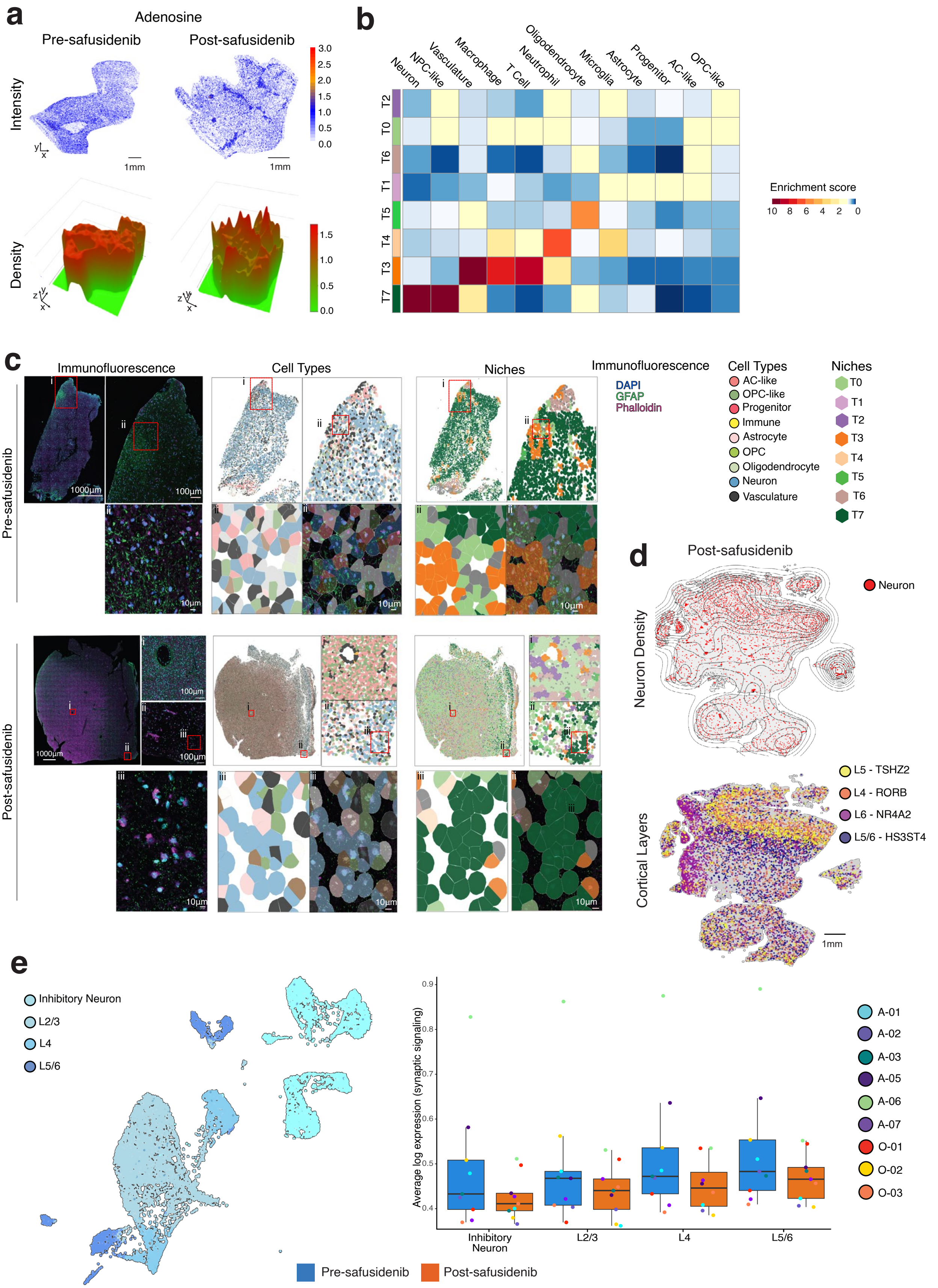

Extended Data Fig. 9 | See next page for caption.

Extended Data Fig. 9 | Neuronal localization and distribution across transcriptomic niches. a. Spatial metabolomics examining adenosine (m/z: 268.09 adducts: M + H) in participant A-05 tumor. Detected intensity score, above, 3D density map extrapolated from intensity, below. Scale, 1 mm. **b**. Enrichment heat map of each cell type identified co-localized within the transcriptional niches. **c**. Overlayed immunofluorescence, cell types and transcript niches in participant O-01 pre- and post-safusidenib (n = 3 per condition). Scales depicted in relevant immunofluorescence inset (left), 1000 µm, 100 µm and 10 µm. Immunofluorescence: DAPI, blue; GFAP, green; Phalloidin, magenta. Cell type annotations with immunofluorescence overlay (bottom right panel) and Niche subsets with immunofluorescence overlay (bottom right panel). **d**. Spatial maps of participant A-05 post-safusidenib sample indicating presence of neurons (red) with associated density contour plot (left) and showing cells expressing key neuronal layer markers (right) profiled with Xenium. Scale 1 mm. **e**. UMAP of neurons colored by neuron cell annotation (left). Box plot of synaptic signaling average log expression for each participant in different neuron populations pre- and post-safusidenib. Box indicates IQR, centre line is median; whiskers extend to the furthest points within 1.5 × IQR.

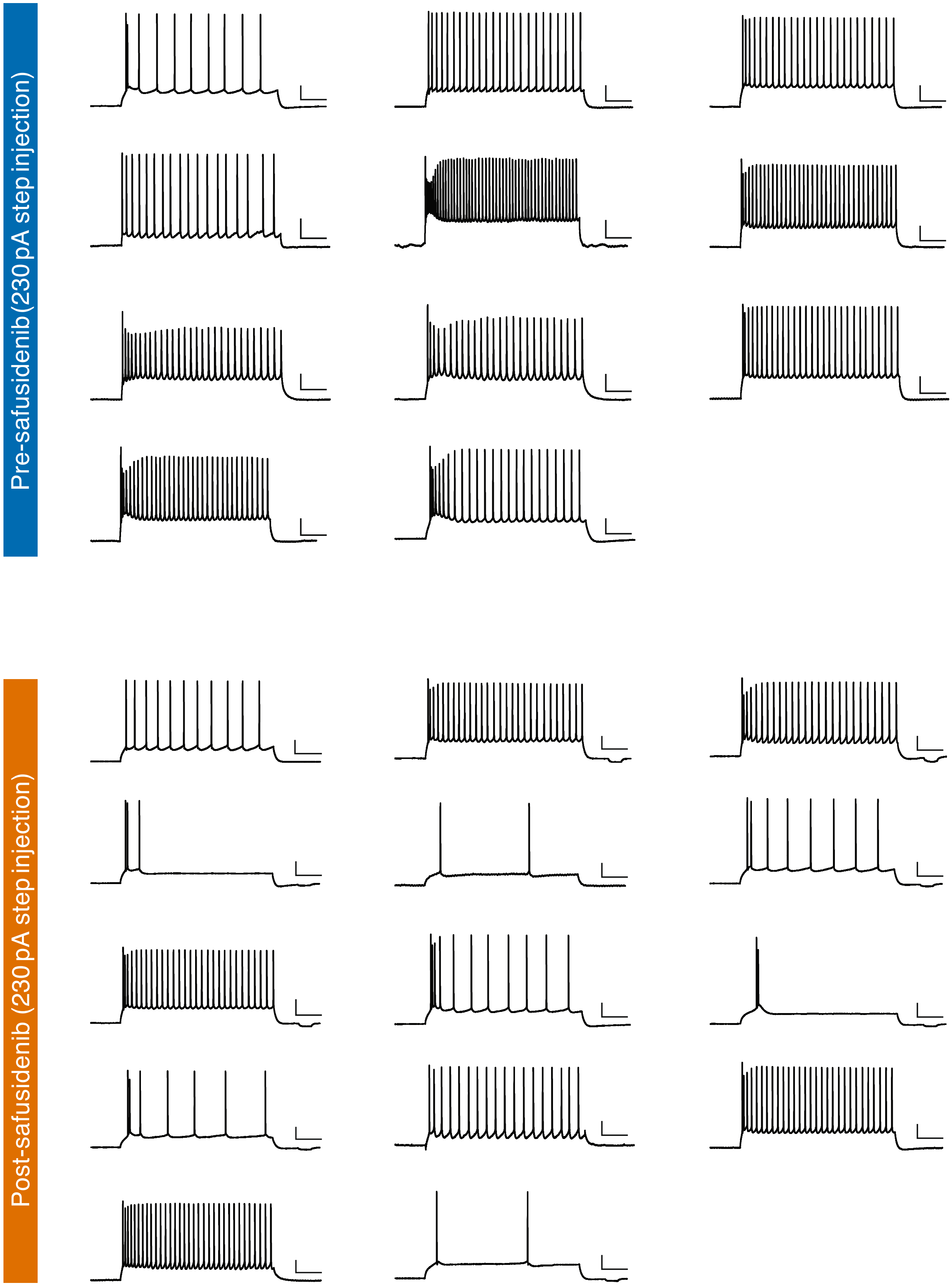

Extended Data Fig. 10 | Electrophysiology of neurons in response to safusidenib treatment. Example whole-cell patch clamp recordings from each pyramidal neuron recorded within tissue samples obtained from patients pre- (top; n = 11 neurons) and post- (bottom; n = 14 neurons) treatment with the mIDH inhibitor. All voltage responses are in response to a 230 pA current step injection. Scale bar, 20 mV, 200 ms.

nature portfolio

Corresponding author(s): Drummond, Whittle

Last updated by author(s): Jun 4, 2025

Reporting Summary

Nature Portfolio wishes to improve the reproducibility of the work that we publish. This form provides structure for consistency and transparency in reporting. For further information on Nature Portfolio policies, see our Editorial Policies and the Editorial Policy Checklist.

Statistics

For all statistical analyses, confirm that the following items are present in the figure legend, table legend, main text, or Methods section.

n/a	Confirmed	
☐	☒	The exact sample size (*n*) for each experimental group/condition, given as a discrete number and unit of measurement
☐	☒	A statement on whether measurements were taken from distinct samples or whether the same sample was measured repeatedly
☐	☒	The statistical test(s) used AND whether they are one- or two-sided *Only common tests should be described solely by name; describe more complex techniques in the Methods section.*
☐	☒	A description of all covariates tested
☐	☒	A description of any assumptions or corrections, such as tests of normality and adjustment for multiple comparisons
☐	☒	A full description of the statistical parameters including central tendency (e.g. means) or other basic estimates (e.g. regression coefficient) AND variation (e.g. standard deviation) or associated estimates of uncertainty (e.g. confidence intervals)
☐	☒	For null hypothesis testing, the test statistic (e.g. *F*, *t*, *r*) with confidence intervals, effect sizes, degrees of freedom and *P* value noted *Give P values as exact values whenever suitable.*
☒	☐	For Bayesian analysis, information on the choice of priors and Markov chain Monte Carlo settings
☒	☐	For hierarchical and complex designs, identification of the appropriate level for tests and full reporting of outcomes
☐	☒	Estimates of effect sizes (e.g. Cohen's *d*, Pearson's *r*), indicating how they were calculated

Our web collection on statistics for biologists contains articles on many of the points above.

Software and code

Policy information about availability of computer code

Data collection	No software was used
Data analysis	Custom code based on open-source software as outlined in supplementary methods; all code can be found at https//github.com/ MontanaSpiteri/AnHeart Custom code is based on R (v4.4.0) and includes use of ggplot2 (v3.5.1) for all figure creation as well as python (v3.11) Single-nuclei data was first processed using Cell Ranger (10X Genomics, v7.1.0) to align FASTQ format files to the hg38 reference genome. Processing was then performed in R using CellBender (v0.3.0), Scrublet (v0.2.3), scater (v.1.28.0), SingleCellExperiment (v1.22.0), scran (v1.33.1), scVI (v1.1.5), bluster (v1.10.0), SingleR (v.2.2.0), and Numbat (v1.4.0). Downstream analysis included the use of Seurat (v.1.22.0), CytoTRACE2 (v1.0.0), limma (v3.61.9), edgeR (v4.3.11), mSigDB (v10.0.2), entropy (v1.3.1), ggtern (v3.5.0), stats (v4.4.1) and RRHO2 (v1.0). Spatial metabolomics data was processed in R with Cardinal (v2.6.5) and matched against the Human Metabolome Database (v5.0). Downstream analysis included code based on stats (v4.3.0). Methylation data was analyzed using minifi (v1.50.0) in R. WGS data was analyzed using Illumina DRAGEN (v4.2). Spatial transcriptomics data was processed using Xenium Analyzer (v3) and the processed in R using packages also used in single nuclei analysis but also including intrinsicDimension (v1.2.0). Downstream analysis included sf (v1.0-17), Statial (v1.7.0), hexbin (v1.28.3) and GraphSAGE (v1). Imaging analysis of Xenium slides was completed using ZEN Blue software (v3.8).

Single nuclei and spatial transcriptomic data were combined using CytoSPACE (v1.1.0).
Epigenetic data of histone modifications was processed and plotted in R using packages also used in single nuclei analysis.
Bulk metabolomics data were analyzed using Shimadzu GCMSsolution Realtime Analysis (v5.34), Shimadzu Smart Metabolites Database (v3), Shimadzu LabSolutions InSight software (v3.6), El Malven software (v0.12.1) and TraceFinder Software (v4.1, Thermo Scientific™) after which downstream analysis was done in R using packages also used in single nuclei analysis. Bulk histone modification data was analysed using Skyline (v23.1.0.455).
All pathway analysis are based on fgsea (v1.30.0).
Analysis for clinical data was conducted in GraphPad Prism (v10.0.0).
Alignment of spatial metabolomics and transcriptomics was performed using STAlign(v1.0.1).
Hematoxylin and eosin (H&E) stained sections and immunohistochemistry slides were processed using CaseCentre online software (v2.9).
Adjacent sections were registered using wsireg (v0.3.5).
Electrophysiology data was analysed using minitab (v22.1).
Volumetric analysis was conducted with Brainlab software (Brainlab, iPlanNet v2.3.1.215.1, Munich, Germany).

For manuscripts utilizing custom algorithms or software that are central to the research but not yet described in published literature, software must be made available to editors and reviewers. We strongly encourage code deposition in a community repository (e.g. GitHub). See the Nature Portfolio guidelines for submitting code & software for further information.

Data

Policy information about availability of data

All manuscripts must include a data availability statement. This statement should provide the following information, where applicable:

- Accession codes, unique identifiers, or web links for publicly available datasets
- A description of any restrictions on data availability
- For clinical datasets or third party data, please ensure that the statement adheres to our policy

Study-level clinical and spatial data from this study will be made available upon reasonable request to the lead authors from a qualified medical or scientific professional for the specific purpose laid out in that request and may include deidentified individual participant data (requests evaluated within 4 weeks). The data for this request will be available after a data access agreement has been signed. Further translational data is available from dbGAP under accession code phs003976 after provision of IRB ethics approval and the snRNA-seq data for the independent LGG cohort is available at GEO under accession code GSE292732. Data for the matched spatial transcriptomics and metabolomics data from sequential sections of the same LGG tumor is available at BioImage Archive via DOI: 10.6019/S-BIAD1426.

Publicly available data from Spitzer et al. 2024 is available at GEO under the accession number GSE26099 under the terms and conditions specified by the data provider. Single-cell sequencing reads were aligned and quantified using the GRCh38 human reference genome (2020-A), a pre-built reference package provided by 10x Genomics (GENCODEv32/Ensembl98). The reference package is available at: https://www.10xgenomics.com/support/software/cell-ranger/latest/release-notes/cr-reference-release-notes#2020-a.

WGS reads were aligned using the hg38 reference available at DRAGEN Illumina: https://sapac.support.illumina.com/downloads/dragen-reference-genomes-hg38.html.

Research involving human participants, their data, or biological material

Policy information about studies with human participants or human data. See also policy information about sex, gender (identity/presentation), and sexual orientation and race, ethnicity and racism.

Reporting on sex and gender	Sex was reported at study baseline and 6/10 (60%) enrolled patients were male. Sex based analysis was not performed due to the small sample size and descriptive nature of the study design. Gender was self reported by participants in response to the Research Participant Perception Survey. Gender based analysis was not required for the study objectives.
Reporting on race, ethnicity, or other socially relevant groupings	"Race" was self reported by participants in response to the Research Participant Perception Survey. The terms used were modified from the original survey and obtained from the Australian Institute of Health and Welfare’s Metadata Online Registry (METEOR). No grouping or analysis was performed using race or ethnic data.
Population characteristics	Population characteristics are given in Table 1. Briefly, median age of participants was 33 (29-46), 4 female and 6 male participants, 3 with a diagnosis of oligodendroglomia and 7 with a diagnosis of astrocytoma, 6 with no prior resections and 4 with prior resections.
Recruitment	Between 21 December 2022 and 15 February 2024, 12 patients were consented and screened for the study. 1 withdrew consent prior to biopsy, 1 was withdrawn from study as histology from study biopsy reported a non-cancer diagnosis and was therefore no longer eligible for study treatment. Patients were eligible if they met the eligibility criteria, including a radiological or pathological diagnosis of IDH1 mutated LGG, not required to have urgent resection for mass effect or hydrocephalus according to the treating neurosurgeon and suitable for 2 stage biopsy and resection of the tumour. Biological endpoints using paired patient samples and dichotomous outcomes will limit biases. Potentially eligible patients were recruited from outpatient clinics or referred from external centres based on predefined eligibility criteria. This recruitment strategy may introduce self-selection bias, as individuals who are more motivated to seek further care are more likely to participate. Additionally, the study design and inclusion criteria for patients suitable for two surgical procedures introduces a bias towards patients of good performance status and particular disease characteristics.

	As this was a feasibility study, such bias could impact the generalizability of findings by overrepresenting individuals with certain health-seeking behaviors or demographic characteristics. However, in small-scale feasibility studies, this limitation is often unavoidable. The primary outcomes were feasibility and acceptability, while secondary outcomes focused on biological measures that are unlikely to be affected by recruitment bias. To mitigate potential biases, consistent inclusion criteria were applied, demographic characteristics were documented for transparency, and a screening log of all potential participants was maintained and summarized in the CONSORT .
Ethics oversight	The study protocol was approved by the Melbourne Health Human Research Ethics Committee on 30 March 2022.

Note that full information on the approval of the study protocol must also be provided in the manuscript.

Field-specific reporting

Please select the one below that is the best fit for your research. If you are not sure, read the appropriate sections before making your selection.

☒ Life sciences ☐ Behavioural & social sciences ☐ Ecological, evolutionary & environmental sciences

For a reference copy of the document with all sections, see nature.com/documents/nr-reporting-summary-flat.pdf

Life sciences study design

All studies must disclose on these points even when the disclosure is negative.

Sample size	Perioperative/Phase 0 studies are exploratory in nature and are designed primarily to gather preliminary data on pharmacokinetics (PK), pharmacodynamics (PD), and target engagement, rather than to test efficacy or establish statistically significant outcomes. For this perioperative study, no formal statistical sample size calculation was performed. Perioperative/Phase 0 studies are exploratory in nature and are designed primarily to gather preliminary data on pharmacokinetics (PK), pharmacodynamics (PD), and target engagement, rather than to test efficacy or establish statistically significant outcomes. Given the small number of patients typically involved and the focus on mechanistic insights rather than hypothesis testing, sample sizes were chosen based on feasibility, ethical considerations, and the need to obtain meaningful biological insights while minimizing patient exposure. Specifically, the biological endpoint is defined as: • Detection of drug in tumor • Evidence of on-target modulation These binary outcomes allow for assessment of agent activity on an individual level, without requiring large sample sizes. This approach is consistent with the current standards for early exploratory trials, where the emphasis is on characterizing the agent's biological activity and guiding further development rather than drawing definitive statistical conclusions.
Data exclusions	Translational research samples obtained for participant A-04 were removed due to low tumor purity. For single nuclei and spatial transcriptomic data we outline exclusion of nuclei and cells in Extended Table S1.
Replication	Due to the limited amount of patient samples, we did not replicate experiments.
Randomization	This study involves a single-arm design, where all participants received the investigational agent. As such, there is no comparison group that would necessitate random assignment. The endpoints are typically binary biological responses (e.g., presence or absence of drug in tumor tissue; on-target modulation), which are interpreted within the context of individual patient outcomes rather than between-group comparisons.
Blinding	Blinding was not implemented in this perioperative study because the trial design did not include a comparator or placebo arm, and the primary objectives were to assess the feasibility and acceptability of the study design.

Reporting for specific materials, systems and methods

We require information from authors about some types of materials, experimental systems and methods used in many studies. Here, indicate whether each material, system or method listed is relevant to your study. If you are not sure if a list item applies to your research, read the appropriate section before selecting a response.

Materials & experimental systems

n/a	Involved in the study
☐	☒ Antibodies
☒	☐ Eukaryotic cell lines
☒	☐ Palaeontology and archaeology
☒	☐ Animals and other organisms
☐	☒ Clinical data
☒	☐ Dual use research of concern
☒	☐ Plants

Methods

n/a	Involved in the study
☒	☐ ChIP-seq
☒	☐ Flow cytometry
☐	☒ MRI-based neuroimaging

Antibodies

Antibodies used	Primary antibodies: Anti-CD68 (DAKO PG-M1, clone PG-M1, 1:200 dilution), anti-GFAP (Cell Signaling Technologies 3670, clone GA5, 1:1000 dilution), anti-CD31 (Abcam ab134168, polyclonal, 1:500), anti-IDH1-R132H (Dianova IDA-H09, clone H09, 1:100 dilution), anti-MAP2A (ThermoFisher PA110005, polyclonal, 1:1000 dilution), anti-ATRX (Sigma HPA001906; polyclonal, 1:300 dilution), anti-TP53 (Leica Biosystems NCL-L-p53-DO7, clone DO7, 1:50 dilution), anti-Ki67 (Dako M7240; 1:100 dilution) Secondary Antibodies: Alexa Fluor 594 anti-rabbit (ThermoFisher A32740, polyclonal, dilution 1:1000), Alexa Fluor 647 anti-mouse (ThermoFisher A32728, polyclonal, dilution 1:1000), Alexa Fluor 488 anti-chicken (ThermoFisher A11039, polyclonal, dilution 1:1000), Alexa Fluor 488 anti-mouse (ThermoFisher A11004, polyclonal, dilution 1:1000).
Validation	The primary antibodies were validated for their respective applications as follows: Anti-CD68 (DAKO, clone PG-M1) was validated through immunohistochemistry on paraffin-embedded tissues (IHC-P), flow cytometry (FC), and immunofluorescence (IF). Anti-GFAP (Cell Signaling Technologies, #3670, clone GA5) was validated through Western blotting (WB), immunoprecipitation (IP), immunohistochemistry on both paraffin-embedded and frozen tissues (IHC-P, IHC-F), immunofluorescence (IF-IC, IF-F), and flow cytometry (FC). For anti-CD31 (Abcam, ab134168, polyclonal), validation was through immunohistochemistry on frozen sections (IHC-Fr) and flow cytometry (FC) by the manufacturer, with additional literature supporting its use in IHC-P and WB. The anti-IDH1-R132H antibody (Dianova, DIA-H09, clone H09) was validated through immunohistochemistry on paraffin-embedded tissues (IHC-P) and Western blotting (WB). Validation for anti-MAP2A (ThermoFisher, PA1-10005, polyclonal) was through Western blotting (WB), immunohistochemistry (IHC), and immunofluorescence (IF). Anti-ATRX (Sigma, HPA001906, polyclonal) was validated through immunohistochemistry (IHC) and Western blotting (WB), with extensive public IHC data supporting its use. Lastly, anti-TP53 (Leica Biosystems, NCL-L-p53-DO7, clone DO-7) was validated through immunohistochemistry on paraffin-embedded tissues (IHC-P).

Clinical data

Policy information about clinical studies

All manuscripts should comply with the ICMJE guidelines for publication of clinical research and a completed CONSORT checklist must be included with all submissions.

Clinical trial registration	NCT05577416
Study protocol	The study procedures and methodology are outlined in Cain et al. Future Oncology, 2024. Since the trial is still ongoing the full protocol is not available at this point.
Data collection	Data was recorded in electronic case report forms (eCRF) by site clinical research staff from electronic medical record source data. Patients were recruited between 21 December 2022 and 15 February 2024, and data collected up to 8th November 2024. All clinical, safety and efficacy data was reported in the eCRF.
Outcomes	The primary endpoint was feasibility, with at least 60% of patients screened and undergoing biopsy completing all planned investigations and procedures, and study samples informative for PK and PD. The secondary endpoints were safusidenib toxicity (occurrence, type, severity and relationship of adverse events); safety of planned craniotomy and resection after stereotactic biopsy (30-day morbidity and mortality post surgery, delays in planned resection, number of emergency resections and number of unplanned admissions); biological activity of Safusidenib (change in 2-HG levels in plasma, tumour and CSF); Pharmacokinetics of Safusidenib (drug concentration in plasma, CSF and tumour, correlated with clinical safety and clinical activity); overall response (Best response to Safusidenib based on change in extent of FLAIR and contrast enhancement on MRI, and best response to Safusidenib based on LGG-RANO); and improved understanding of patients' perspective on the peri-operative design and satisfaction with study procedures using the Research Participant Perception Survey short form (RPPS).

Plants

Seed stocks	*Report on the source of all seed stocks or other plant material used. If applicable, state the seed stock centre and catalogue number. If plant specimens were collected from the field, describe the collection location, date and sampling procedures.*
Novel plant genotypes	*Describe the methods by which all novel plant genotypes were produced. This includes those generated by transgenic approaches, gene editing, chemical/radiation-based mutagenesis and hybridization. For transgenic lines, describe the transformation method, the number of independent lines analyzed and the generation upon which experiments were performed. For gene-edited lines, describe the editor used, the endogenous sequence targeted for editing, the targeting guide RNA sequence (if applicable) and how the editor was applied.*
Authentication	*Describe any authentication procedures for each seed stock used or novel genotype generated. Describe any experiments used to assess the effect of a mutation and, where applicable, how potential secondary effects (e.g. second site T-DNA insertions, mosiacism, off-target gene editing) were examined.*

Magnetic resonance imaging

Experimental design

Design type	MRI imaging acquired at screening and at pre determined intervals during study using site standard imaging protocol for glioma, including advanced sequences (MR spectroscopy and perfusion imaging sequences)and fluid-attenuated inversion recovery (FLAIR).
Design specifications	Clinical MRI scans and protocols with standard clinical vendor provided post processing
Behavioral performance measures	LGG-RANO criteria for evaluating response

Acquisition

Imaging type(s)	Structural, diffusion weighted imaging, dynamic susceptibility contrast perfusion
Field strength	3T
Sequence & imaging parameters	3D-T1 pre and post contrast (0.9mm isotropic, FA=9 degrees, TR=2020ms, TE=2.35ms, TA=5:47min), Axial SE DWI (1x1x4mm, FA=180 degrees, TR=7670ms, TE1=59ms, TE2=99ms, b-value1=0, b-value2=1000s/mm^2, TA=3:29min), Axial FLAIR (0.6x0.6x4mm, FA=150degrees, TR=8500ms, TE=76ms, TA=3:09min), 3D FLAIR (0.8mm isotropic, TR=7000ms, TE=384ms, TA=4:35min), Axial SWI (0.6x0.6x1.6mm, FA=15 degrees, TR=28, TE=20, TA=3min), Axial T2 (0.5x0.5x3mm, FA=150degrees, TR=7880, TE=105ms, TA=1:44min), DSC perfusion (FA=90degrees, TR=1600ms, TE=30ms, TA=1:42min after 2.5ml gadobutrol preload at 1ml/s followed by 5ml at 5ml/s) , CSI spectroscopy Slaser (10x10x15mm, FA=90degrees, TR=1700ms, TE=40ms, TA=7:56min).
Area of acquisition	Whole brain for all sequences except for spectroscopy that covers the tumour

Diffusion MRI ☒ Used ☐ Not used

Parameters Axial 2D DWI (1x1x4mm, FA=180 degrees, TR=7670ms, TE1=59ms, TE2=99ms, b-value1=0, b-value2=1000s/mm^2, TA=3:29min)

Preprocessing

Preprocessing software	SyngoVia (Siemens, Erlangen, Germany)
Normalization	*If data were normalized/standardized, describe the approach(es): specify linear or non-linear and define image types used for transformation OR indicate that data were not normalized and explain rationale for lack of normalization.*
Normalization template	*Describe the template used for normalization/transformation, specifying subject space or group standardized space (e.g. original Talairach, MNI305, ICBM152) OR indicate that the data were not normalized.*
Noise and artifact removal	*Describe your procedure(s) for artifact and structured noise removal, specifying motion parameters, tissue signals and physiological signals (heart rate, respiration).*
Volume censoring	*Define your software and/or method and criteria for volume censoring, and state the extent of such censoring.*

Statistical modeling & inference

Model type and settings	NA
Effect(s) tested	*Define precise effect in terms of the task or stimulus conditions instead of psychological concepts and indicate whether ANOVA or factorial designs were used.*

Specify type of analysis: ☐ Whole brain ☐ ROI-based ☐ Both

Statistic type for inference (See Eklund et al. 2016)	*Specify voxel-wise or cluster-wise and report all relevant parameters for cluster-wise methods.*
Correction	*Describe the type of correction and how it is obtained for multiple comparisons (e.g. FWE, FDR, permutation or Monte Carlo).*

Models & analysis

n/a	Involved in the study
☒	☐ Functional and/or effective connectivity
☒	☐ Graph analysis
☒	☐ Multivariate modeling or predictive analysis